Nano-scale Heat Transfer in Nanostructures: Toward Understanding and Engineering Thermal Transport

A DISSERTATION

SUBMITTED TO THE FACULTY OF

UNIVERSITY OF MINNESOTA

BY

Jihong Ma

IN PARTIAL FULFILLMENT OF THE REQUIREMENTS

FOR THE DEGREE OF

DOCTOR OF PHILOSOPHY

Advisor: Traian Dumitricã

May 2017

Acknowledgements

I would firstly like to thank my PhD thesis advisor, Prof. Traian Dumitricã, for his tremendous help and guidance in my academic career. His insightful suggestions enabled me to perform important and interesting research at the frontier of nanoscale material science.

I would also like to thank my PhD committee members, Prof. Terrence Simon, Prof. Andre Mkhoyan, Prof. Michael McAlpine and Prof. Traian Dumitricã, for spending their time and effort to serve on my committee and provide useful comments.

I sincerely appreciate the support from my colleague, Dr. Ilia Nikiforov, who patiently answered many of my questions during the early stages of my study. I would also like to thank my other colleagues, Dr. Yuezhou Wang and Mr. Hao Xu for their support in my career development.

I would like to acknowledge all my collaborators for their excellent work and meaningful discussions, including Dr. Shiyun Xiong, Dr. Sebastian Volz, Dr. Peter Kroll, Dr. Efstathios Meletis, Ms. Atreyi Dasmahapatra, Dr. Changguo Wang, and Mr. Yuanpeng Liu.

I would like to thank Mr. Albert Swanson's family for their generous donation to support my thesis writing in my final year.

Finally, I would like to thank my parents for their spiritual support to complete my PhD. I would also like to thank my husband Gabriel Al-Ghalith for his tremendous help in my life and career, including dramatically speeding up my code, optimizing my computer system, compressing my files with high speed, and generating graphs and videos for some of my published work.

All the calculations presented in this thesis were performed on Minnesota Supercomputer Institute, Extreme Science and Engineering Discovery Environment, and High-End Computing Capability from NASA.

Abstract

Heat transfer is vital throughout research and industry. This thesis focuses on heat transfer in nanostructures and amorphous materials, in which the arrangement of atoms is crucial for the effectiveness of heat transport. Defects and mechanical deformations in a material which cause displacement or reconfiguration of atoms relative to that material's "normal" or "pristine" condition can dramatically influence its heat transport efficiency. Since the 1950's, there has been little progress in understanding the defects–thermal transport property relationship. Using novel numerical techniques and large-scale computations performed on modern supercomputers, I have studied heat transport in nanomaterials containing various defects and mechanical deformations. From the properties of atomic vibrations in my simulations, the effects these deformations have on heat transport can be deduced.

Three research projects are presented in this thesis. The study of heat transport in screw-dislocated nanowires with low thermal conductivities in their bulk form represents the knowledge base needed for engineering thermal transport in advanced thermoelectric and electronic materials. This research also suggests a new potential route to lower thermal conductivity, which could promote thermoelectricity. The study of high-temperature coating composite materials helps with the understanding of the role played by composition and the structural characterization, which is difficult to be approached by experiments. The method applied in studying the composition-structure-property relationship of amorphous Silicon-Boron-Nitride networks could also be used in the investigation of various other similar composite materials. Such studies can further provide guidance in designing ultra-high-temperature ceramics, including space shuttle thermal protection system materials and high-temperature-resistance coating. The understanding of the impact of bending and collapsing on thermal transport along carbon nanotubes is important as carbon nanotubes are excellent materials candidates

in a variety of applications, including thermal interface materials, thermal switches and composite materials. The atomistic study of carbon nanotubes can also provide crucial guidance in multi-scale study of the materials to enable large-scale thermal behavior prediction.

Publications[1]

Xiong, S.; **Ma, J.**; Volz, S.; Dumitrică, T., Thermally-Active Screw Dislocations in Si Nanowires and Nanotubes. *Small* **2014,** *10*, 1756-1760.

Ma, J.; Ni, Y.; Dumitrică, T., Thermal Conductivity and Phonon Scattering in Severely Bent Carbon Nanotubes and Bi-layer Graphene. *Materials Today: Proceedings* **2015**, *2*(6), 3819-3823. (*Presented in a keynote lecture)*

Ma, J.; Ni, Y.; Volz, S.; Dumitrică, T., Thermal Transport in Single-Walled Carbon Nanotubes under Pure Bending. *Phys. Rev. Applied* **2015**, *3*, 024014.

Wang, C.; Liu, Y.; **Al-Ghalith, J.**; Dumitrică, T.; Wadee, M. K.;Tan, H., Buckling behavior of carbon nanotubes under bending: From ripple to kink. *Carbon* **2016**, *102*, 224-235.

Al-Ghalith, J.; Ni, Y.; Dumitrică, T., Nanowires with Dislocations for Ultralow Lattice Thermal Conductivity. *Phys. Chem. Chem. Phys.* **2016**, *18*, 9888-9892

Al-Ghalith, J.; Dasmahapatra, A.; Kroll, P.; Meletis, E.; Dumitrică, T., Compositional and Structural Atomistic Study of the Amorphous Si-B-N Networks of Interest for High-Performance Coatings. *J. Phys. Chem. C.* **2016**, *120*, 24346-24353

---

[1] Al-Ghalith, J. is the same author as Ma, J.

Table of Contents

List of Tables

List of Figures

Abbreviations and Acronyms

Below is a list of commonly used abbreviations and acronyms in this thesis.

ZT	Figure of merit
σ	Electrical conductivity
S	Seebeck coefficient
κ	Thermal conductivity
T	Temperature
NW	Nanowire
NT	Nanotube
Si	Silicon
PbSe	Lead selenide
SiGe	Silicon Germanium
N	Nitrogen
B	Boron
Si_3N_4	Silcon nitride
h-BN	hexagonal Boron nitride
a-Si-B-N	amorphous Silicon-Boron-Nitride
C	Carbon
CNT	Carbon nanotube

SWCNT   Single-walled carbon nanotube

MD   Molecular dynamics

NEMD   Nonequilibrium molecular dynamics

b   Burgers vector

DFT   Density functional theory

RDF   Radial distribution function

s   Curvature

PDOS   Phonon density of states

Chapter 1

Introduction

1.1 Motivation and Objectives

Heat transfer, or heat, is thermal energy in transit due to a special temperature difference. Heat transfer has been studied as early as 1701, when Sir Isaac Newton formulated the law of cooling. In modern times, this area is affecting almost every sector of our life and industry. For instance, it is fundamental to thermoelectric devices, high-performance electronics, and micro-scale or nano-scale thermal management.

Broadly, the known heat transfer mechanisms are classified into three categories[1]: *conduction*, which is the transfer of energy from more energetic particles to less energetic particles of an object through interactions between particles; *convection*, which is the energy transfer due to bulk movement of fluids; and *radiation*, which transfers thermal energy through electromagnetic waves. Among these three mechanisms, heat conduction dominates in solids. For the materials of interest in this thesis, the heat carriers are lattice vibrations, or phonons.

The modern principles of heat conduction in solids were formulated[2] by Peierls, in 1929. The interest in the role of defects on thermal conductivity started in 1950, in conjunction with the research on thermoelectric materials[3,4]. In nano-scale, the arrangement of atoms helps determine how well heat is transported through the material. Defects and mechanical deformations in a material, which manifest in displacement or reconfiguration of atoms relative to their "normal" or "pristine" condition, can dramatically influence how efficiently heat is conducted through it. This is because phonons travel relatively large distances in solids (mean free paths of 10-100 nm), they are sensitive even to distant structural defects, on which they scatter. As such, the thermal conductivity is very subtle to microstructure. In fact, early measurements of thermal conductivity in solids aimed to study lattice defects[4]. Owing to recent technological progresses (for instance, the growth of the nanowires and the atomistic simulations), we view this conjuncture as an opportunity for engineering phonon scattering via nanostructure complexity.

1.1.1 Heat Transfer in Screw-dislocated Thermoelectric Nanowires

Thermoelectricity is the conversion of temperature differences to electric voltage. Thermoelectric materials are now attracting considerable attention due to the

recently demonstrated advances and strong global demand for cost-effective, pollution-free forms of energy conversion[5]. Applications include refrigerators, which, unlike traditional coolers, avoid emitting harmful refrigerants; regeneration of electricity from waste heat; and radioisotope thermoelectric generators, using the heat released by the decay of radioactive material into electricity, a strategy adopted by the "Curiosity" space robotic rover on Mars[6]. However, the conversion efficiency of current thermoelectric materials is low, making the price so high that most of them can only serve applications where cost is less critical. Advances in thermoelectric materials are necessary to eliminate these restrictions.

The efficiency of the conversion from thermal energy to electricity is measured by the dimensionless figure of merit *ZT*, which is defined as

$$ZT = \frac{\sigma S^2 T}{\kappa} \tag{1-1}$$

where σ, S, κ and T denote electrical conductivity, the Seebeck coefficient, thermal conductivity and temperature, respectively. Desired efficiency of solid state thermoelectric devices[7] is $ZT \cong 3$ to 4. From the definition of *ZT*, we can see that by lowering κ, *ZT* will get closer to the desired value. It has been reported that in the case of Silicon (Si), which is a good representative of the nanostructures in thermoelectricity, κ will be substantially reduced in nanowires (NWs) with respect to

that in bulk materials[8–13]. Meanwhile, the presence of native oxides, defects, surface ripples, surface roughness[14] and germanium (Ge) coatings[26] will further decrease κ, thus increasing ZT. Until today, the best thermoelectric materials have ZT between 1 and 2. Hence, additional mechanisms to lower κ are desirable.

Line defects, often referred to as dislocations, are most often associated with mechanical properties of materials. As discussed in the highly-cited review of Klemens[15], it has been long recognized by physicists the role of dislocations as important sources of phonon scatterings due to their spatially-extended character. According to Klemens, in bulk, dislocations lead to a significant decrease in κ in the direction *perpendicular* to the dislocation line. Recent experiments indicate that both NWs and nanotubes (NTs) can be grown via the propagation of an axial screw dislocation[16]. No one had ever explored the thermal transport *along* the dislocation line in screw-dislocated NWs and NTs.

Regarding the choice of materials, we note that bulk and nanomaterial forms of lead selenide (PbSe) alloys and silicon germanium (SiGe) alloys are intensively investigated for high performance thermoelectrics[17,18]. Thus, lower thermal conductivity can be expected by introducing screw dislocation in PbSe NWs and SiGe NWs. The gained understanding can be used to engineer dislocations that minimize (for thermoelectrics) or maximize (for high power electronics) or minimize thermal

conductivity of structures, depending on their applications.

1.1.2 Thermal and Mechanical Studies of Amorphous Silicon-Boron-Nitride Network

Ultra-high-temperature ceramics are a class of synthetic materials with superior thermal, mechanical, and oxidation resistance properties. They have various industrial applications including space shuttle thermal protection system materials[19,20] and high-temperature-resistant coatings[21,22]. One focus of protective coating research has been amorphous Silicon Nitride (Si_3N_4) containing B (a-Si−B−N), in particular a-$Si_3B_3N_7$[23], a ternary material synthesized via the sol−gel route[24]. Especially because of the experimental difficulties associated with the structural characterization of amorphous materials, computer simulations are playing an important role in understanding the structure properties relationship. Important experimental results have been already reproduced by atomistic calculations carried out on computer-generated networks. For example, molecular dynamics simulations found that the a-$Si_3B_3N_7$ networks exhibit a very high resistance against crystallization, up to 1,900 K[25,26]. In good agreement with experimentation[27], molecular dynamics simulations also predicted that the a-$Si_3B_3N_7$ bulk modulus ranges between 50−250 GPa, depending on its density[28]. Hence, a comprehensive study of a-Si-B-N network with molecular dynamics simulations is

feasible and reliable to guide industrial applications of these ultra-high-temperature ceramics.

1.1.3 Thermal and Mechanical Studies of Deformed Carbon Nanotubes

A carbon nanotube (CNT) can be described as a seamless cylindrical hollow tube formed by wrapping a single sheet of pure graphite (a hexagonal lattice of carbon, similar to a chain link fence), see Figure 1. Since Iijima[29] reported his experimental observation of CNTs using transmission electron microscopy, the study of CNTs has flourished. Due to their special sp^2 C-C bonds and their hollow quasi-one dimensional structure, CNTs present extraordinarily high κ in the axial direction[30–34] and excellent mechanical properties[35–40]. Their high κ along the tube direction motivated exploratory research for a wide variety of applications of CNTs, including reinforced composites[41], field emission devices[42], sensors and probes[42] and thermal interface materials[43–45].

When polymer composites filled with CNTs is under compression, a nonlinear elastic "kinking" response is often encountered, see Figure 2. The effect of the buckling kink of CNTs on their thermal conductivity has been investigated in both experiments[46,47] and simulations (atomistically and mesoscopically)[48–51]. However, no
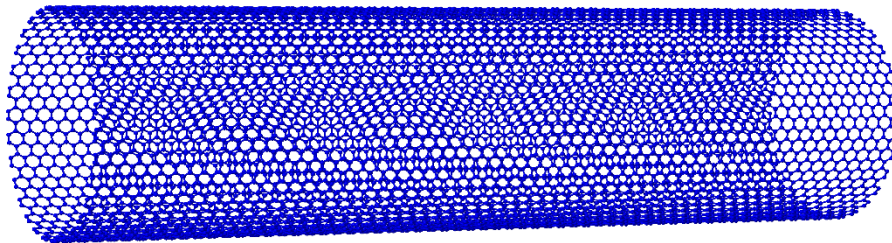
Figure 2. An armchair single-walled carbon nanotube.

(a)

(b)
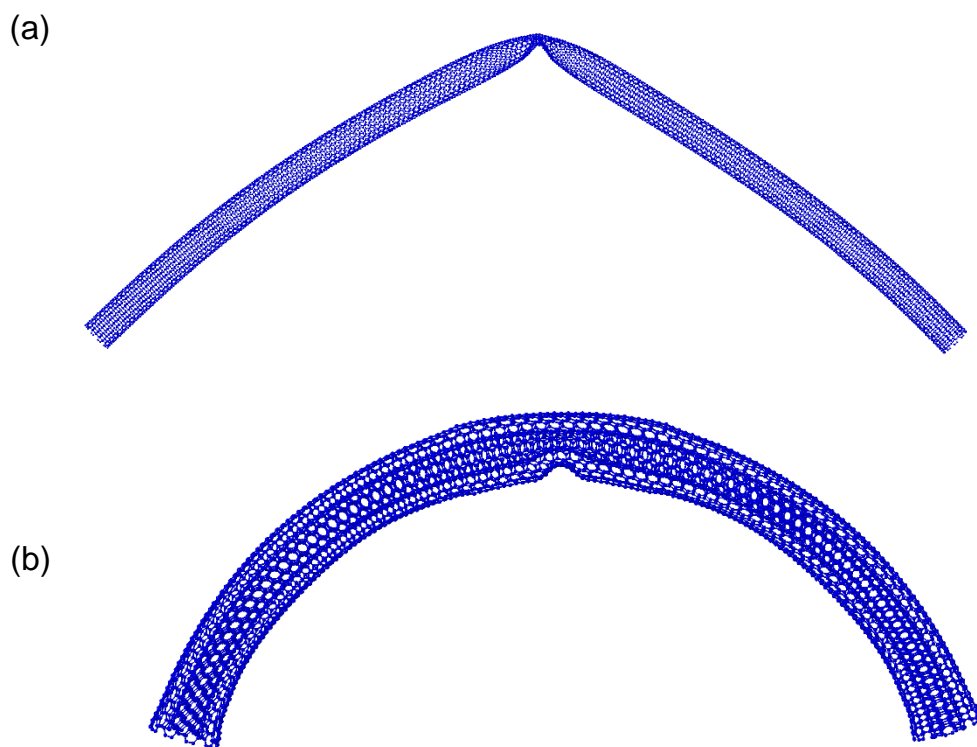
Figure 1. (a) A bent single-walled carbon nanotube with a kink formed. (b) a bent double-walled carbon nanotube with a kink formed.

clear conclusion on whether the thermal transport is affected by the bending or not had been reached.

Their tube-like structures are also susceptible to collapsing[52–61], which could impact their physical properties. However, the relation between collapsing and thermal transport remains to be discovered, as most κ studies of CNTs only focus on the ones with small diameters[30,31,48–50,62–65], despite the wide applications of CNTs with large diameters[66–68]. Experimental[52–57] and computational[59–61] studies have discovered that CNTs with large cross-sectional diameters (>~2.5nm) present an energetically favorable flat conformation due to surface van der Waals interactions, Figure 3, and the closest wall-wall distance is about 3.36 Å. The potential influence of the deformation on thermal transport along CNTs is important in understanding quasi-one dimensional
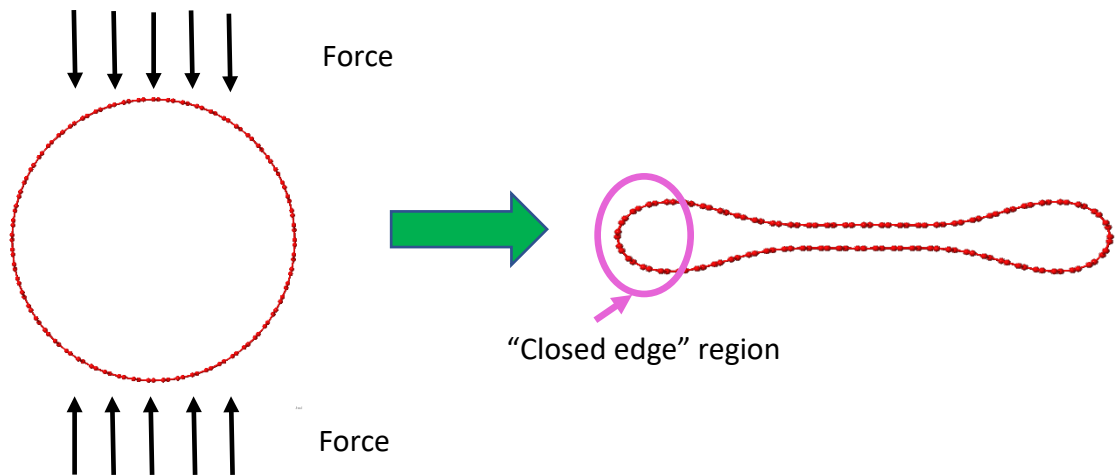
Figure 3. Formation of a flattened CNT from a cylindrical CNT, viewed along the tube.

phonon scattering mechanisms, which can further provide guidance in their applications.

1.2 Theoretical Background

1.2.1 Dislocation Theory

Dislocations are defined as boundaries between deformed and non-deformed regions in crystalline structures. In other words, a dislocation line represents the slip front of propagation of a line defect. The Burgers vector, which is generally used to define a dislocation in a crystal, depicts the direction and amount of slip. Its magnitude gives a characteristic discontinuity of displacement caused by dislocation. There are two basic types, edge and screw, Figure 4[69], which are just extreme forms of all possible dislocations.

Dislocations are most often associated with mechanical properties of materials. They allow plastic deformations to occur at lower applied stresses since they permit glide of one entire crystal plane over the one below, in a discrete way. Besides, the motion, multiplication and interaction of dislocations cause strain hardening, a common phenomenon in which continued deformation increases the strength of a crystal. The

strength and ductility, and thereby the mechanical behavior of a crystal, are controlled by dislocations.

(a)   (b)
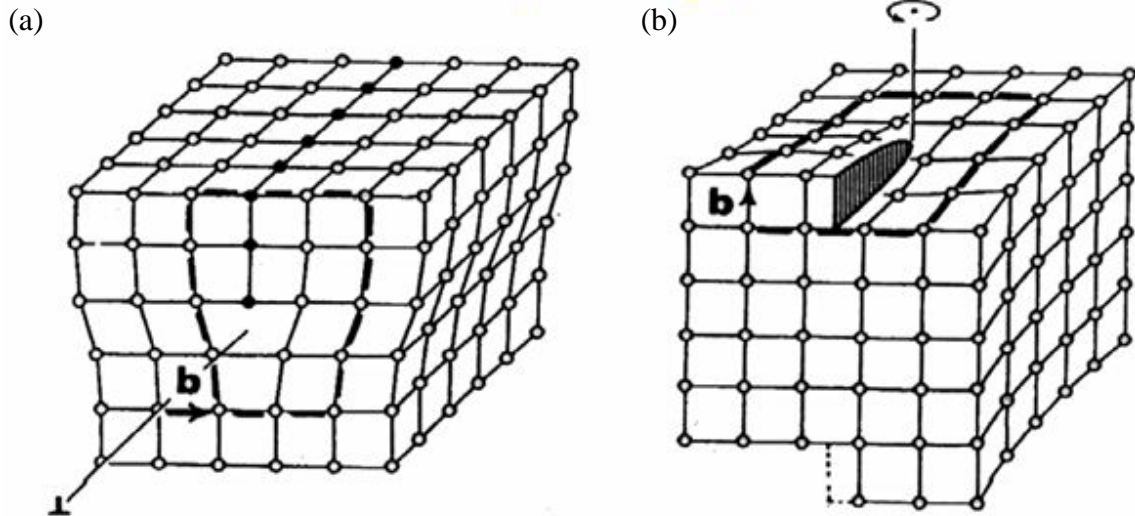
Figure 4. Schematic representation of (a) edge and (b) screw dislocations in a simple cubic crystalline material, where filled circles denote the lattice points of a crystal, b is a Burgers vector, hatched area and dashed line illustrate the slip plane and dislocation line, respectively.

Dislocations distort the crystal structure in a complex manner. While away from the dislocation line, the deformation field can be well described with linear elasticity, the highly deformed core region is inaccessible to continuum methods, and it is largely treated on an empirical basis. For example, consider a screw dislocation of Burgers vector's magnitude b. The elastic strain energy is calculated by integrating the strain energy density and by simply adding an empirical term E_c,

$$E_{screw} = (Gb^2/4\pi)\ln(R/r_c)+E_c \tag{1-2}$$

where G is the shear modulus of a material, R and r_c denote the outer dimension of the structure and the dislocation core size, respectively.

What is less commonly appreciated is that dislocations naturally arise during growth[70], Figure 5 (a)[71]. In fact, they are of importance for the growth of both bulk crystals and nanomaterials[72–74]. This is because the screw dislocation offers a non-vanishing growth step allowing the growth to advance in a spiral manner without the need for nucleation of a new layer.
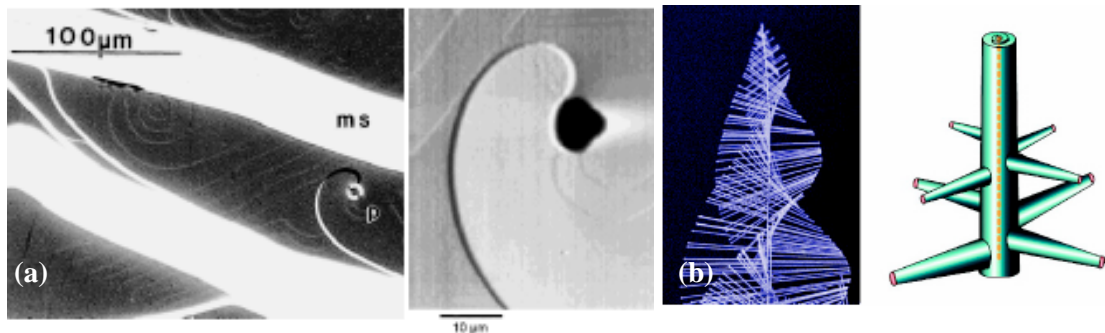
Figure 5. (a) Screw dislocations in bulk SiC. Experimental images showing a micropipe or open-core dislocations. The right side shows an enlarged image. (b) Screw dislocations in a PbS NW. Electronic microscopy of the "pine tree" NW (left) and schematic representation of screw-dislocation-driven trunk growth (right).

The dislocations occurring during growth are often in the form of pipes, Figure 5 (b)[75]. An early explanation for the pipe formation was given by Frank[76]. He showed that for a super screw dislocation (with large b), a state of equilibrium exists, in which

the core is an empty pipe. Frank's model predicts the equilibrium radius R for the pipe from the balance between the energy due to the screw dislocation given by Equation (1-2) and the created surface energy. For these reasons, the pipes are referred to as open-core dislocations. More recently, nano-pipes and other dislocation types, including closed-core super screw dislocations have been observed in GaN[77,78].

Recent experiments[16] presented convincing evidence that both NWs[74,79] and NTs[72,73] can be grown via a common mechanism of the propagation of an axial screw dislocation, Figure 5 (b). According to classical crystal growth theory, the supersaturation of a system can be manipulated to dictate the growth mechanism. At low supersaturation, dislocation-driven spiral growth prevails, at intermediate the layer-by-layer growth dominates, while at high supersaturation dendritic growth sets in. Screw dislocation line defects provide an endless source of crystal steps to enable nanostructure growth at low supersaturation conditions. As yet, screw dislocations have been identified in a variety of quasi-one-dimensional materials[73,74,80–84] including PbSe. What is important here, is that the understanding of dislocation-driven growth[16] just reached the point where realistic progress can be made towards growing nanomaterial with controllable morphologies (Burgers vectors, chirality, NTs or NWs), in large quantities, and at reasonable costs. Unfortunately, little is known about the way the dislocations influence the properties of these new states of matter.

1.2.2 The Classical Theory of Heat Transfer

In the early theory of Klemens[15], the various scattering mechanisms (acting simultaneously) are treated as perturbations to the harmonic approximation, i.e. the motion of the individual atoms in the crystal lattice can be represented as an ensemble of excitations, each of which has a well-defined energy and crystal momentum. When quantized, these excitations are referred to as phonons, i.e. lattice vibrations. Phonons carry energy as they propagate through crystals and thus contribute to κ. For the harmonic approximation, phonons are the quantum eigenstates of the atomic system, which can propagate without dissipation, thus resulting in an infinite κ. The finite κ in all solids is due to dissipation, which must occur by phonon scattering of either each other (anharmonic interactions), or from imperfections of the lattice (point defects, dislocations, interfaces, etc.)[85].

As we treat phonons as pseudo particles traveling through solids, we find, from the kinetic theory of gases, in a certain approximation the following expression for the thermal conductivity,

$$\kappa = \frac{1}{3} C_v v l \qquad (1\text{-}3)$$

where C_v denotes the heat capacity at constant volume, v is the average particle velocity, which is the speed of the sound at this level of the theory, and l is the phonon mean free path, i.e. either the characteristic length for scattering of phonons off each other or off a structural defect.

In Figure 6[86], we see that at low temperature regime, the size effect matters as the mean free path is long enough to allow that phonon scattering occurs at the surface. Thus, κ can be expressed, instead of Equation (1-3), as follows:

Figure 6. Thermal conductivity of a highly purified crystal of sodium fluoride. At low temperature, $\kappa \sim T^3$; at higher temperature, $\kappa \sim T^{-1}$.

$$\kappa \approx C_v v D \qquad (1\text{-}4)$$

where D is the size of the specimen. As the temperature gets lower, the only factor that changes κ is the heat capacity C_v, which, according to Debye's approximation, has the following relation with temperature:

$$C_v \propto T^3 \qquad (1\text{-}5)$$

Thus, κ is also proportional to T^3 until the size effect does not matter. While at higher regime, where κ decreases with the increase of the temperature, the mean free path $l \ll D$, when the size effect doesn't exist. At this state, the heat capacity C_v can be treated as a constant. Hence the magnitude of mean free path l dominates. At higher temperatures, the total number of excited phonons is proportional to T, so that the collision frequency of a given phonon is proportional to the number of phonons, which leads to the mean free path $l \propto T^{-1}$. Hence κ is proportional to T^{-1} as well.

The atomistic theory of κ incorporating defects was first studied in detail by Klemen[15,87], Carruthers[88], Ziman[89], and Callaway[90], by whom the various scattering mechanisms (anharmonicity, point defects, and dislocations, etc.) are treated as perturbations to the harmonic Hamiltonian. Scattering probabilities are then computed with the Fermi Golden rule, while transport properties were captured by the Boltzmann transport equation (BTE) for the probability distribution function f^λ of the phonons in the state λ:

$$-v_\lambda \frac{\partial f_0^\lambda}{\partial T} \nabla T = f_{scatt}^\lambda \qquad (1\text{-}6)$$

where f_0^λ is the equilibrium Bose-Einstein distribution. Here, the usual assumption of the local equilibrium is made on the left-hand side of the equation. The solution to this equation is so complicated that we would use the relaxation time approximation (RTA) as a standard approach. The approximation is stated as follows:

- if a probability distribution function for a given phonon mode is not an equilibrium distribution, then the scattering strength is proportional to the deviation from equilibrium with some characteristic time constant τ that incorporates all the information about the scattering processes;

- each relaxation mode is independent of all the others, and thus, all other modes are considered to be in equilibrium.

With these two approximations, Equation (1-6) can be simplified as

$$-v_\lambda \frac{\partial f_0^\lambda}{\partial T} \nabla T = \frac{f^\lambda - f_0^\lambda}{\tau_\lambda} \tag{1-7}$$

Nonetheless, investigations[85,91] have demonstrated that the RTA underestimates κ. Within the RTA, the value of κ can be expressed as a generalization of the Equation (1-3):

$$\kappa_{ij} = \sum_\lambda C_v v_i^\lambda v_j^\lambda \tau_\lambda \tag{1-8}$$

where i, j are the Cartesian indices, and λ is as denoted before, the phonon states.

After invoking Debye's approximation for phonon dispersion, κ writes as an integral over all possible phonon frequencies ω

$$\kappa = (1/2\pi^2 v) \int_0^{\omega_d} C_v(\omega)\tau(\omega)\omega^2 \, d\omega \tag{1-9}$$

where ω_d is the Debye frequency, and τ is the phonon lifetime. The contribution of each scattering effect is mixed in via the Matthiessen rule[92]

$$1/\tau = 1/\tau_s + 1/\tau_c + 1/\tau_d + \cdots \tag{1-10}$$

where the three terms (τ_s, τ_c, τ_d) aim to capture the effect of dislocations[15] as follows:

- τ_s, the contribution from the scattering on the linear-elastic strain field of the dislocation

$$1/\tau_s \propto N_d b^2 \gamma^2 \omega \tag{1-11}$$

where N_d is the dislocation density, b is the magnitude of the Burgers vector, and γ the Grüneisen parameter (capturing the effect of volume change on vibrational properties).

- τ_c, the contribution from the scattering on the non-linear elastic region of the dislocation

$$1/\tau_c = N_d \left(r_c^4 / v_p^2 \right) \gamma \omega^3 \tag{1-12}$$

where as before r_c is the radius of the core and v_p is the phonon phase velocity. This result is based on approximating the strain in the core as the one resulting from a line of vacancy defects[88].

- τ_d, the dislocation dynamics[93,94] term

$$1/\tau_d \propto \omega^{-1} \qquad\qquad (1\text{-}13)$$

which accounts for the dislocation motion.

Regarding bulk materials, the phenomenological theory of Klemens predicts κ reduction due to dislocations. However, as has been recognized before, this theory underestimates κ by at least an order of magnitude in comparison with the experimental data. For example, Sproull *et al.*[95] measured the impact of dislocations on the κ of LiF crystals. They found that the reduction in κ is much larger than Klemens' predictions[87]. Even when enhanced with more complex effects, significant deviations still exist between phenomenological modeling and experiment[88,96]. In addition, it is essential to note that the impact of dislocations on κ also depends on temperature. When the density of line or point defects is low enough (for GaN[97], it's lower than 10^6 cm^{-2}), the defects scatter appreciably only at temperatures below 100 K[98–101] and insignificantly otherwise[97]. On the contrary, at temperatures greater than 100 K, κ decreases with a logarithmic dependence for materials with dislocation densities in the range of 10^7– 10^{10} cm^{-2} such as GaN[97]. This might be attributed to the fact that the mean free path is directly related to the temperature. When at higher temperature, the mean free path is so short that it cannot be easily affected by the sparse defects. But when the density is high enough, the phonons can be scattered by the dislocations. Otherwise, at lower temperature, the mean free path is long enough to allow the phonons to be scattered by

the less dense defects.

In this respect, our MD simulations should bring significant improvements as they allow for an accurate account for the dislocation core region. Note that estimates for the core radius r_c range from b to $5b$, where b is the magnitude of the Burger's vector and the displacement field of the core, needed in Klemens theory, is unavailable for continuum methods. Here, we are concerned with super screw dislocations (with large b). Additionally, we note that the classical term (1-12) doesn't capture explicitly the size of the Burgers vector and doesn't distinguish between open and closed-core dislocations. Thus, the classical theory does not allow exploring the phonon engineering of screw dislocations.

Regarding nanostructures, it is important to recognize that there is an essential difference between the thermal conductivity reduction captured by Klemens in terms (1-11) and (1-12), and the problem of thermal transport in screw dislocated nanostructures. Klemens refers to scattering of the phonon states (eigenstates of the harmonic ideal problem) on the linear and non-linear elastic strains localized around the dislocation line, Figure 7. By contrast, in our proposed studies of Si, PbSe and SiGe NWs and NTs, we encounter the unexplored case of thermal transport *along* the screw dislocation line. Due to the objective periodicity of the strain field of the dislocation, which extends over the whole nanostructure, we are interested in the thermal transport

through phonon carriers that are eigenstates of the strained dislocation core (that are satisfying the Bloch theorem generalized for helical symmetry[102]). Hence the classical theory doesn't apply.
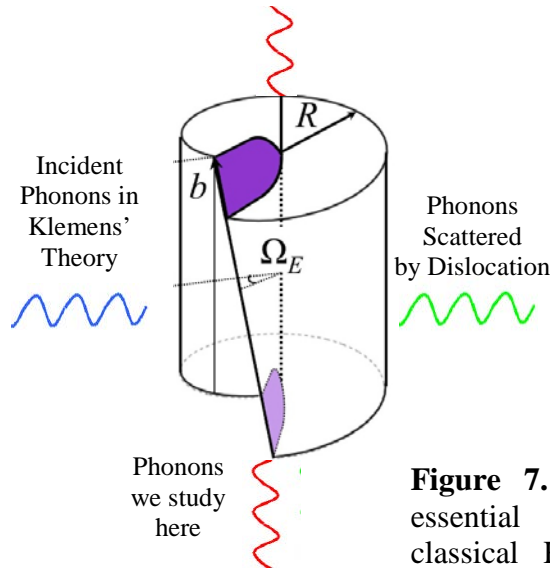
Figure 7. Schematics showing the essential differences between the classical Klemens' theory and our proposed line of research.

The only point common to Klemens's theory is the κ reduction via the dislocation dynamics. However, term (1-13) is likely unsuitable as the dislocation dynamics in NWs is often specific (different than in bulk, see Ref.[103]). In NW the dislocations are in the close vicinity of surfaces, and interaction of the core with the surfaces gains in importance. For more insight, it is useful to view it in a continuum elasticity perspective: A stable axial screw dislocation residing in a cylindrical rod (with a diameter order of magnitude larger than a NW) couples to a twisting

deformation known as the "Eshely twist" of magnitude Ω_E, Figure 7. This twist is visible in the experimental Figure 5 (b). Apparently, none of these effects (attraction by surfaces and twisting) are accounted for in equation (1-13). Thus, new mechanisms need to be uncovered.

1.3 Methodology

1.3.1 Boundary Conditions

In molecular dynamics (MD), each atom is treated as a point mass whose velocity and position are computed by time integration of the classical Newton's equations. The computational task is to solve the set of coupled differential equations given by

$$m_i \frac{d^2 \boldsymbol{x_i}}{dt^2} = -\frac{\partial \varphi}{\partial \boldsymbol{x_i}} \tag{1-14}$$

where m_i and $\boldsymbol{x_i}$ are the mass and position vector of the i-th particle, and $\varphi(\boldsymbol{x_1}, \boldsymbol{x_2}, ..., \boldsymbol{x_n})$ denotes the potential energy ranging from a simple pairwise atomic interaction for PbSe[104], to the Stillinger-Weber three-body potential for SiGe[105], and even to the more complicated *ab initio* fully quantum mechanical methods. However,

the number of atoms in a real system is usually so large that it is impossible to substitute all the positions of atoms into the potential function. Thereupon, by taking advantage of the inherent translational symmetry of the crystal structure with the periodic boundary condition (PBC), we can significantly reduce the number of atoms that need to be calculated.

$$x_{i,\zeta} = \zeta T + x_i \tag{1-15}$$

where T is the translational periodicity and $i = 1,2, \dots n_T$, where n_T denotes the number of atoms in the periodic cell. If we choose modest but sufficient number of atoms and properly set the PBC's, we can obtain the solutions with acceptable accuracy. Nevertheless, in some cases, the translational periodicity of the structure is extremely large and with rotational symmetry, as some cases in this thesis, PBC might not be a good choice. Here, we utilize the objective molecular dynamics[106] (OMD) which incorporates not only the translational symmetry of the structure, but also the helical and/or rotational symmetry, i.e. objective boundary condition (OBC), as in Figure 8. In my completed thesis work, only the rotational combined with the translational symmetry in one dimension is involved:

$$x_{i,\zeta} = \zeta T + R^\zeta x_i \tag{1-16}$$

where R denotes the rotational matrix

$$R = \begin{bmatrix} cos\theta & -sin\theta & 0 \\ sin\theta & cos\theta & 0 \\ 0 & 0 & 1 \end{bmatrix} \tag{1-16}$$

and T is along the z (axial) axis. Thus, the velocity $v_{i,\zeta}$ can be expressed as

$$v_{i,\zeta} = R^\zeta v_i \tag{1-17}$$

In this way, the realizable number of atoms within an objective unit cell enables the calculation with both accuracy and efficiency.
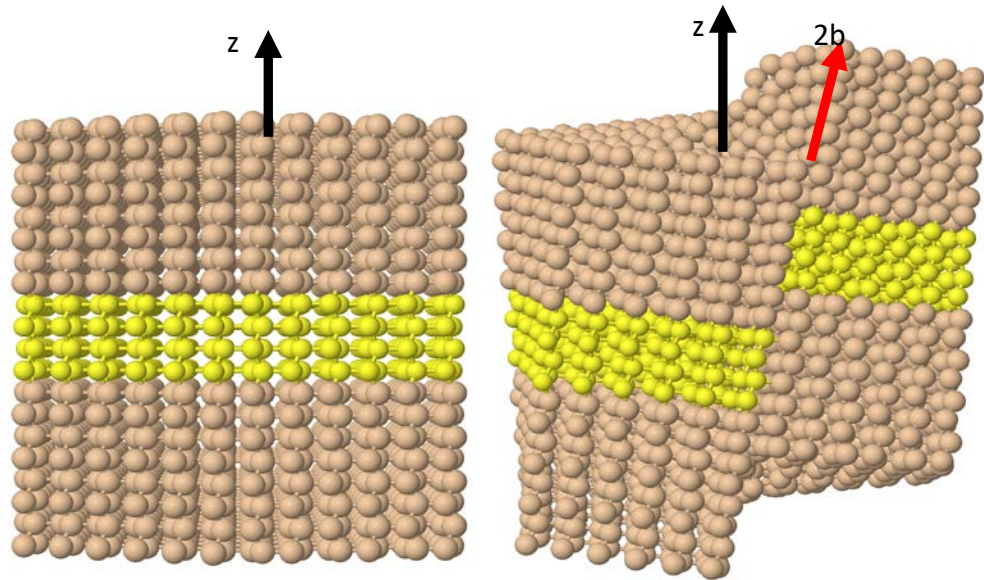
Figure 8. (a) A pristine and (b) a screw-dislocated Silicon nanowire with 2b Burgers Vector. By applying the periodic boundary condition along the z direction and the objective boundary condition (translating along the z direction and rotating about the z-axis) on the simulated unit cells (the light green part) in (a) and (b), we can obtain infinitely long pristine and screw-dislocated Silicon nanowires, respectively.

1.3.2 The Green-Kubo Method

Unlike fluids, the transport of heat in solids is derived from correlations in the motion of atoms around their equilibrium locations. Green-Kubo uses the fluctuation-dissipation theorem to derive an exact mathematical expression for κ, which is given by a time integral over the equilibrium flux autocorrelation function

$$\kappa_{\alpha\beta} = \frac{V}{k_B T^2} \int_0^\infty \langle j_\alpha(0) j_\beta(t) \rangle dt \qquad (1\text{-}18)$$

where $\kappa_{\alpha\beta}$ is a component of the lattice thermal conductivity tensor (α and β = x, y and z), V is the volume of the system, k_B the Boltzmann constant, T the temperature, t is the autocorrelation time. The angular brackets indicate ensemble average over microstates j.

MD uses a discretized version of (1-18) and a method for calculating the instantaneous heat flux j. The heat current is the time rate of change of the "energy moments",

$$j(t)V = \frac{d}{dt} \sum_i r_i \epsilon_i \qquad (1\text{-}19)$$

where ϵ_i is the total energy of particle i, comprising kinetic and potential components,

$$\epsilon_i = \frac{1}{2} m |v_i|^2 + \frac{1}{2} \sum_j \varphi\left(r_{ij}\right) \tag{1-20}$$

Substitute Equation (1-20) to Equation (1-19), we can get

$$\boldsymbol{j}(t) = \frac{1}{V} \sum_i \left[\boldsymbol{v}_i \epsilon_i + \frac{1}{2} \sum_{j,j\neq i} \boldsymbol{r}_{ij} \cdot \left(\boldsymbol{F}_{ij} \cdot \boldsymbol{v}_i\right) \right] \tag{1-21}$$

In solid, only the second term on the right-hand side of Equation (1-21) dominates in contributing to thermal energy transport. Thus, for pairwise potentials, the heat current typically writes[107]

$$\boldsymbol{j}(t) = \frac{1}{2V} \sum_{i,j,i\neq j} \boldsymbol{r}_{ij} \cdot \left(\boldsymbol{F}_{ij} \cdot \boldsymbol{v}_i\right) \tag{1-22}$$

For three-body potentials, like the Stillinger-Weber potential[105], the three-body contribution must be taken into account. Therefore, the flux expression is more complicated[108],

$$\boldsymbol{j}(t) = \frac{1}{V} \left[\frac{1}{2} \sum_{i,j,i\neq j} \boldsymbol{r}_{ij} \cdot \left(\boldsymbol{F}_{ij} \cdot \boldsymbol{v}_i\right) + \frac{1}{6} \sum_{i,j,k,i\neq j\neq k} \left(\boldsymbol{r}_{ij} + \boldsymbol{r}_{ik}\right) \cdot \left(\boldsymbol{F}_{ijk} \cdot \boldsymbol{v}_i\right) \right] \tag{1-23}$$

In MD, the integration time is MΔt (not ∞), and equation (1-18) takes the form[107],

$$\kappa_{\alpha\beta} = \frac{\Delta t}{3Vk_bT^2} \sum_{m=0}^{M} \frac{1}{N-m} \sum_{n=1}^{N-m} j_\alpha(m+n)j_\beta(n) \qquad (1\text{-}24)$$

where M is the number of steps over which the ensemble average is calculated, N is the total number of time steps after equilibration has been reached, and Δt is the MD time step. The MD can be carried out under periodic boundary conditions (PBC) or objective boundary conditions[106,109] (OBC).

1.3.3 The Direct Method

The direct method, is also known as non-equilibrium molecular dynamics (NEMD), in which a temperature gradient is imposed on the atomistic sample by thermostatting different "bath" regions at different temperatures. A variety of thermostatting options are available in Trocadero and LAMMPS, including Langevin[110] and Nosé-Hoover[111,112]. The simulated portion of the material usually has one long
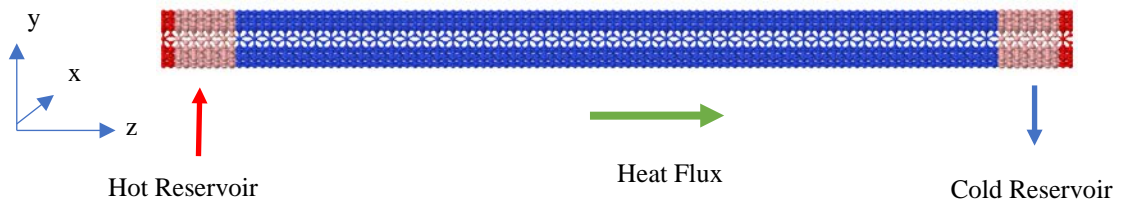
Figure 9. A CNT set up for calculating thermal conductivity along the axial direction (z direction) with NEMD. The red rings in the two ends are fixed ends. The pink rings next to the red ones are hot and cold reservoirs, respectively. The heat flux flows from the hot reservoir to the cold reservoir along the tube.

dimension and a smaller cross-section. The temperature gradient is imposed along the long dimension. For bulk simulations, PBC will be used on the sides (x and y directions). Regarding the treatment of the long side (along z), two options exist in the literature[113], either to keep the end atoms fixed, or impose PBC. Here, we only use the fixed boundary condition, as shown in Figure 9.

In NEMD the goal is to reach steady state. The variation in temperature across the length of the sample becomes meaningful at steady state. A linear temperature profile is expected between thermostats. Then, the thermal conductivity can be determined as

$$\kappa = -j(\frac{\partial T}{\partial z})^{-1} \tag{1-25}$$

This method is plagued by size effects, due to phonon scattering at the thermostatting boundaries and restrictions on the maximum phonon mean free path. In NWs, the size effects are real in the x and y directions and they will be captured in simulations. More specifically, thermal conductivity of a sample is prone to size effects when the dimensions fall below 5-10 times the phonon mean free path. Nevertheless, procedures are in place in order to determine the bulk thermal conductivity of a material from molecular dynamics simulation. The usual way is to extrapolate the finite size thermal conductivity up to the bulk value as follows:

$$\kappa(L) = \kappa_\infty \left(\frac{L_z}{L_z + 4l_\infty} \right) \tag{1-26}$$

where L_z is the length of the simulation cell, l_∞ and κ_∞ are the phonon mean free path

and thermal conductivity in an infinite system (i.e., bulk crystal or nanowire).

Chapter 2

Thermal Transport in Screw-dislocated Nanowires and Nanotubes

Nanostructures grown by screw dislocations have been successfully synthesized in a range of materials, including thermoelectric materials, but the impact of these extended crystallographic defects on thermal properties of these nanostructures is not known. We investigate thermal transport in Si, PbSe and SiGe nanowires storing screw dislocations via non-equilibrium molecular dynamics and equilibrium molecular dynamics simulations. The inherent one-dimensionality and the combined presence of a reconstructed surface and dislocation yield ultralow thermal conductivity values. Our simulations suggest that the large dislocation strain field in nanowires may play a key

role in suppressing the thermal conductivity of thermoelectric nanomaterials to increase their thermoelectric figure of merit. This work was published in Ref[114] and Ref[115].

2.1 Introduction

Thermoelectric (TE) devices[116] have found applications in various areas, from aerospace and petroleum to consumer electronics and automobiles. Unfortunately, current TE devices suffer from low energy conversion efficiency, which is limited by the performance of the current TE materials. The conversion efficiency is characterized by the dimensionless figure of merit $ZT = \sigma S^2 T / \kappa$ at the absolute temperature T. The ZT components of electrical conductivity (σ), Seebeck coefficient (S), and thermal conductivity (κ) are interdependent. Low κ is an important consideration in ensuring high ZTs. Enhanced ZT values as high as close to 2 have been reported in materials with spontaneous nanoscale phase segregation or pressed from ball-milled nanoscale grains or synthetic nanostructures[5,117,118] Exploring novel κ-lowering strategies is of interest as ZT values larger than 3 are needed for increasing the energy conversion efficiency of these thermoelectric devices to the level found in mechanical systems.

Recently, Jin *et al.*[16,74,119,120] discovered that screw dislocations play an important role in the growth of anisotropic nanomaterials, such as PbSe nanowires (NWs). The entire volume of these nanostructures is in close proximity to the dislocation core with the largest strain field. In general, dislocations and strain[121] play a less important role in bulk low-κ thermoelectric materials, which are often characterized by strong lattice anharmonicity. However, in $Bi_{0.5}Sb_{1.5}Te_3$, it has been reported that lattice κ lowering by dislocation-scattering, reinforced by liquid phase compaction, gives dramatic *ZT* improvement (~1.86 at 320 K)[122]. Therefore, it remains an open question whether screw dislocations can result in a major suppression of κ in nanostructures with both high and low κ in their pristine forms.

2.2 Thermal Conductivity in Screw-dislocated Silicon Nanowires and Nanotubes

In this work, I combine modern theories based on atomistic simulations in order to understand how the thermal properties of <110> silicon (Si) NWs and NTs accommodating axial screw dislocations with closed and open cores might differ from the more studied pristine forms. After computing the screw-dislocated NW and NT structures with objective molecular dynamics[106] (MD), we used two main methods, the

direct method[123] and the atomistic Green function method[124–126] (simulations were carried out by Dr. Shiyun Xiong), to reveal an important reduction in κ. This finding presents significant interest for nanoscale thermoelectricity.

I simulated a set of pristine and screw-dislocated Si <110> NWs and NTs with cubic diamond structure and hexagonal cross sections. The number of 111 layers L in the cross-section was taken to be 12, 16, 20 and 30, so that the radii of the created NWs ranged from 18.8 Å to 47.1 Å. Next, from the pristine L =12 NW we created a set of (L,h) NTs, by systematically removing central atomic layers. We label by h the number of 111 inner layers that have been removed. Finally, in all these structures we introduce screw-dislocations with the axis located at the center. We considered minimal Burgers vector of magnitude b =3.8 Å and multiples of it, 2b and 3b. In 1b NWs, the created core structure is the Hornstra core, where all atoms remain fourfold coordinated.

Screw-dislocations twist NWs and NTs. This is the Eshelby twist[127] γ_E, which is well known at the macroscale. The presence of γ_E creates challenges for atomistic simulations as it prevents the applicability of the standard periodic boundary conditions. Here, in order to find optimal morphologies (corresponding to minimum energy) we used objective MD[106] coupled with a Tersoff classical potential[128]. The method allows for performing simulations of screw-dislocated NWs and NTs under

arbitrary twist in an economic fashion, always using the same N, the number of atoms located in the primitive cell of the pristine structure.

Examples of optimized structures are shown in Figure 10. Each structure corresponds to the minimum of the computed total energy vs. twist angle θ. As illustrated in Table 2-1, in accordance with Eshelby theory[127] we find that γ_E increases with the magnitude of the Burgers vector. Moreover, the obtained γ_E and formation energies of the dislocations compare very well with those computed with a higher-level quantum mechanical description of bonding[129], thus indicating the reliability of our modeling. Note also that dislocation does not affect the surface structural relaxation[72,129,130].

Having identified the atomic positions inside the objective cell and γ_E, we constructed long nanostructures. We computed κ with the direct method, based on nonequilibrium classical MD at a 300 K mean temperature. During our MD runs, the NWs and NTs maintain their crystalline structure as well as the central location of the dislocation. Thereby, we recognize that scattering contributions by defects and dislocation motion[15] are not included in our results. Nevertheless, our MD simulations are subject to size effects. Therefore, for the (12,0) NWs and (12,4) NTs, we simulated structures with lengths of 10, 20, 30, and 40 nm. The computed finite-size κ has been extrapolated[123] to predict κ for the infinitely-long case, Figure 11 (a) and (b).

Table 2-1. Number of Si atoms in the objective cell, twist, energetics, and thermal conductivity of (12,0) NWs and (12,4) NTs. The magnitude of the Burgers vector (1b, 2b, and 3b, where b =3.8 Å) is indicated in the subscript notation.

(L, h)	N	γ_E (deg/Å)	E_d (eV/Å)	κ (W/mK)[b]
(12, 0)	228	0	0	50
(12, 0)$_b$	228	0.19 (0.19[a])	0.79 (0.94[a])	36
(12, 0)$_{2b}$	228	0.39 (0.36[a])	2.05 (2.15[a])	20
(12, 0)$_{3b}$	228	0.56 (0.53[a])	3.74 (3.40[a])	12
(12, 4)	204	0	0	28
(12, 4)$_b$	204	0.18	0.09	23
(12, 4)$_{2b}$	204	0.35	0.35	17
(12, 4)$_{3b}$	204	0.52	0.77	12

a) These values, shown here for comparison, were obtained with a density-functional theory-based method[129];
b) These values correspond to infinitely-long structures.

Consistent with previous studies, we find that the presence of surfaces in pristine Si NWs leads to significant κ reduction. For example, in a (12,0) NW we measured κ = 50 W/mK, which represents 25% of the bulk Si value[9] of 196 W/mK This value is consistent with previous studies employing MD and Tersoff potentials[131] and is larger than in experiments[12] because realistic effects, such as surface effects[9,14], are not included in our MD simulations. Nevertheless, our pristine structures only serve here as useful references, to help us distinguish the potential impact of screw-dislocations.
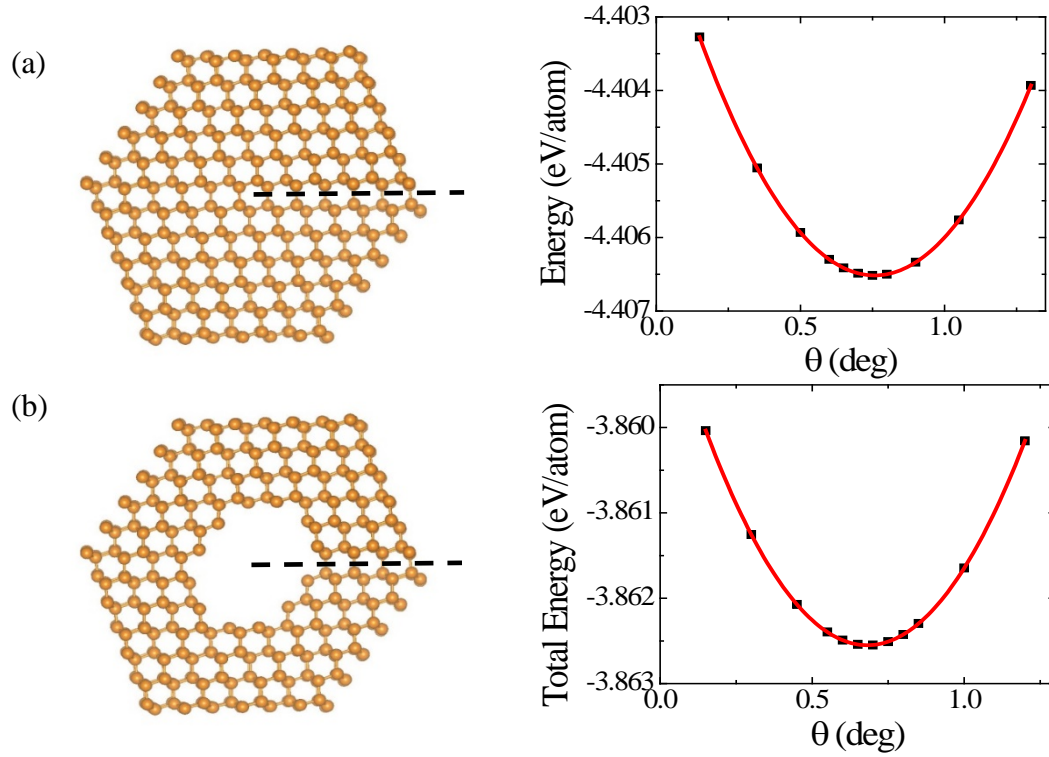
Figure 10. Optimal configuration (left) and total energy vs. twist angle (right) for (a) $(12,0)_b$ NW and (b) $(12,4)_b$ NT. The dashed line indicates the cut made to create the dislocation.

Remarkably, a screw dislocation leads to a sizable κ decrease. The values entered in the last column of Table 2-1, show a consistent decrease in κ with the magnitude of the Burgers vector. Likewise, an open core dislocation in NTs is reducing κ to a similar extent. For example, in both $(12,0)_{3b}$ NWs and $(12,4)_{3b}$ NTs, $\kappa = 12$ W/mK, which represents only 6% of the bulk value.

For more insight, Figure 11 (c) shows the computed κ for a series of NWs 20 nm in length. In Eshelby's theory, the amount of twist depends inversely on the cross-sectional area, so it decreases with the NW diameter. For example, a $(30,0)_b$ NW stores twist of only 0.03 deg/Å. Fortunately, Figure 11 (c) demonstrates that the Eshelby twist doesn't play a key role for heat transport. For this reason, the other panels of Figure 11 compare only pristine and untwisted dislocated structures. Additionally, the surface morphologies of pristine and untwisted and dislocated NWs are practically identical, Figure 12, and thus no differences in the phonon-surface scattering should be expected.

In Figure 11 (d) we compare the dependence of κ on the Burgers vector for NTs with different inner diameters. In pristine NTs, we find that the effect of the gradual increase of the inner surface is beneficial for thermoelectricity, as it leads to a κ decrease. When accounting for the size effects in the same manner as in Figure 11 (b), we obtained a 56% κ reduction between pristine (12,4) NTs and (12,0) NWs (see Table 2-1). This is an interesting result by itself considering the recent progress in the synthesis of pristine Si NTs[132]. Examining now the data for screw-dislocated cases, we find that as the NT's wall gets thinner, the impact of screw dislocations on κ diminishes: while in (12,2) NT the strain field leads to a significant κ reduction, in (12,8) NT, κ is hardly affected by the size of the Burgers vector. Overall, this study shows that the κ reduction is strongly linked to the complex screw dislocation core.

One way to match our notable MD results is to go beyond the harmonic approximation and accept that phonons can be scattered by other phonons. Indeed, the harmonic approximation is permissible as long as atoms remain very close to their equilibrium positions, forming bond lengths of 2.36 Å. Instead, in screw-dislocated NWs, large strains are involved. For example, we identified bond lengths measuring 2.5 Å in the Hornstra core of the $(12,0)_{1b}$ Si NW. Thus, strain-induced anharmonicity
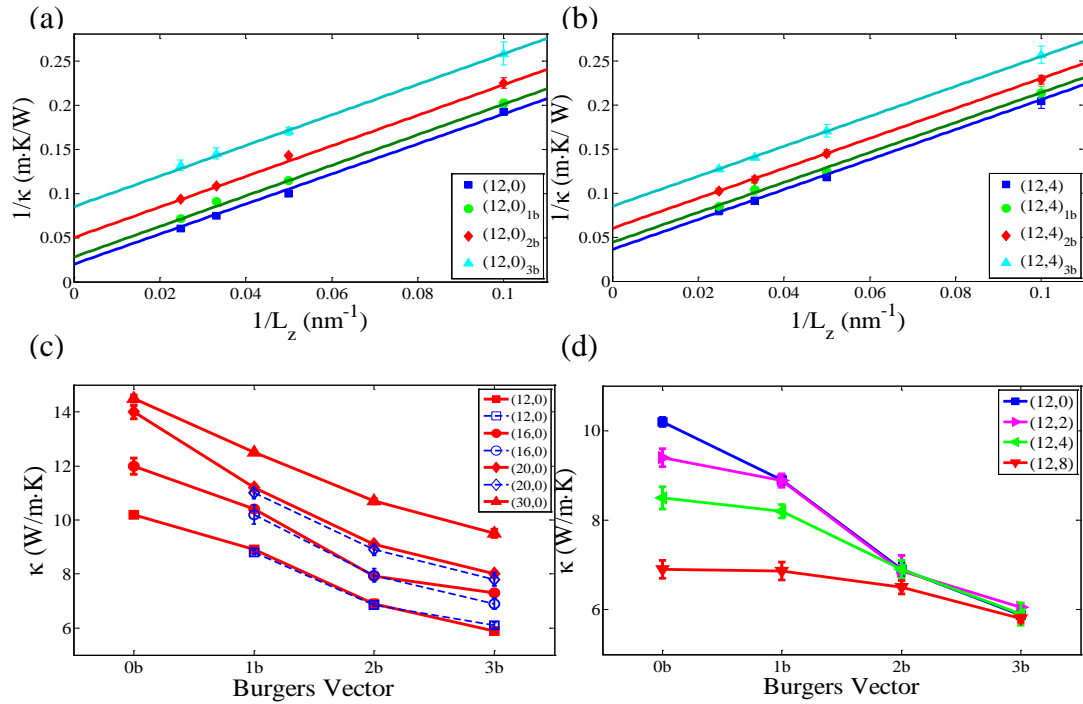
Figure 11. Dependence of $1/\kappa$ on $1/L_z$ for pristine and SD (a) (12,0) NWs and (b) (12,4) NTs. The intercept of the linear fit with the vertical axis gives κ for infinitely-long structures. Relative comparison of κ for (c) NWs and (d) NTs with $L_z = 20$ nm. The filled (open) symbols correspond to untwisted (twisted) structures. Here b = 3.8Å.
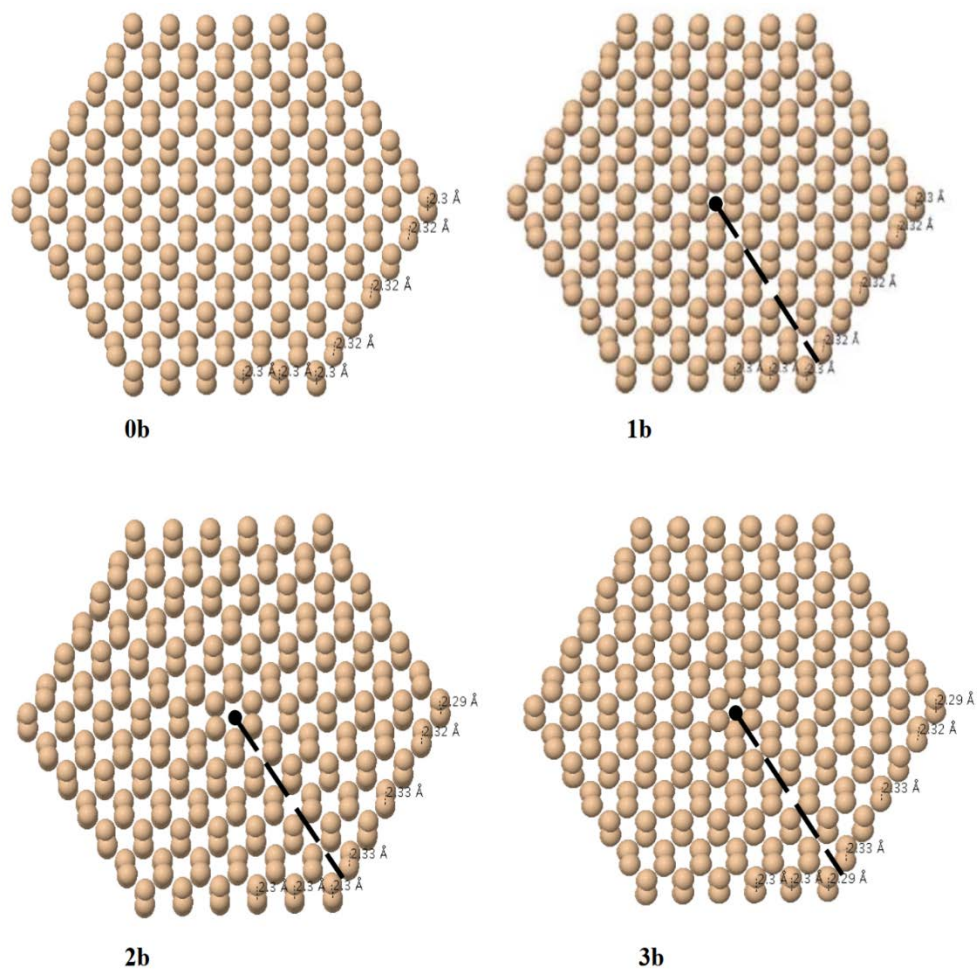
Figure 12. Cross section of untwisted (12,0) Si NWs with the size of the Burgers vectors marked under each structure. Selected surface bond lengths are shown. The dashed line indicates the cut made to create the dislocation.

of the interatomic potential, which leads in turn to phonon-phonon scatterings[133,134], should be expected. Because MD includes the full interaction potential, these anharmonic effects are already present in the MD data of Figure 11.

An attractive feature is that the effect uncovered here can act in combination with the known κ limiting mechanisms. To illustrate this point, we have performed exploratory MD calculations on (12,0) Si NWs coated with four layers of Ge. After accounting for the size effects, we obtained that the addition of a Ge shell leads to $\kappa =$ 40 W/mK for NW with pristine core, and to the even smaller values of 28.6, 11.8, and 7.2 W/mK for $(12,0)_b$, $(12,0)_{2b}$, and $(12,0)_{3b}$ NWs, respectively.

2.3 Thermal Conductivity in Screw-dislocated Lead Selenide and Silicon Germanium Nanowires

In this work, I investigate the phonon scattering on dislocations in lead selenide (PbSe) and silicon germanium (SiGe) NWs containing screw dislocations with various sizes of the Burgers vectors. Both materials present low κ in their bulk forms. For example, at 300 K, $\kappa = 2.2$ W/mK in PbSe[135] and $\kappa = 10$ W/mK in $Si_{0.5}Ge_{0.5}$[136]. By equilibrium molecular dynamics simulations, we uncover the significant thermal conductivity reduction in both systems and further demonstrate the robustness of the

proposed effect by comparing it with two other effects – surface roughness and vacancy defects – for which κ lowering is consistently computed with the same methods.

We have considered PbSe $< 100 >$ NWs with a square 2.45 X 2.45 nm^2 cross-section and a rock-salt crystalline structure, and SiGe $< 110 >$ NWs with a 4.33 X 3.75 nm^2 rectangular cross-section in which one type of atom is bonded in a tetrahedral geometry with four atoms of another type. The latter system is in the spirit of the early work of Abeles[137], where the idea of computing the thermal conductivity of SiGe alloys starting from an ordered virtual crystal was first introduced. The SiGe NW with a crystalline ordered structure represents a model system for investigating, separately, the potential effect of dislocations on κ.

We introduce screw dislocations with the axis at the center, see Figure 13, with minimal Burgers vectors (b = 6.12 Å in PbSe and 3.92 Å in SiGe) and larger (super screw dislocations with even multiples, n, of b). For this, I used the morphologies of the pristine NW structures. Starting from the NW center, the atoms in the vicinity of the cut-plane were gradually displaced along the NW axis until atomic displacements equal to the to the magnitude of the desired Burgers vector were reached and maintained up to surface atoms. The chosen location of the dislocation axis does not cross any atomic site, see Figure 13 (a). Note that the axial crystallographic orientation has an important role in the structural and thermal stability of NWs[138]. Here, the selection of the axial

orientation of the NWs was based on the experimental input for PbSe[74,82], and on energetic considerations related to the minimum size of the Burgers vector for SiGe. The lateral surface of NWs also has a remarkable effects on properties[139]. While in the previous section, I explored screw dislocations in NWs with hexagonal cross-sections[114], here, I consider NWs with rectangular cross-sections.

We carried out a series of equilibrium MD simulations with LAMMPS[140] to investigate the stability and thermal attributes of the dislocated NWs. For PbSe
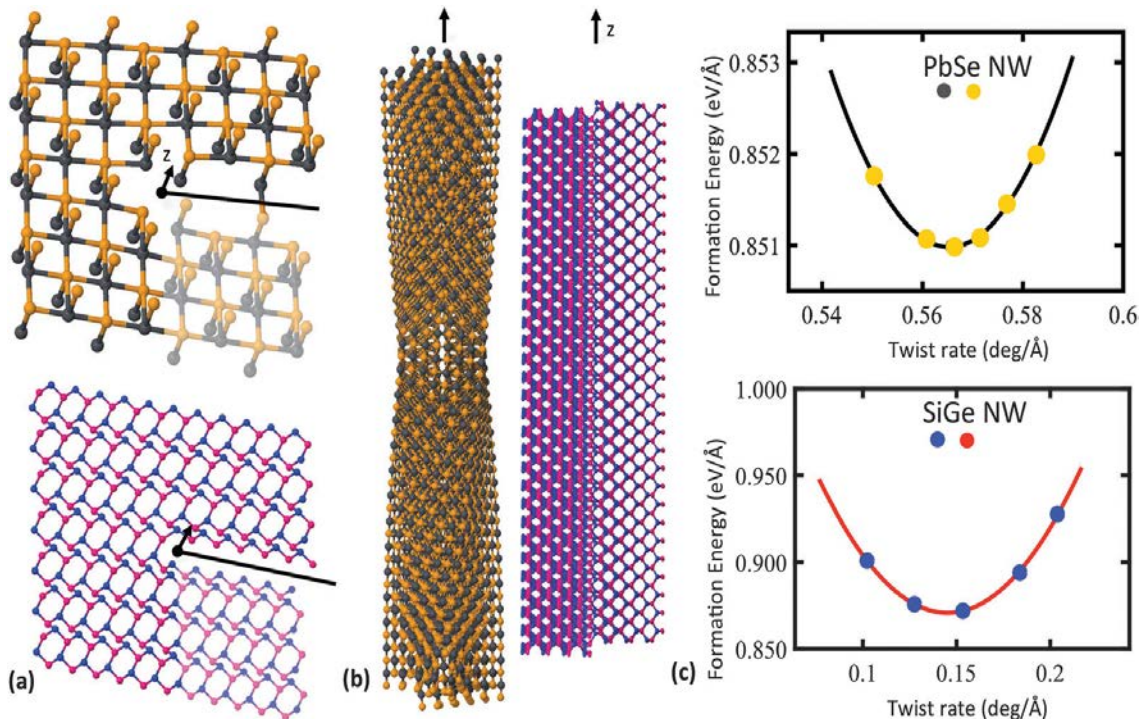
Figure 13. (a) Atomistic representation of stress-free configurations of the screw-dislocated unit cells of PbSe (top) and SiGe (bottom) NWs. The black line indicates the intersection of the cut-plane with the cross-section. (b) Side views of the dislocated and twisted PbSe (left), and dislocated and untwisted SiGe (right) NWs. (c) Formation energy (energy measured with respect to pristine NW) vs. twist rate.

structures, we adopted the interatomic potentials developed by Schapotschnikow et al.[104], which is a combination of Lennard-Jones (LJ) and Coulomb potentials,

$$U_{ij}(r_{ij}) = U_{coulomb}(r_{ij}) + U_{LJ}(r_{ij}) = \frac{q_i q_j}{4\pi\varepsilon_0 r_{ij}} + 4\varepsilon_{ij}\left[\left(\frac{\sigma_{ij}}{r_{ij}}\right)^{12} - \left(\frac{\sigma_{ij}}{r_{ij}}\right)^6\right] \quad (2\text{-}1)$$

where r_{ij} is the distance between i and j, ε_{ij} and σ_{ij} are the LJ parameters, q_i and q_j are partial charges on atom i and j, and ε_0 is the dielectric constant of a vacuum. Parameters of the LJ potential for the same type of atoms are defined as in Ref[104]; and for different types of atoms, the Lorentz-Berthelot mixing rules have been applied. In order to improve the simulation efficiency, instead of using 10 nm as the cut-off radius for electrostatic interactions as indicated in their paper, we applied Ewald summation to describe the long range electrostatic interactions. The lattice constant at 0 K and the bulk modulus in the rock salt[141] structure are 6.06 Å and 52.9 GPa, respectively, with our adapted method, which are comparable to the values obtained in their paper[141], 6.06 Å and 54.3 GPa, and other experimental measurements[,142], as well as the first principle calculations[143,144]. Thus, the cut-off radius approach can be safely replaced with Ewald summation.

The potential for PbSe systems has never been employed in thermal transport studies. To verify the potential, we are using MD simulations to calculate κ, I, firstly, calculated a series of cubic bulk PbSe structures with different sizes, side lengths

varying from 2.4 nm to 7.3 nm with periodic boundary conditions (PBC) applied in three directions. Initially, the structures were fully relaxed with a conjugate gradient energy minimization algorithm. The structures were evolved for 10 ps in the isothermal-isobaric ensemble to raise the temperature to 300 K in a vacuum. Then they were thermally equilibrated at 300 K for another 10 ps each in both canonical and microcanonical ensembles. The MD time step was set to 1 fs. Another 100 ps in microcanonical ensembles were carried out with the velocity Verlet integral after equilibrium, to calculate the heat flux. Then the Green-Kubo formula is applied to calculate κ. The results are shown in Figure 14. We can see that the κ is converged at around 3.2 W/mK when the side length reaches 3.7 nm, which is comparable to the results of the first principle calculations in Ref.[135]. Hence, this hybrid potential is sufficiently robust for predicting κ of the bulk PbSe phase.

We then took a similar procedure to calculate a series of pristine PbSe NWs with 2.45 X 2.45 nm^2 cross-sectional area (xy plane) and different lengths in the z direction. PBC was applied only in the z direction. The lengths of the calculated pristine structures vary from 3.06 nm to 30.13 nm in the z direction. κ has converged when the length is approximately 5 nm. These results are presented in Figure 15.
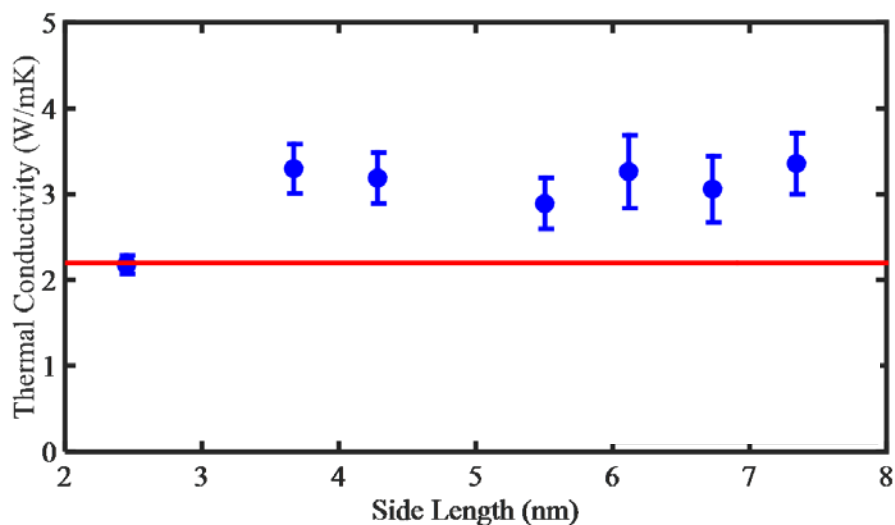
Figure 14. Thermal conductivity of bulk PbSe structures with different side lengths. The blue circles are calculated with MD simulation. The red line is the result from first-principle calculations.
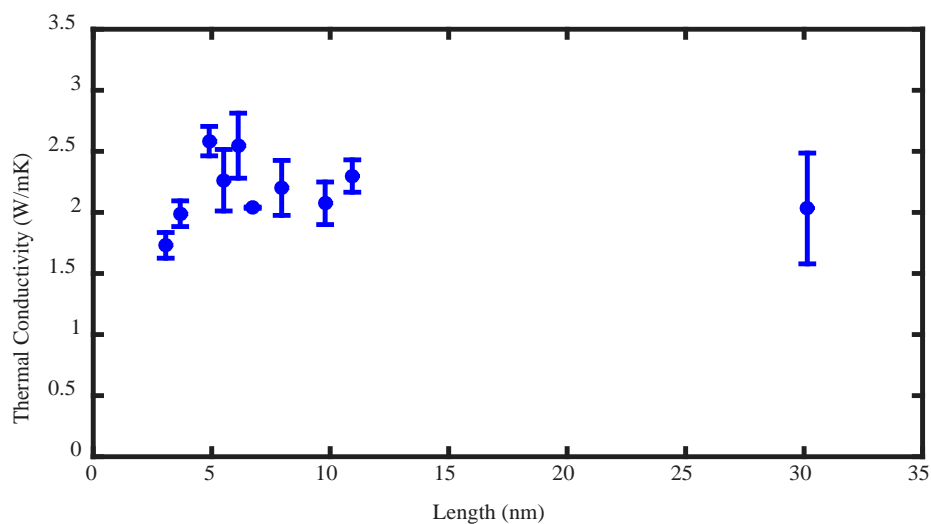
Figure 15. Thermal conductivity of pristine PbSe NWs with different lengths. The blue circles are the simulated results for pristine NWs.

For SiGe, I used the three-body Stillinger–Weber potential[105,145], which have been previously used to study thermal properties of SiGe systems[121,146,147]. κ was

obtained by averaging the calculated thermal conductivities over the number of ensembles. From Figure 16 we can see that the averaged κ of a pristine SiGe NW has converged to 5.1 W/mK after 25 ensembles. The error bar can be estimated as ± 0.1 W/mK.

Screw-dislocated NWs possess Eshelby's twist rates[129,130,148] of $nb/\pi R^2$, where πR^2 is the cross-sectional area of the NW and nb is the size of the Burgers vector, in agreement with classical theory[127]. Periodic and objective boundary conditions[106] were applied in the z direction, thus mimicking the simulation of infinitely long, straight or uniformly twisted NWs.
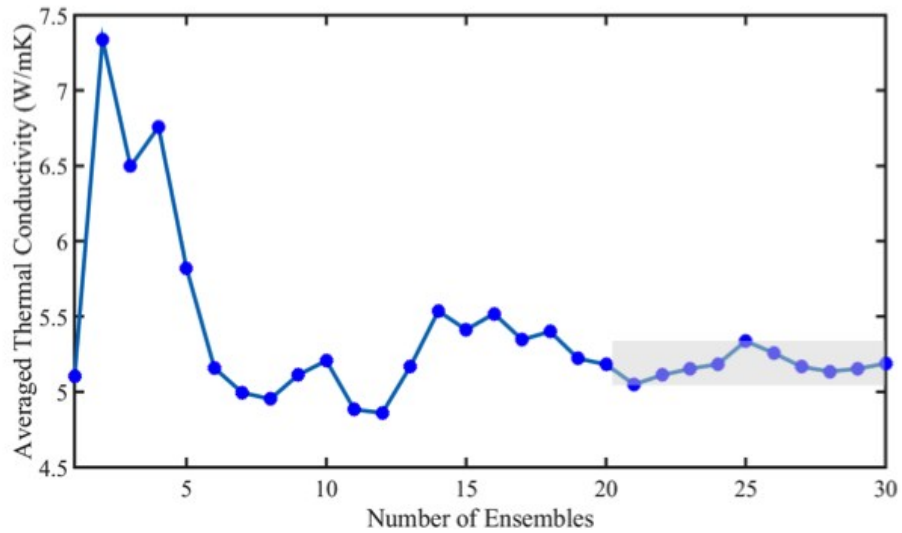
Figure 16. Convergence of thermal conductivity of pristine SiGe NWs with the number of ensembles. The shaded area represents the error bar.

In preparation for the κ calculation for the screw-dislocated NWs, the initial structures were relaxed with a conjugate gradient energy minimization algorithm. The calculation results presented in Figure 13 (c) indicate that for a PbSe NW storing a dislocation with minimal Burgers vector magnitude 1b, the optimal twist rate is 0.57 deg/Å. This twist lowers the formation energy of the dislocation by 31 %. Similarly, in a SiGe NW, the optimal twist rate of 0.15 deg/Å lowers the formation energy by 27 %. In the center of the relaxed NWs we did not observe the formation of homoelemental bonds. Nevertheless, the hetero-elemental bonds were severely strained. For example, in 4b PbSe NWs, bond lengths in the core region measured 3.2 Å, which represents a 5.6 % stretching with respect to the pristine case. Similarly, in 1b SiGe NWs, bonds are stretched by 6.7 %. On the one hand, in PbSe, our MD simulations obtained that without twist, the dislocation quickly migrates to the surface, leaving behind the pristine NW structure. Nevertheless, the Eshelby twist retains the dislocation at the central location, allowing us to compute the correlations in the vibration of the atoms around their strained positions. To comply with the Eshelby's twist, the sizes of the periodic cells used in our simulations were 21.4 nm (4b), 30 nm (2b), and 60 nm (1b). On the other hand, in SiGe NWs we find that accounting for the Eshelby's twist is not essential. Due to the strong Si–Ge bonds, the screw dislocation is retained at the center of the NW throughout the simulation. The simulation cells used for computing κ were 3.92 nm in length.

κ for NWs was also obtained using the Green–Kubo formula. As an example of the convergence of our MD simulations, Figure 17 (a) shows the computed κ as a function of the correlation time used to evaluate κ.
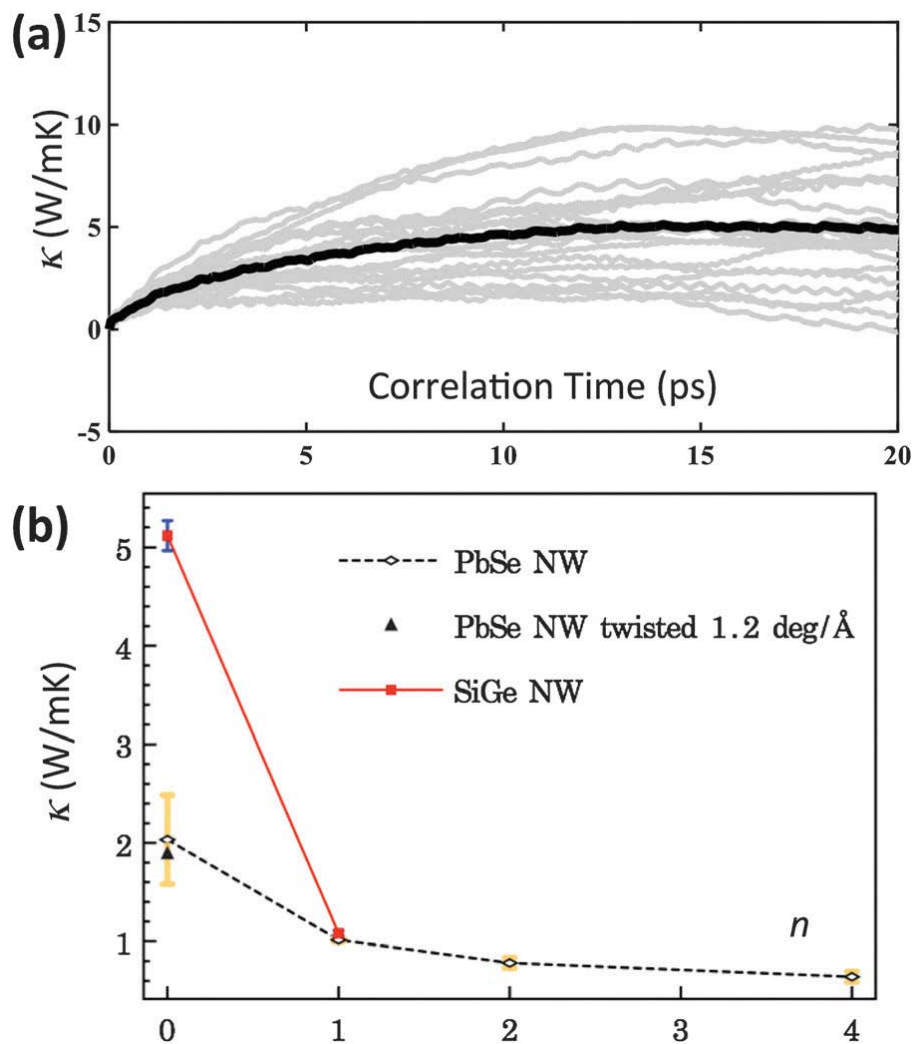
Figure 17. (a) Averaged integration (dark line) of heat flux over 30 ensembles (gray lines). Data represent the calculation of a pristine SiGe NW. (b) κ vs. n for nb PbSe and SiGe NWs. The black triangle represents κ of a pristine PbSe NW under 1.2 deg/Å twist.

We now examine the impact of screw dislocations on thermal transport. The results presented in Figure 17 (b) demonstrate that the presence of a dislocation is associated with ultra-low κ values. Specifically, the screw dislocation lowers κ of the pristine PbSe and SiGe NWs by ~80% (4b) and ~70% (1b), respectively. All dislocated NWs present κ values below ~1 W/mK. By comparison, our previous calculations[114]
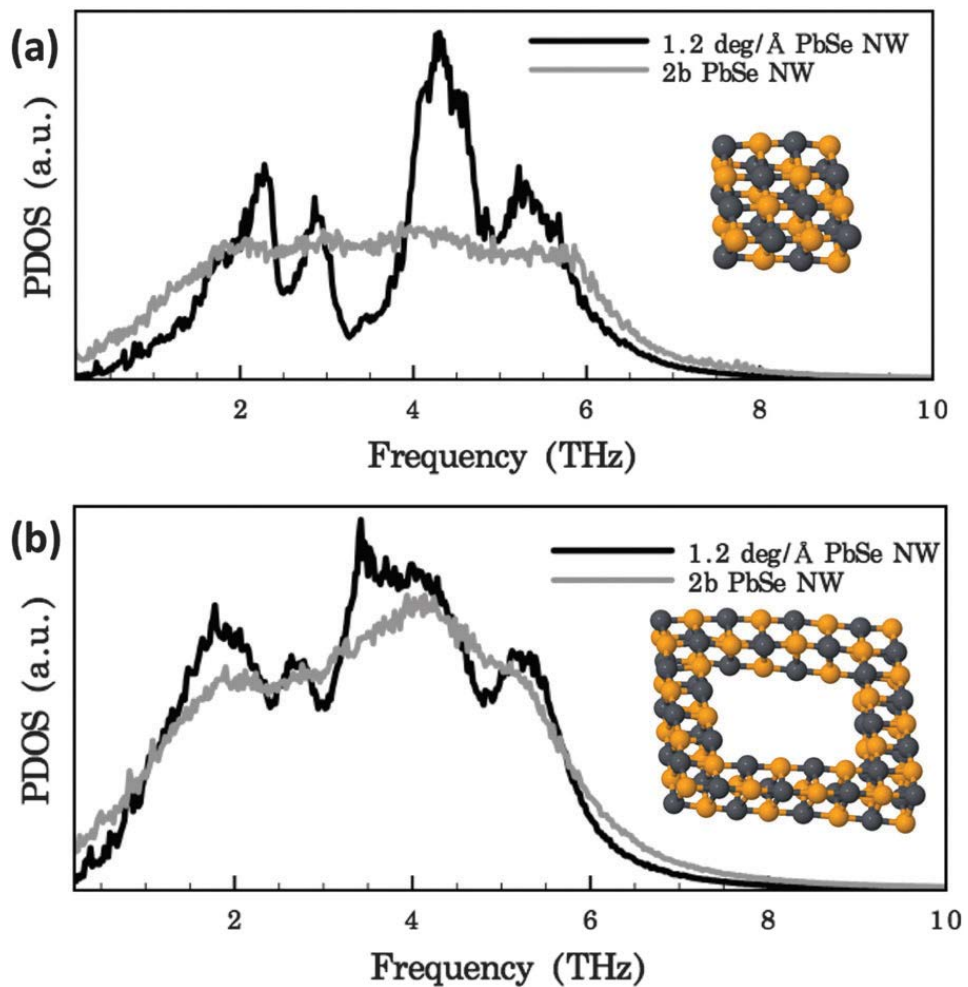
Figure 18. Comparison of the phonon density of states (PDOS) of the (a) core and (b) surface region of pristine and 2b PbSe NWs. Both NWs are twisted by 1.2 deg/Å. Insets show the core and surface regions of the twisted NW.

obtained κ values of 36 W/mK in 1b Si NWs with similar diameters. The effect is attributed to the efficient phonon scattering onto the dislocation core. Specifically, the strain at the core introduces anharmonicities, which enhance the phonon–phonon scattering processes. Based on the previous analysis[149], it can be expected that the core-induced anharmonicities are shortening the lifetimes of phonons, causing reductions in the phonon mean free paths. In Figure 18 (a) we compare the phonon density of states (PDOS) for the core regions of pristine and screw-dislocated PbSe NWs. We observe significant differences in the phonon spectrum. This result indicates that the dislocation core plays an important role in lowering κ as its presence affects phonon–phonon scattering. Note that both NWs are twisted by 1.2 deg/Å, so the observed differences cannot be attributed to torsional deformation.

In explaining the origin of the results of Figure 17 (b), we can rule out potential changes in phonon-surface scattering. First, in Figure 18 (b) there is little difference between the surface PDOS of the pristine and 2b PbSe NWs, both twisted by 1.2 deg/Å. Second, we recall that all the NWs considered so far have smooth surfaces, which were allowed to reconstruct during the structural relaxation stage and the MD runs. The boundary scattering of the heat-carrying phonons should be largely specular, as the κ values of the pristine stress-free NWs are not dramatically reduced with respect to the corresponding bulk values. For example, in the pristine PbSe NW there is a 36% reduction from the computed 3.2 W/mK value of the bulk phase. The specular

scattering of the phonons onto these surfaces leads, in turn, to an efficient scattering of phonons onto the core of the dislocation. Note that our test simulations demonstrated that the torsional deformation of the NW is not changing the dominant specular surface scattering mechanism into a diffuse one: in Figure 17 (b), it can be seen that κ of the PbSe NW twisted by 1.2 deg/Å is within the error bar of the corresponding stress-free structure.

Diffuse surface scattering on rough surfaces or interfaces is a recognized mechanism for κ reduction in NWs[14,150–152]. To get a glimpse into this scattering regime, in a series of MD simulations, we have explored how a progressive increase in surface scattering impacts κ of pristine and 1b SiGe NWs. In this respect, the NW morphologies were modulated with surface ripples, such as in the NW morphology shown in Figure 19 (a). The volume fraction of the removed atoms n_s provides a way to characterize the roughness of the modulation. On the one hand, our calculations obtained a sizable decrease in κ with n_s for the pristine NW, achieving saturation around $n_s = 10\%$. This κ decrease likely originates in the trapping of phonons within the ripples. This trapping effect lowers the average phonon group velocity. On the other hand, κ of 1b SiGe NWs is practically insensitive to n_s. This result suggests a scenario in which the scattering onto the dislocation core and the rippled surface act simultaneously to reduce κ. The surface roughness appears as a competing mechanism

as this process reduces the phonon scattering rate onto the dislocation core. Nevertheless, the NWs considered here are ultrathin. We expect that the surface scattering is a less effective κ-lowering mechanism when the NW diameter gets larger[146].

In my simulations, I have also considered vacancy point defects, which are also known to have an important impact on κ. When defects are randomly distributed and the concentration is low, κ is inversely proportional to the concentration of defects, n_v. Previous MD studies on carbon nanotubes[31] and crystalline silicon[153] have indeed led to an inverse power-law relation, $\kappa \propto n_V^{-\alpha}$, with the power constant α equal to 0.79 and 0.74–1.04, respectively. Our calculation results shown in Figure 19 (b) reveal a similar decrease with $\alpha \sim 1$ for both pristine PbSe and SiGe NWs and achieve saturation when $n_v \sim 2\%$. At saturation, the reduction in κ due to vacancies is less than the one achieved by dislocations alone. Furthermore, our calculations also considered the case when dislocations and vacancies act simultaneously. It can be see that κ of the 1b SiGe NW presents a small increase with n_v until the same saturation value is achieved. This behavior suggests that scattering on vacancy is also a competing mechanism as it reduces the phonon scattering rate onto the dislocation core.
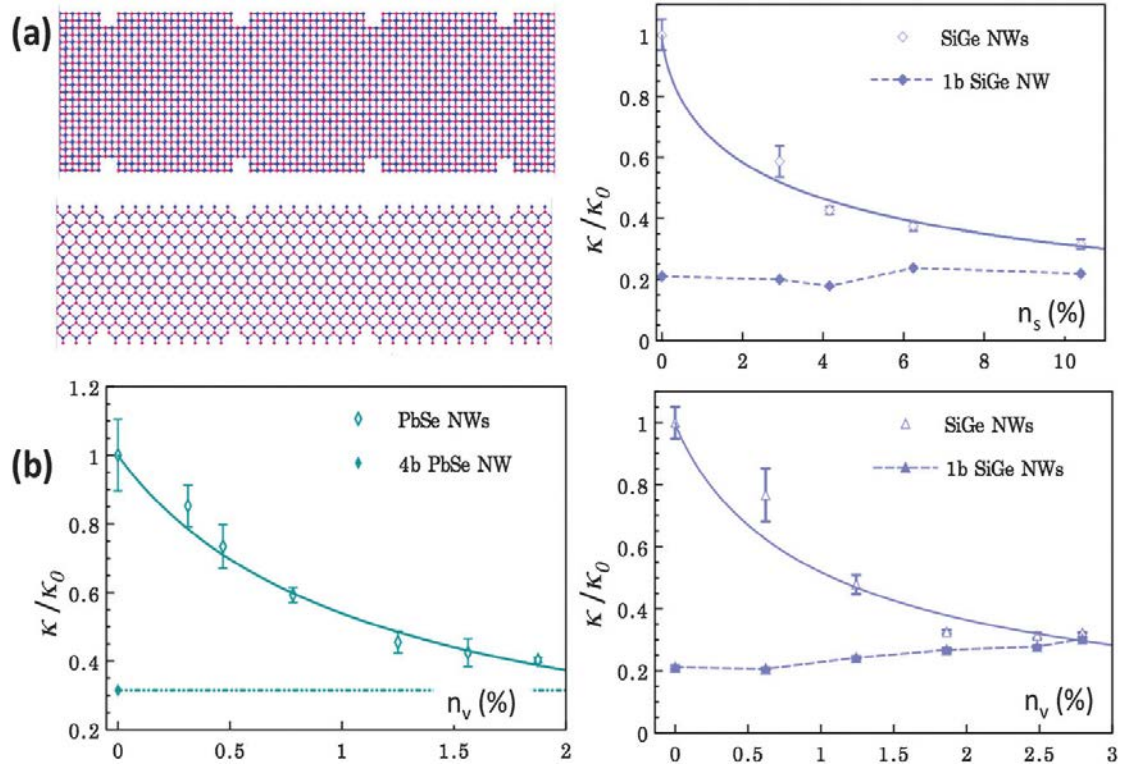
Figure 19. (a) SiGe NW with modulated surfaces. Side views of the $< 100 >$ (top) and $< 110 >$ (bottom) facets. The volume fraction of the removed surface atoms n_s is 2.9%. Thermal conductivity vs. n_s for pristine and 1b SiGe NWs. The fitted curve is $1 / (1 + 0.44 n_s^{0.69})$ (b) Thermal conductivity vs. the concentration of vacancy defects n_v for PbSe (left) with fitted curve $1 / (1 + n_v^{0.98})$ and SiGe (right) with fitted curve $1 / (1 + 0.93 \, n_v^{0.92})$ NWs. κ_0 is the thermal conductivity of the corresponding pristine NW. For SiGe NWs the cumulative effect (dislocation-surface modulation and dislocation-vacancy) was computed.

2.4 Conclusion

In conclusion, I have investigated $< 110 >$ Si, $< 100 >$ PbSe and $< 110 >$ SiGe NWs as model quasi-one-dimensional nanostructures with low thermal conductivities and different types of bonds. MD simulations revealed that screw dislocations are stable inside straight Si NW, SiGe NW structures and Eshelby's twisted PbSe NWs. The phonon scattering onto the dislocation core stabilized at the NW center leads to important reductions in κ of the ideal lattice. The presented comparison with scattering onto rough surfaces and vacancies indicates that the new screw dislocation effect is comparable with and can have priority over other competing κ-lowering mechanisms. The presented MD results provide hope for experimentally detectable difference of this effect over the bulk and surfaces of nanostructures. At the same time, they may have important implications for thermoelectric materials, as phonon scattering on dislocations could provide a new avenue for defect engineering of κ.

Chapter 3

Atomistic Study of Amorphous Silicon-Boron-Nitride Networks

In this work, through computational modeling, I explored the effects of boron−nitrogen (BN) composition on the thermal and mechanical properties of amorphous silicon−boron−nitride (a-Si−B−N), a synthetic ceramic material with superior thermal protection, mechanical attributes, and oxidation resistance at high temperatures. Network-derived Si−B−N models optimized with *ab initio* molecular dynamics serve as input structures for classical molecular dynamics simulations. Atomistic Green−Kubo simulations on relaxed supercells and structural relaxations on strained cells are used to screen the thermal and mechanical properties of a collection of network structures with low enthalpies of formation. We find that when the material is composed of well-mixed parts rather homogeneously spread within the material, the thermal conductivity and elastic constants are isotropic and exhibit a weak dependence on composition and network structure. In contrast, when separation into BN-rich layers occurs, the material exhibits anisotropic behavior, with an increase in thermal

conductivity along the layer direction and a decrease in elastic constant in the cross-layer direction. The insights provided into the composition−structure−property relationships can be useful for the rational design of amorphous Si−B−N materials targeting high-performance coating applications. This work has been published in Ref[154].

3.1 Introduction

In recent years, atomistic simulations are assuming a guiding role in the effort of optimizing the properties of advanced coating materials[155−159]. In a-Si−B−N, understanding the role played by composition is of great importance for the future design of this new material. So far, a-Si−B−N structures have been explored to understand the impact of the BN : Si_3N_4 ratio onto mechanical properties[27,28,160,161]. Using classical MD simulations, Griebel et al.[160] derived strain−stress curves of selected a-Si_3BN_5, a-$Si_3B_2N_6$ and a-$Si_3B_3N_7$ models and found that increasing the B content increases the Young's modulus. In this work, I extend the scope of the previous studies by revealing how composition and structure might influence a combination of properties desirable for coating applications. Using a combination of atomistic numerical methods, we screen a library of low enthalpy a-Si−B−N networks (a-Si_3BN_5,

a-Si$_3$B$_3$N$_7$, and a-Si$_3$B$_9$N$_{13}$) to predict from extensive atomistic simulations the thermal conductivity and mechanical stiffness with different BN contents.

3.2 Methods

The initial simulated structures were generated and optimized with density functional theory (DFT), which was carried out by the group at the University of Texas at Arlington. Due to the large computational costs associated with *ab initio* calculations, I then explored the properties of the *ab initio*-molecular-dynamics-generated networks with interatomic potential energy models. The lower computational cost for the classical Hamiltonian enables a more accurate spatial representation of the disordered networks and more efficient screening of the structure−composition−property relationship. The classical MD calculations were performed with the code LAMMPS[140]. We treat the Si−N and B−N interactions with the bond-order Tersoff potential and parameters given in ref[162]. For Si−Si, N−N, B−B, and Si−B interactions, only repulsion is modeled because these bonds are not present in the *ab initio*-molecular-dynamics-derived structures and are unlikely to appear in experiment[163]. Additionally, it is known that homoelemental N−N bonds are energetically unfavorable[164]. Thermal and mechanical properties of the structures treated with the Tersoff potential were extracted, as described next.

Because a-Si−B−N are insulators electronically, phonons are the main thermal energy carriers. We have computed their thermal conductivity (κ) in the classical limit from long equilibrium MD runs. In preparation for κ measurements, the supercells constructed based on *ab initio* MD annealed structures were first evolved in the isothermal−isobaric ensemble at the desired temperature and a pressure of 0 bar for 375 ps, then in the canonical ensemble for 225 ps, and finally in the microcanonical ensemble for another 205 ps in order to achieve good equilibration. We compute the instantaneous microscopic heat current on the MD-generated microstates and then κ was extracted with the Green−Kubo formula (see Chapter 1). Each MD time step is 0.15 fs long.

To gain insight into the mechanical behavior, we have examined the response to applied strains of a-Si−B−N structures described with the same Tersoff potential. Since the analysis is focused on the linear regime, we simulated cells with ∼1 nm side lengths placed under periodic boundary conditions. External strain was applied by elongating the simulation box size in one direction by 0.02 Å at each iteration, followed by conjugate gradient energy minimization. The specimens were allowed to shrink or expand in the other two directions to ensure that the system is under uniaxial loading. The corresponding potential energies were then recorded for each step of strain. The stress and Young's modulus (Y) along a specific direction were calculated from the first and second derivatives of the total potential energy with respect to the strain,

normalized by the cross-sectional area. For each considered structure, external strain was applied in all three Cartesian directions.

3.3 Structures and Energetics of Amorphous Silicon-Boron-Nitride Networks

Figure 20 and Figure 21 present the collection of structures that will be considered in this study. It can be seen that the process of searching for local minima generates nearly cubic unit cells containing about 100 atoms. Lattice parameters, densities of selected structures at each considered stoichiometry, and numbers of undercoordinated atoms are presented in Table 3-1. According to our definition, Si, B, and N atoms are undercoordinated if they have fewer than four (Si), three (B), and three (N) first neighbors within the cutoff distances, which are set as 20% larger than the experimental values of Si−N and B−N bond lengths of 1.72 Å and 1.43 Å, respectively[23]. We see that, for all values of χ, the employed *ab initio* MD generation procedure gives models with very few or no undercoordinated atoms.

The network generation process produces nearly homogeneous a-Si−B−N structures. Only when second-nearest neighbor statistics are examined do these structures present a slight trend for B-N-B preference[165]. However, for the high BN

content structure $Si_3B_9N_{13}$, we also find segregation of h-BN layers. Figure 21 shows examples of model structures without (models 1−3) and with (models 4−6) h-BN layers containing Si atoms. It can be observed that the h-BN layers are connected by covalent S−N and B−N bonds. Similar BN phase segregation was found previously in B-doped Si_3N_4/SiC ceramics[166].
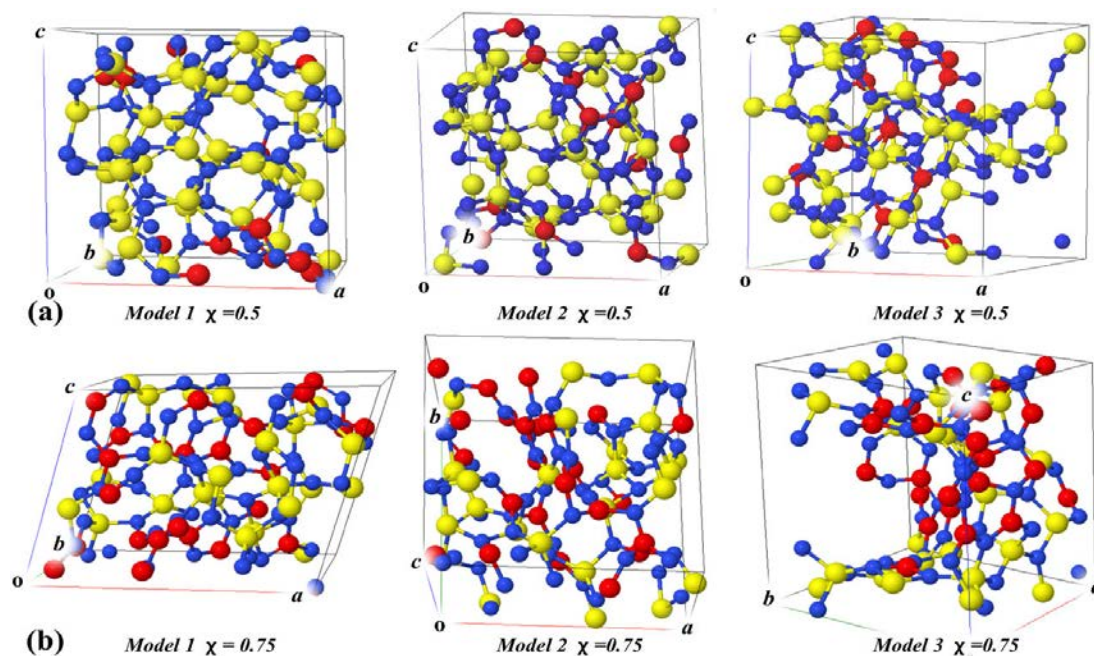
Figure 20. Unit cells of (a) a-Si_3BN_5 ($\chi = 0.5$) and (b) a-$Si_3B_3N_7$ ($\chi = 0.75$) models. Models 1−3 are nearly homogeneous. Color scheme: Si (yellow), B (red), N (blue).
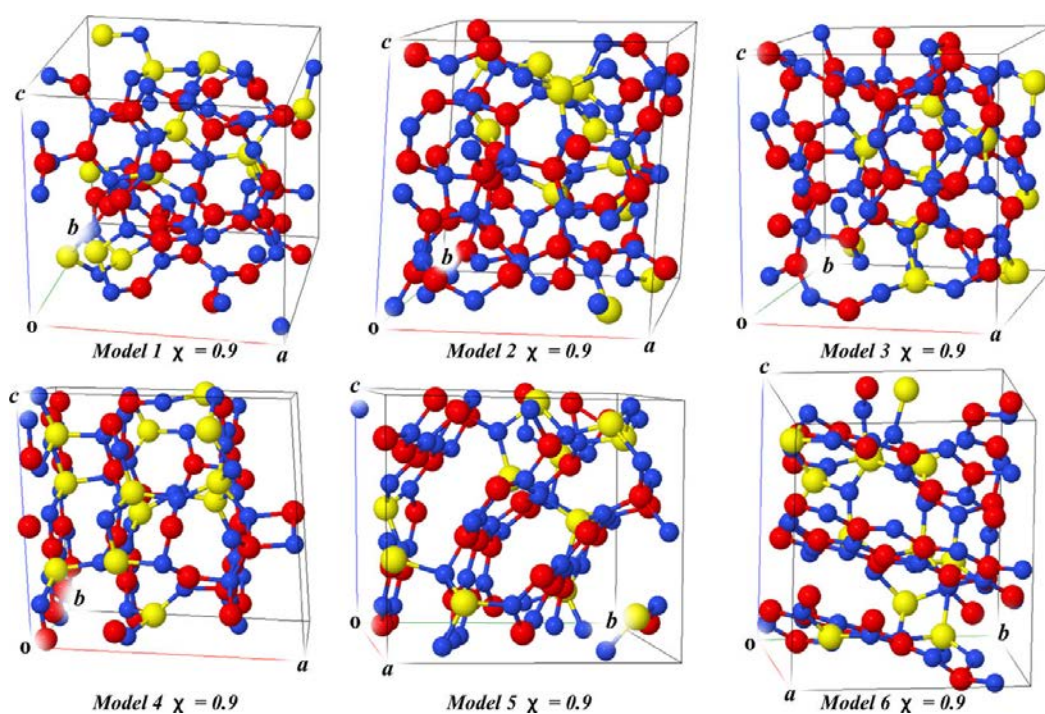
Figure 21. Unit cells of a-$Si_3B_9N_{13}$ ($\chi = 0.9$) models. Models 1−3 (top row) are nearly homogeneous. Models 4-6 (bottom row) present h-BN segregation. Color scheme: Si (yellow), B (red), N (blue).

Table 3-1. Comparison of Selected a-Si−B−N Cells with Different χ Values, Described with DFT and Tersoff Models

χ	0.00	0.50[a]	0.75[a]	0.90[a]	1.00
Number of Atoms	112	108	104	100	256
Lattice Lengths					
a (Å)	12.05	10.49	12.32	10.19	13.06
b (Å)	10.12	10.27	9.35	9.99	12.52
c (Å)	9.75	10.22	9.24	9.31	12.77
Lattice Angles					
α (deg)	85.62	88.78	95.85	83.54	88.05
β (deg)	88.61	91.78	70.97	91.31	93.17
γ (deg)	95.62	87.44	98.27	88.75	88.69
Density (g/cm^3)	3.16	2.99	2.87	2.57	2.53
DFT Model[b]					
ΔH_f (eV/atom)	0.21	0.24	0.32	0.26	-

Number of UC atoms[c]	3	0	0	0	0
Tersoff Model					
ΔH_f (eV/atom)	0.31	0.24	0.14	0.08	0.26
Number of UC atoms	2	0	0	0	1

a) Model 1 in Figure 26 and Figure 27 (b).
b) With van der Waals correction.
c) UC stands for undercoordinated atoms.

Because of the h-BN segregation effect, we have also included in our study BN-rich structures that were not fully relaxed. Specifically, we have considered an a-BN system taken from the very first annealing cycle after the model obtained after 7 ps in an *ab initio* MD at 2200 K was relaxed. This "intermediate" model, listed in the last column of Table 3-1, serves the purpose of having a balance between three- and four-fold-coordinated B.

The DFT energies $E_{a-\text{SiBN}}$ of the computed networks cannot be used directly to compare the stability of structures with identical compositions. The relative stability of structures with different compositions depends on the way the structural parts BN and Si_3N_4 mix to form the network. Therefore, we follow here the approach of binary-phase

thermodynamics and define for the quasi-binary composition $(BN)_\chi(Si_3N_4)_{1-\chi}$ a per-atom enthalpy of formation, ΔH_f:

$$\Delta H_f = \frac{E_{a-SiBN}(\chi) - n_p\left[(1-\chi)E_{Si_3N_4} + \chi E_{BN}\right]}{n_a} \qquad (3\text{-}1)$$

Here n_p is the number of BN and Si_3N_4 parts in the structures. For example, a-$Si_3B_3N_7$ comprises three parts BN and one part Si_3N_4. Thus, $n_p = 4$ and $\chi = 0.75$. We propose to measure ΔH_f with respect to the crystalline β-Si_3N_4 and h-BN phases. Thus, we take $E_{\beta-Si_3N_4} = -58.69$ eV and $E_{h\text{-}BN} = -17.89$ eV, which are the energies computed with DFT. n_a is the number of atoms in one a-Si−B−N unit.

Figure 22 plots the calculated ΔH_f for selected network structures with lowest DFT energies at each considered χ. Our data do not reveal significant distinctions in the thermochemical stability of the structures with various χ values. The $\chi = 0.9$ structures emerge as only slightly more stable than the $\chi = 0.75$ ones. The different models with the same χ values are close in energy. As can be noted from Figure 20, models 2 and 3 with $\chi = 0.75$ present rather large voids in their network structure. This structural aspect is not reflected in the ΔH_f values, which were both calculated as 0.33 eV/atom. A similar observation about the role of structure can be made at $\chi = 0.9$, where we identified significant segregation of the h-BN layers: In Table 3-2, we compare $\chi = 0.9$

structures with and without h-BN layer segregation. It can be seen that both structure types present similar densities and ΔH_f values.
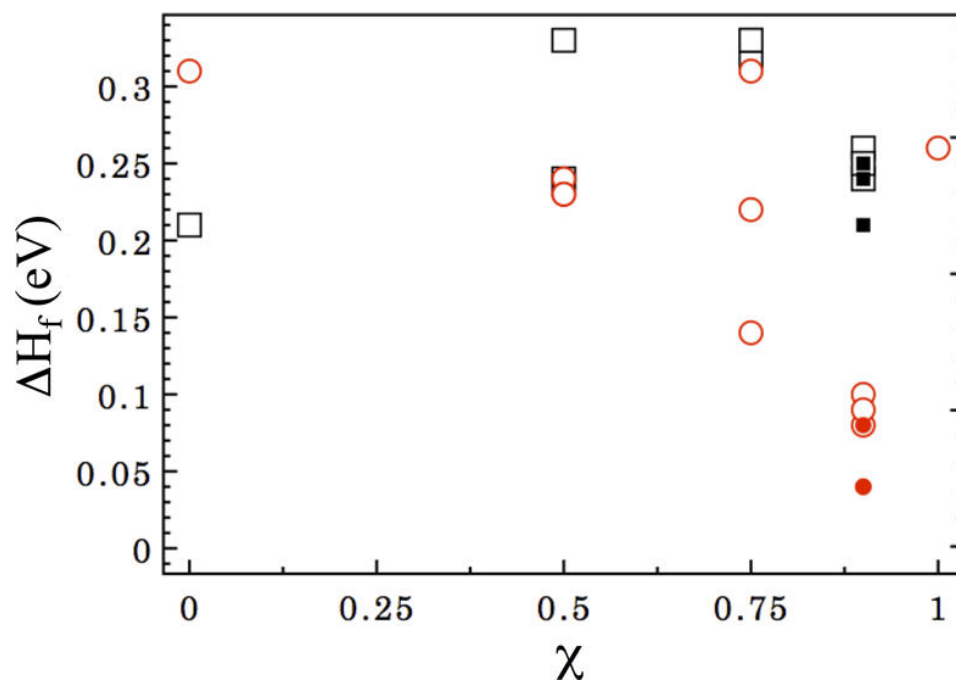
Figure 22. Per-atom enthalpies of formation of $(BN)_\chi(Si_3N_4)_{1-\chi}$ structures plotted as a function of χ, which is the BN molar fraction. Red circles represent the Tersoff data, while black squares show the DFT data. Open symbols refer to nearly homogeneous structures, while solid symbols refer to structures presenting h-BN layer segregation.

Table 3-2. Comparison of $\chi = 0.9$ Cells Described with DFT and Tersoff Models[a]

	Model					
	1	2	3	4	5	6
Number of atoms	100	100	100	100	100	100
Lattice Lengths						
a (Å)	10.19	9.43	9.70	10.25	9.26	9.88
b (Å)	9.99	9.84	9.90	9.36	10.47	9.06
c (Å)	9.31	9.76	9.82	9.37	9.17	9.97
Lattice Angles						
α (deg)	83.54	85.44	89.15	87.82	91.47	88.94
β (deg)	91.31	86.84	88.21	94.66	89.61	93.46
γ (deg)	88.75	90.64	91.52	95.59	86.94	89.42
Density (g/cm³)	2.57	2.68	2.56	2.71	2.72	2.71
DFT Model[b]						

ΔH_f (eV/atom)	0.26	0.24	0.25	0.24	0.25	0.21
Number of UC atoms[c]	0	0	0	1	1	0
Tersoff Model						
ΔH_f (eV/atom)	0.08	0.10	0.09	0.08	0.04	0.04
Number of UC atoms	0	0	0	7	1	0

a) Model 1 – 3 are nearly homogeneous. Models 4−6 present h-BN segregation. All these models were considered in Figure 26 and Figure 27 (b). The unit cells for these models are shown in Figure 21.
b) With van der Waals correction.
c) UC stands for undercoordinated atoms.

We next investigated these network structures with the Tersoff potential description. The atomic positions were further allowed to relax via energy minimization to the new equilibrium positions. The stopping tolerance for energy is 1.0×10^{-8} eV and that for force is 1.0×10^{-8} eV/Å. From Tables 3-1 and 3-2, it can be seen that the relaxed structures present very few undercoordinated atoms, a feature that is in agreement with the original DFT network structures. The energies of the relaxed structures were used to compute ΔH_f. For consistency, we used as reference values $E_{\beta-Si_3N_4} = -38.46$ eV and $E_{h-BN} = -15.13$ eV, which are the per-unit energies computed with Tersoff potential. As can be seen from Figure 22 and Tables 3-1 and 3-2, the ΔH_f values computed with the Tersoff potential are generally in good agreement

with the DFT values. There is a trend of the Tersoff model to underestimate (overestimate) ΔH_f at large (small) χ.

We have also probed the structural description of a-Si−B−N networks in the MD context. We have evolved, at 300 K for 100 ps, our set of a-Si−B−N structures with a velocity Verlet algorithm and a 0.15 fs time step, and we have characterized the atomistic structure of the homogeneous a-Si−B−N networks by computing the radial distribution function (RDF). RDF describes the likelihood of finding a neighboring atom in the spherical shell of a central atom. The interatomic potential cutoff radii in our simulations are 2.62 and 1.79 Å for Si−N and B−N interactions, respectively. As shown in Figure 23, only Si−N and B−N bonds are located within the potential cutoff radius. We note also that, for the $\chi = 0.75$ structure, the RDF peaks at 1.75 Å for Si−N and 1.47 Å for B−N are very close to the experimental values of 1.72 and 1.43 Å, respectively[23]. This agreement indicates that the short-range order is well described by our classical MD approach.

Analysis of MD velocity data for the same set of model structures indicated that the added BN bonds should be thermally active, as they show distinct vibrational features in the phonon density of states (DOS) and partial phonon density of states (PDOS). Figure 24 (a) shows that the phonon modes of a-Si_3N_4 are mainly distributed below ~35 THz, while the a-BN phonon modes have a broader frequency range (0−60

THz) with a distinct peak at ~45 THz. With increasing χ, this peak forms and its intensity increases. The PDOS data shown in Figure 24 (b) further reveal that this peak originates in the vibrations of B atoms. We have compared the area under the unnormalized DOS and PDOS spectra to obtain the proportions of phonon modes in the structure due to the vibrations of different atom types. As shown in Figure 24 (c), we find that the portion of B modes increases monotonically with the BN fraction. When we recall that B forms bonds only with N atoms, it follows that this bond proportion effect concerns the B−N bonds. This interpretation is in agreement with the data presented in Figure 24 (d) and (e), where the 45 THz peak can be identified only in the PDOS of N atoms. Note that a previous MD study[23] also reported the vibrational frequency of B−N stretching mode at ~45 THz.
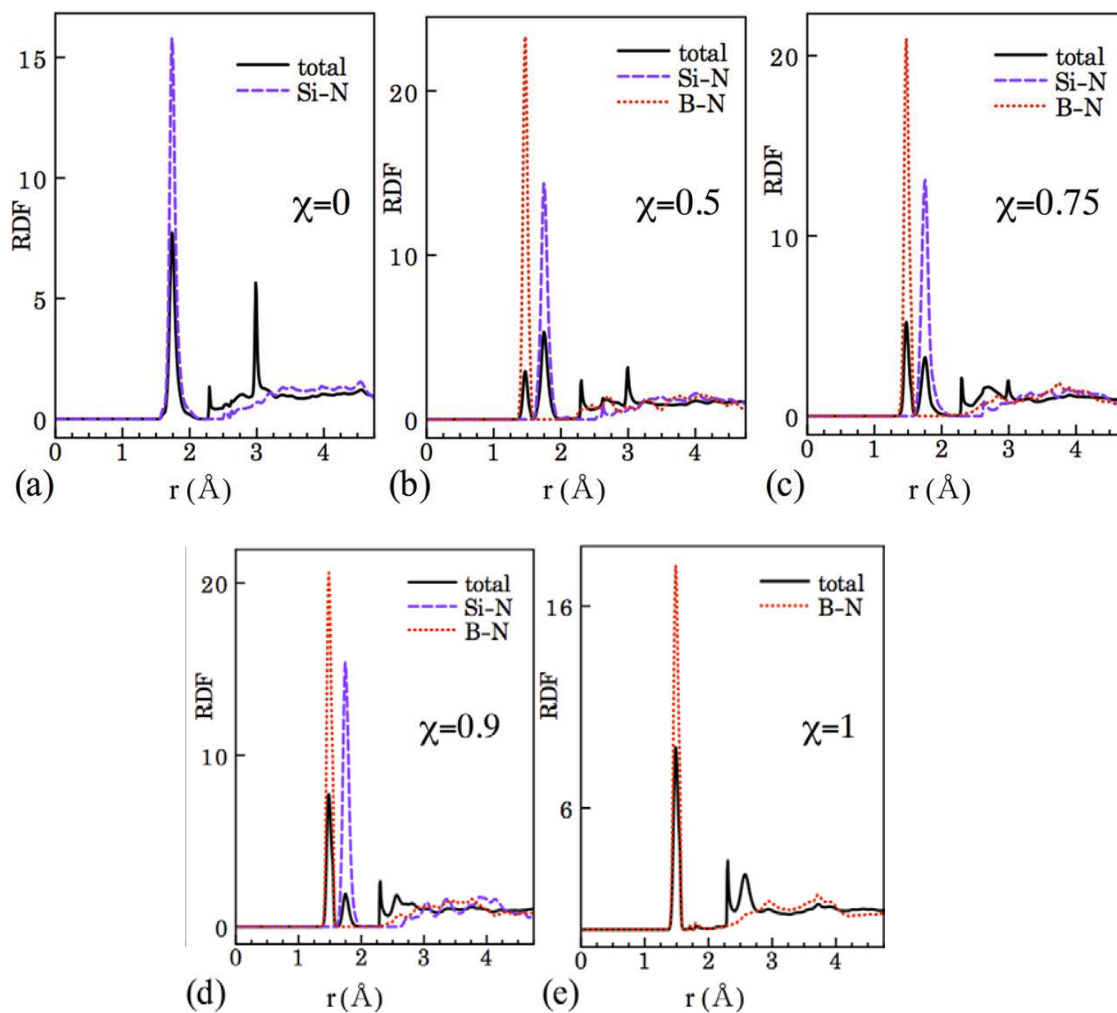
Figure 23. Radial distribution function for a set of a-Si−B−N structures with different χ values: (a) a-Si$_3$N$_4$, $\chi = 0$; (b) a-Si$_3$BN$_5$, $\chi = 0.5$; (c) a-Si$_3$B$_3$N$_7$, $\chi = 0.75$; (d) a-Si$_3$B$_9$N$_{13}$, $\chi = 0.9$; and (e) a-BN, $\chi = 1$.
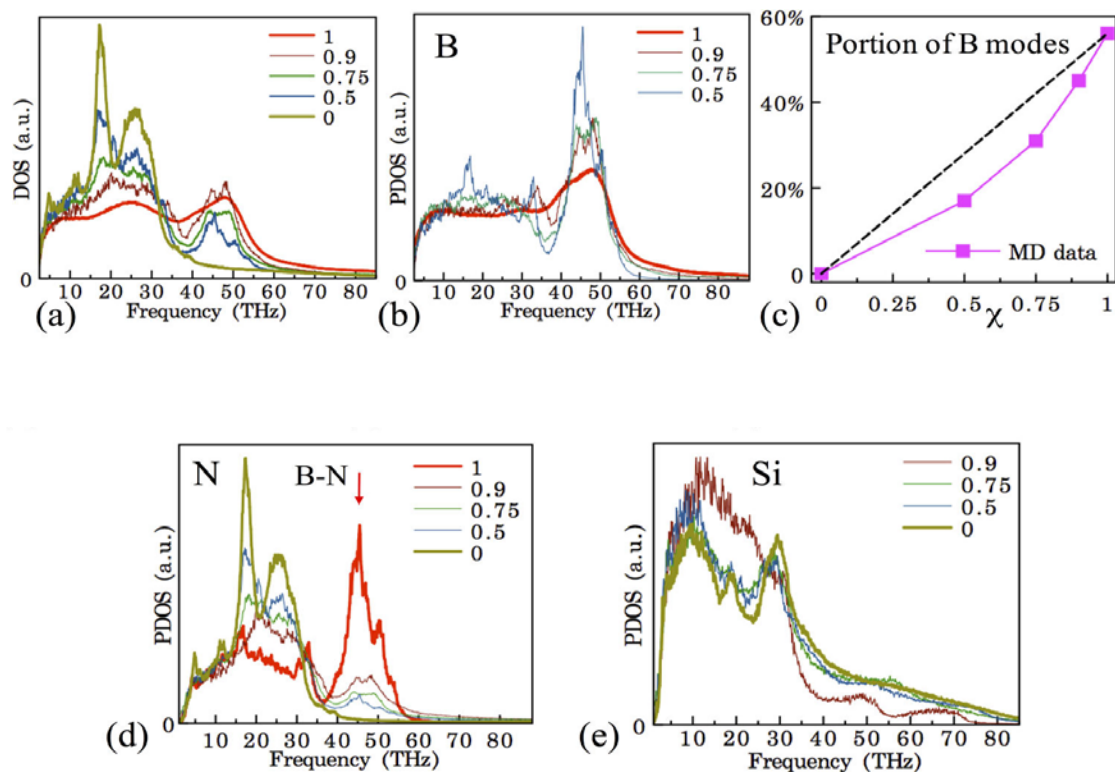
Figure 24. (a) Normalized phonon density of states of a-Si−B−N structures, identified in the legend by their χ values. (b) Partial phonon density of states of B and (c) portion of B modes with respect to all phonon modes as a function of χ. The dashed line connecting the values of the end phases is shown for comparison. (d, e) Partial phonon density of states of (d) N and (e) Si. In panel d, the down arrow points to the B−N stretching model.

3.4 Properties of Amorphous Silicon-Boron-Nitride Networks

Having probed the suitability of the Tersoff treatment for simulating a-Si−B−N films via comparison with our DFT results and the available experimental and MD data, we now turn our attention to utilizing this description for predicting how the atomistic structure and composition influences thermal and mechanical properties.

In our calculations for κ, we have considered only the collection of representative network structures with low enthalpies summarized in Figure 22. This is because even with the efficient Tersoff Hamiltonian, evaluation of κ is still a difficult task. For example, because the ensemble average of the auto-correlation of heat flux exhibits nonergodic long-time oscillations, averaging over multiple MD runs is required[167]. Here, each reported κ value for a given model represents the average κ measured from 20 MD measurement runs, each lasting 100 ps. Error bars represent the standard error based on 20 individual measurements.

We first considered one nearly homogeneous network model for each χ and performed MD simulations at room temperature. Supercells with different side lengths were studied by periodically repeating the optimized cell obtained from *ab initio* MD.

Figure 25 (a) shows an example of the averaged integral of heat flux autocorrelation function for a-Si$_3$BN$_5$ with ~4 nm side length. There is good convergence after $\tau = 5$ ps.

As demonstrated in Figure 25 (b), accounting for finite-size effects is important in predicting κ. The simulation cell size dictates the maximum phonon wavelength present in the simulation. For all χ, κ increases with the supercell size as additional long wavelength phonons become available for heat transport. The crossover behavior observed at ~3 nm suggests that the long-wavelength phonons bring a more significant contribution to κ for a-Si$_3$B$_9$N$_{13}$ than for a-Si$_3$B$_3$N$_7$. When κ converges, at side lengths larger than 4 nm, the κ of a-Si$_3$BN$_5$, a-Si$_3$B$_3$N$_7$, and a-Si$_3$B$_9$N$_{13}$ are calculated as 2.3 ± 0.1, 3.0 ± 0.1, and 3.1 ± 0.5 W/mK, respectively. (Each κ value reported here is the average value of κ_{xx}, κ_{yy}, and κ_{zz}, which means the κ value in x, y and z directions, respectively).

Figure 25 (c) suggests that the BN addition to a-Si$_3$N$_4$ leads to a monotonic increase in κ. The increase is weak, such that a linear interpolation between the values of the binary compounds overestimates the MD-computed κ. This observed trend may be a signature of the fact that h-BN has a larger longitudinal speed of sound than β-Si$_3$N$_4$, that is, 16 km/s[168] *vs.* 9.9 km/s[169]. Although a reduction of these values is expected in the amorphous phases, the speed of sound will still depend on the local
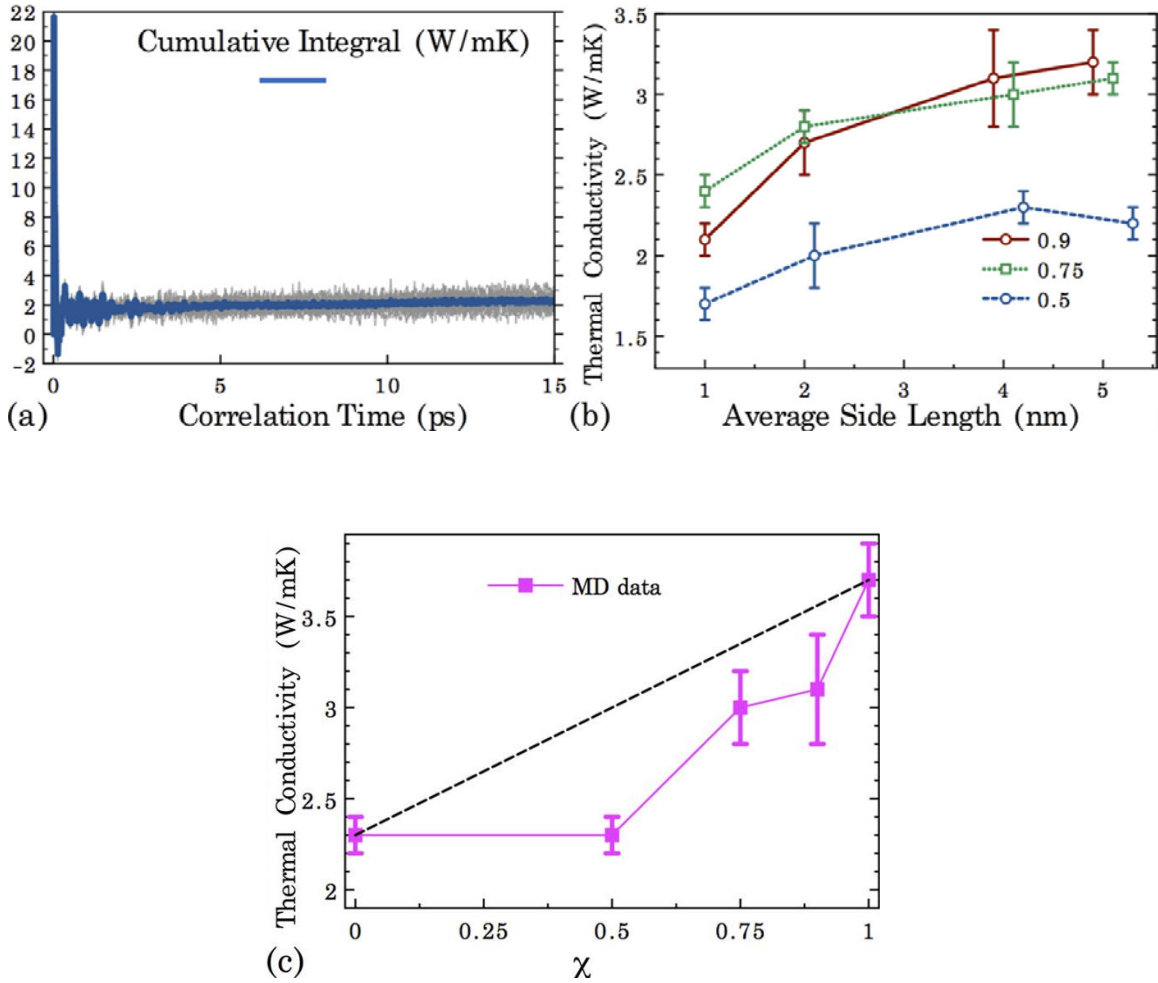
Figure 25. (a) Cumulative integral (blue) of the heat flux autocorrelation function averaged over 20 ensembles (gray) for ~4 nm-sized a-Si_3BN_5 ($\chi = 0.5$). (b) Dependence of κ on supercell size. (c) Dependence of κ on χ. The dashed line connecting the values of the end phases is shown for comparison. The continuous line connecting the data points is to guide the eye. T $\approx$ 300 K.

order and nature of the bonds[170]. (To clarify the connection between κ and the speed of sound, recall that kinetic theory defines κ as $1/3 C_v v_g l$, where C_v and l denote the specific heat and phonon mean free path, respectively. The phonon group velocity v_g for heat-conducting long-wavelength phonons is approximately the speed of sound. This

relationship predicts the minimum κ of a material at high temperatures, in which case C_v is close to a χ-independent constant and l approaches the interatomic spacing limit[171,172].)

Our further investigations focused on the network-model dependence of κ. Figure 26 shows that the computed κ values for our collection of nearly homogeneous models (models 1−3 for each χ) are all contained in the 2.0−3.5 W/mK range. Overall, this plot shows that while κ has a weak dependence on the network model representation, the variation of κ from different models is larger than, or on the same
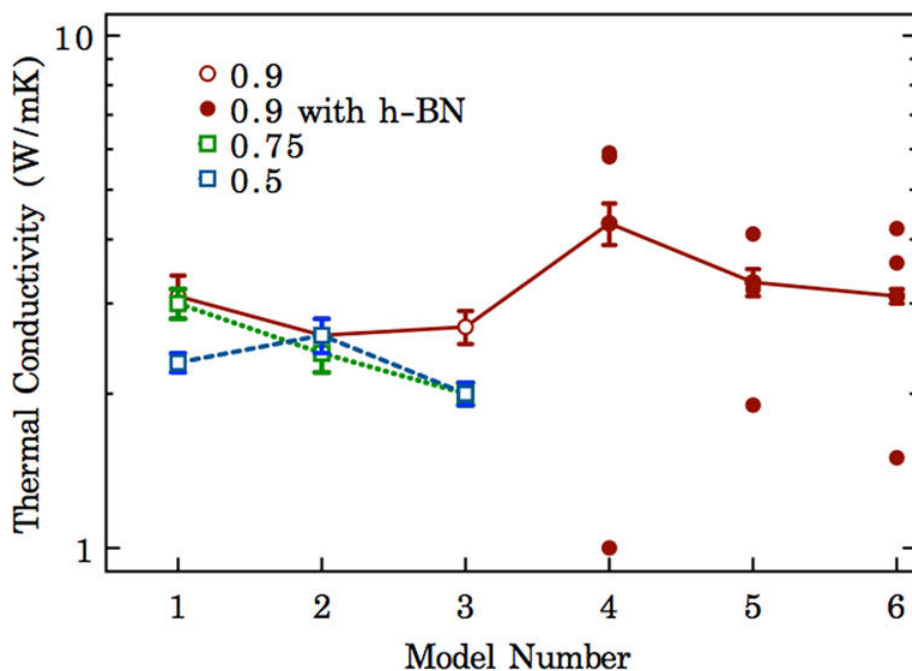
Figure 26. Structure dependence on thermal conductivity of a-Si_3BN_5 (χ = 0.5), a-$Si_3B_3N_7$ (χ = 0.75), and a-$Si_3B_9N_{13}$ (χ = 0.9). The horizontal axis refers to the network model number. Lines connect κ points with the same χ value. For models 4−6 with χ = 0.9, we have also plotted the values of diagonal elements of the thermal conductivity matrix.

order as the standard error resulting from κ computation by the Green−Kubo method. Thus, to gain an ensemble representation, further averaging of the individual values for models with the same χ was performed. The obtained values, listed in the first line of Table 3-3, maintain the already noted trend of a weak increase of κ with χ.

Table 3-3. Model-Averaged Thermal Conductivity and Young's Modulus as a Function of $\chi^{a)}$

χ	0.50	0.75	0.90
κ (W/mK)	2.3 ± 0.2	2.5 ± 0.4	2.8 ± 0.2
Y (GPa)	209 ± 30	203 ± 32	239 ± 25

a) For each value of χ, models 1−3 have been considered as an average.

In contrast with the nearly homogeneous models, the h-BN segregation in χ = 0.9 models has a significant impact on thermal transport. In Figure 26, it can be seen that the individual κ values for models 4−6 are greater than the values obtained for models 1−3. This increase is associated with a significant increase in κ anisotropy, which can be seen in Figure 26. Model 4 provides a good example for observing anisotropy, since the h-BN layers are oriented along the x direction. On one hand, in the y and z directions we obtained $\kappa_{yy} = 5.9 \pm 0.3$ W/mK and $\kappa_{zz} = 5.8 \pm 0.4$ W/mK. These values are significantly larger than the κ of a-BN due to the crystallinity of the formed h-BN layers. On the other hand, in the x direction we obtained $\kappa_{xx} = 1.0 \pm 0.1$

W/mK, a value that falls well below κ_{yy} and κ_{zz} and that is comparable with the thermal conductivity across layers in h-BN[173]. For comparison, the diagonal elements calculated for model 1 with $\chi = 0.9$ are $\kappa_{xx} = 3.6 \pm 0.3$ W/mK, $\kappa_{yy} = 2.7 \pm 0.3$ W/mK, and $\kappa_{zz} = 3.0 \pm 0.2$ W/mK.

We have screened the elastic properties for the same collection of structures. Figure 27 (a) presents the computed stress–strain curves for selected nearly homogeneous networks with different χ values. While different slopes are associated with the different χ structures, we see that the network elasticity is not increasing monotonically with the concentration of added stiff B–N bonds. This is likely a signature of the specific structural environment seen by the atoms, a situation causing nonaffinity in deformation. As can be noted from Figure 27 (b), the model-specific Y values fluctuate in the 170–270 GPa interval. The elastic behavior of models 1–3 is isotropic. This transpires from the error bars, which represent the standard error based on measurements performed in the three Cartesian directions. For a more realistic representation of Y as a function of χ, we have performed averaging of the values given by the different models. The Y values, listed in the second line of Table 3-3, suggest a weak increase of Y with χ. We also note that the obtained Young's modulus for a-$Si_3B_3N_7$ is in very good agreement with the *ab initio* prediction (~200 GPa) given in Ref[163].
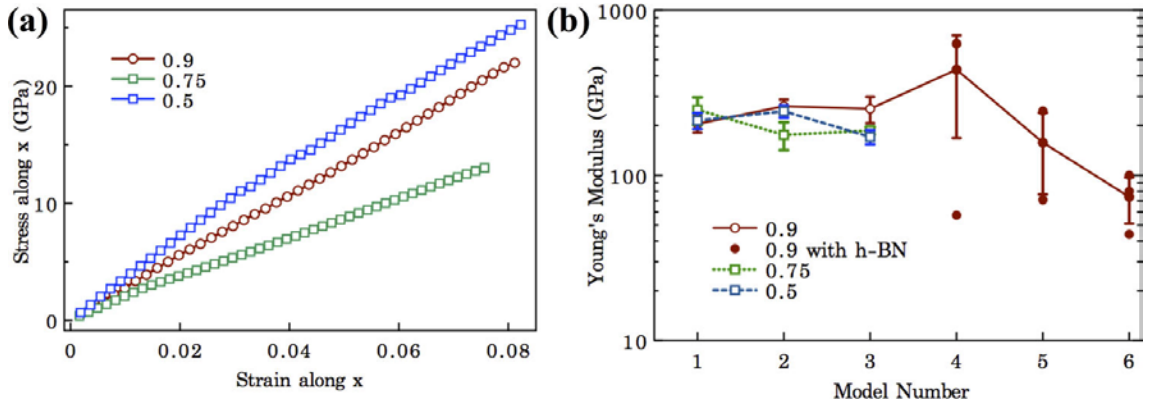
Figure 27. (a) Selected stress−strain curves and (b) structure dependence of Young's moduli of a-Si_3BN_5 ($\chi = 0.5$), a-$Si_3B_3N_7$ ($\chi = 0.75$), and a-$Si_3B_9N_{13}$ ($\chi = 0.9$). In panel b, the horizontal axis refers to the network model number. Lines connect data points with the same χ value. For models 4−6 with $\chi = 0.9$, we have also plotted the values of diagonal elements of the Y matrix.

In Figure 27 (b), it can be seen that h-BN segregation in the $\chi = 0.9$ model has a strong effect on Y. For models 4−6, it can be seen that the diagonal components of Y present very different values. For example, for model 4 in the y and z directions, we obtained $Y_{yy} = 623$ GPa and $Y_{zz} = 628$ GPa. Such large values can be expected along the h-BN layers. On the other hand, in the x direction we obtained $Y_{xx} = 57$ GPa, a value that falls significantly below the Y values computed for the nearly homogeneous networks. Moreover, we observed that this structure exhibits failure at elongation strains of only 4%, when the covalent bonds connecting the layers break.

3.5 Conclusion

In summary, a-Si−B−N ceramics with different BN content (a-Si$_3$BN$_5$, a-Si$_3$B$_3$N$_7$, and a-Si$_3$B$_9$N$_{13}$) were modeled as chemically ordered random covalent networks with a computational protocol that involved *ab initio* MD simulations. The a-Si−B−N networks obtained this way exhibit very few or no undercoordinated atoms and a weak variation in thermochemical stability. Furthermore, atomistic simulations based on Tersoff potentials were performed to evaluate κ and Young's moduli of the network models obtained by *ab initio* MD simulations. For each composition, it was necessary to average κ and Y over different network models. The main finding of this investigation is that thermal and mechanical properties depend weakly on the BN content, as long as the network structure lacks segregation into h-BN layers.

Understanding the relationship between composition and thermal and mechanical properties is of great importance for developing a-Si−B−N coatings able to provide protection against thermal impact and mechanical loads. The principal conclusion of the presented investigation is that it is unworthy to pursue compositions as high as χ = 0.9 (a-Si$_3$B$_9$N$_{13}$). This is because large χ promotes BN layer segregation, an effect that severely weakens the structure in the cross-layer direction and increases thermal conductivity along the layer direction. Instead, our study identifies χ = 0.5 (a-

Si_3BN_5) and $\chi = 0.75$ (a-$Si_3B_3N_7$) as the compositions least prone to segregation into h-BN layers. These compositions exhibit a combination of low thermal conductivity and large mechanical stiffness suitable for coating applications. The methods of investigation used here show promise for studying the composition−structure−properties relationship in more complex quaternary amorphous ceramics[26,174–176]. Furthermore, the results can be applied in multiscale simulation frameworks[177,178] to enable system-scale predictions for mechanical behavior.

Chapter 4

Thermal Transport in Deformed Carbon Nanotubes

The carbon nanotubes' resilience to mechanical deformation is a potentially important feature for imparting tunable properties at the nanoscale. Using nonequilibrium molecular dynamics and empirical interatomic potentials, we examine the thermal conductivity variations with bending and collapsing in the thermal transport regime where both ballistic and diffusive effects coexist. These simulations are enabled by the realistic atomic-scale descriptions of uniformly curved, buckled and twisted nanotube morphologies obtained by imposing objective boundary conditions. The study of bent carbon nanotubes has been completed and published in Ref[63,64,179]. The study of the flattened carbon nanotube is in preparation.

4.1 Introduction

The combination of extremely high thermal conductivity[31–34,180,181] (κ) and exceptional mechanical properties[36,38,39,182–186] of carbon nanotubes (CNTs) motivated the usage of this material for developing a variety of applications, including multifunctional materials[187,188], thermal switches, and thermal interface materials[44,45,189]. Their tube-like structures are susceptible to buckling[36,65,182,186,190–192] and collapsing[52–61]. When a SWCNT bends, it does not break. Instead, the strain energy is lowered by the formation of a structural kink[35,36,179,190,191,193].The relation between the thermal transport and the bending deformation modes of single-walled carbon nanotubes (SWCNTs) had not been well established. Little investigation has been done on the thermal transport along flattened SWCNTs. The potential effects of bending and buckling are important for the fundamental understanding of phonon scattering mechanisms in quasi-one dimensional structures as well as for applications.

4.2 Thermal Transport in Single-walled Carbon Nanotubes Under Pure Bending

The κ of stress-free SWCNTs extends from ballistic to diffusive throughout a range of temperatures and diameter-dependent lengths[180]. We are concerned with the thermal conductance regime exhibited by SWCNTs with lengths (l) less than the phonon mean free path (l_{MFP}). In this regime, atomistic molecular dynamics (MD) simulations[181,191,193] performed on SWCNTs up to hundreds of nanometers in length obtain that κ increases with length. The increase demonstrates the substantial contributions to thermal transport of the additional long-wavelength phonons created by increasing the SWCNT length[194]. The mechanics of CNT bending is well understood, and there is good quantitative agreement between theory and experimentation. For example, the observed critical strains for wavelike rippling[193] of multiwalled CNTs are only within a few percent of the modeling predictions[35,190]. In contrast, in the thermal domain, no uniform conclusion has been reached, even qualitatively. Experiments[46,47] uncovered the robustness of heat transport along bent CNTs in both the diffusive and the ballistic regimes. In contrast, theoretical studies[48–50,195] considering the ballistic regime have revealed that bending and buckling cause κ reductions.

There could be several reasons for the discrepancy between the experimental and theoretical results. A first explanation suggests that κ reductions could be related to the challenges in simulating a bent SWCNT at the atomistic level. Indeed, the standard MD formulation under periodic boundary conditions is unusable since bending is incompatible with translational symmetry. For this reason, researchers often rely on finite-size cluster representations, by considering SWCNTs as long as 50 nm. A bending deformation is usually imposed by rotating the two ridged ends to a target angle. Besides the disadvantage of introducing spurious effects, the procedure leads to deformed nanotubes with small bending portions (typically 8 nm long) and large straight ends[48]. Such morphologies are not similar with the ones investigated in experiment[196], where the bent portions are approaching the mean free path of the SWCNT. A related explanation brings up the observed diameter and length dependence for the onset of buckling[190]. The condition for buckling is fulfilled earlier in longer and large-diameter SWCNTs. If thermal transport is strongly influenced by bending, only large-diameter SWCNTs might exhibit robust thermal transport since less geometrical curvature and strain effects are needed to develop buckling. A final explanation invokes the differences in SWCNT length considered in experiments and current MD simulations. While experiments are probing the ballistic regime near its upper limit, simulations are considering tube lengths l well below l_{MFP}. The SWCNT length limits the longest possible phonon wavelength that can exist. The origin of the discrepancy

may originate in the contribution of the low frequency phonons that are not accounted for in the MD simulations considering short tubes. We find that the conjuncture of the first and last explanations is correct. By increasing the lengths of the considered bent SWCNTs closer to l_{MFP}, our MD simulations predict that thermal transport becomes insensitive to buckling deformation.

To simulate realistically bent SWCNTs, we employ the generalization of periodic MD termed objective MD[106,109,197]. With this method, the whole simulated SWCNT is in pure bending, which represents a condition of stress where only a bending moment is applied. Our objective boundary conditions write

$$r_{i,\zeta} = R^{\zeta} r_i, \qquad i = 1, 2, 3, \dots, N. \tag{4-1}$$

Here, N is the total number of atoms located at positions r_i located in the primary cell. $r_{i,\zeta}$ represents the positions of the corresponding atoms in the image cell indexed by ζ, and R denotes the applied rotation of angle θ performed around the z axis, which is the rotation axis. As θ is the only constraint imposed here, the atoms are free to move away or towards the rotational axis. The curvature s of the SWCNT, then, is not imposed, but here, N is the total number of atoms located at positions r_i in the primary cell. $r_{i,\zeta}$ represents the positions of the corresponding atoms in the image cell indexed by ζ, and R denotes the applied rotation of angle θ performed around the z axis, which is the rotation axis. As θ is the only constraint imposed here, the atoms are free to move
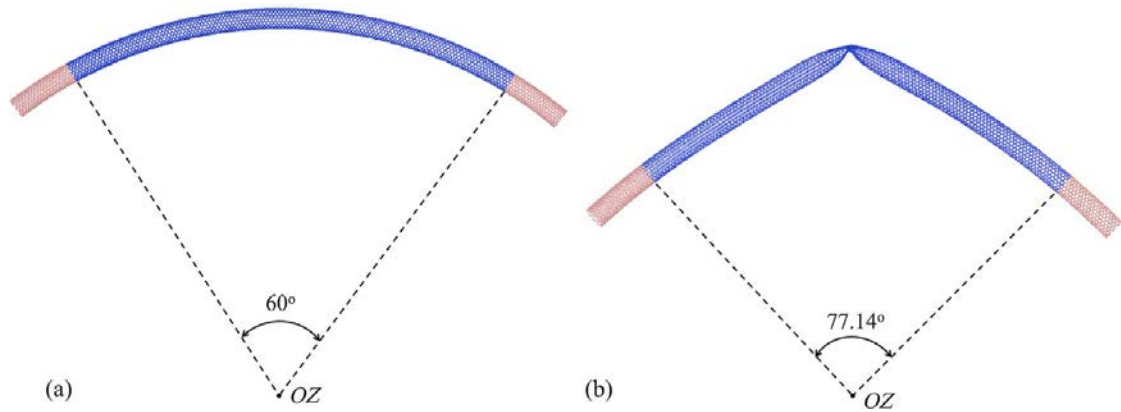
Figure 28. Objective MD configurations of a (10,10) SWCNT bent (a) without and (b) with a kink. The atoms located inside the simulation cell are represented in blue. Atoms in the $\zeta = -1$ and $\zeta = 1$ image cells are shown in pink. The measured curvatures are (a) 0.034 **nm^{-1}** and (b) 0.044 **nm^{-1}**.

away from, or towards, the rotational axis. The curvature s of the SWCNT, then, is not imposed, but it is the result of energy minimization. By varying θ, we are able to generate bent SWCNTs with different curvatures. For example, Figure 28 (a) shows a bent morphology of a (10,10) SWCNT supercell with $l = 30.75$ nm containing 5000 carbon atoms. The bending angle is $\theta = 60$ deg, and the shape of the relaxed bent tube is nicely smooth. The curvature defined as $s = \theta / l$ is everywhere 0.106 nm^{-1}.

In an earlier work[190] , it had been demonstrated that, in spite of the imposed objective periodicity, objective MD is able to describe the expected localized buckling of SWCNTs and all related essential details, including scaling with diameter and length of the critical curvature beyond which SWCNTs behave nonlinearly. Building on this work, which considered SWCNT supercells up to 16 nm in length, here we report that

the method can capture bending and localized kinking of much larger SWCNT portions. Referring to Figure 28, as we further increase θ, a single kink develops as shown in Figure 28 (b) for $\theta = 77.14$ deg. Using this approach, we build a collection of bent structures comprising (10,10) and (6,6) SWCNTs up to 90 nm in length.

Relying on the objective bent morphologies, we perform nonequilibrium molecular-dynamics (NEMD) simulations[140] to understand the thermal transport. The interatomic interactions are described with the adaptive intermolecular reactive empirical bond order (AIREBO) potential[198], which includes a Lennard-Jones term describing the van der Waals interactions experienced by the C-C atoms located in the 2–10.2 Å space interval. The nonbonded interactions at the kink should manifest into an increase of the phonon scattering rate. The proposed NEMD simulation setup is shown in Figure 29 (a) for a (10,10) SWCNT. One unit cell at each end is fixed in order to impose the bending constraints. Such a small size is sufficient in view of the short range of the potential. Four other unit cells next to each end are set as the hot and cold heat baths, respectively. In order to minimize the thermal boundary resistance effect, the length of the bath regions is increased in the subsequent calculations involving (10,10) SWCNTs. We use six unit cells for $l \leq 55.4$ nm, 12 unit cells for $l = 65.2$ nm, and 18 unit cells for $l = 90$ nm. The time step that we use in the NEMD simulations is 0.5 fs. Initially, the whole dynamic system is equilibrated at 300 K with the help of a Nose-Hoover thermostat. Next, the temperatures of the two heat baths are rescaled at

every time step to maintain T_h = 310 K and T_c = 290 K, respectively. The velocity Verlet algorithm is used for time integration. A steady state is reached after 1000 ps. The rate of kinetic energy exchange between the two baths is obtained as

$$Q = \frac{1}{2} \langle Q_h - Q_c \rangle \tag{4-2}$$

Here Q_h and Q_c are the instantaneous heat currents flowing into and away from the hot and cold baths to maintain the temperature gradient. $Q_h - Q_c$ equals the difference in instantaneous kinetic energies of the atoms located in the hot and cold bath regions. The angle brackets indicate a statistical average taken here over the last 5000 ps after the steady state is reached. The thermal conductivity is then calculated as

$$\kappa = -q \left(\frac{dT}{dx} \right)^{-1} \tag{4-3}$$

where q is the heat current per cross-section area A, and x is the axial position. We define A by assuming a 0.34 nm thickness for a one-atom-thick tube wall. The local temperature T is computed by statistically averaging the kinetic energy of the atoms located on three subsequent unit cells.

We first examine short (in comparison with l_{MFP}) SWCNTs before and after their buckling threshold. We consider SWCNTs with different diameters and lengths to provide an opportunity to probe different curvature regimes.
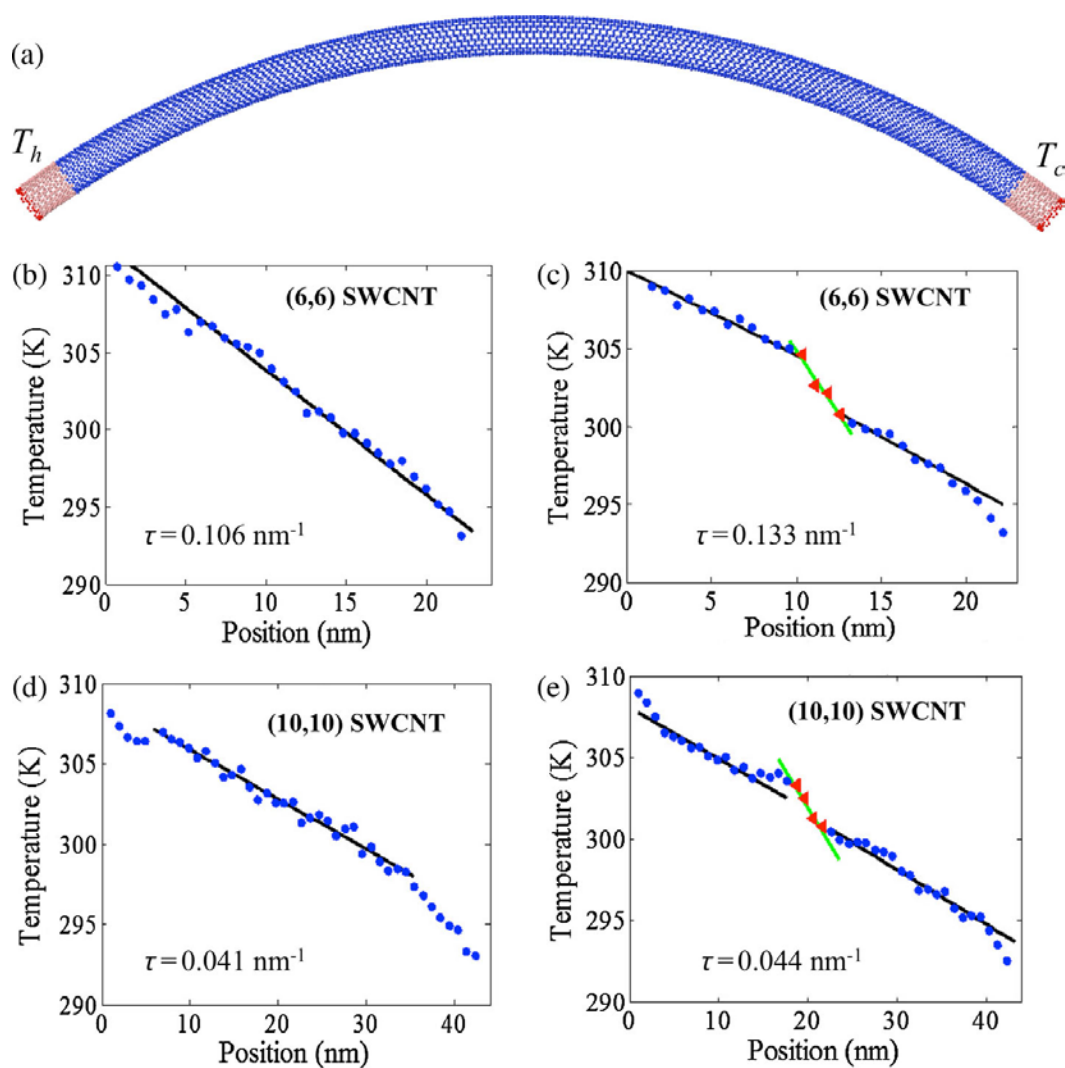
Figure 29. (a) Setup for the NEMD simulation with unidirectional flux. Temperature profiles in bent (6,6) SWCNT, (b) ideal (unkinked), and (c) kinked. The total length is 24.6 nm. Temperature profiles in a bent (10,10) SWNT with (d) ideal (unkinked) and (e) kinked structure. The total length is 45.5 nm. Circles are the local temperatures of the unkinked regions. The red triangles in (c) and (e) represent the temperature in the kink region. Fitted lines are shown in all figures.

Figure 29 (b) – (e) display the obtained temperature profiles along the nanotube length for selected curvatures. For the unkinked cases, we extract the κ by considering the temperature gradient observed in the linear region. We exclude the temperature points from the regime near the thermal baths, since these points are largely affected by the undesirable effect of phonon scattering at the interfaces between thermostatted and nonthermostatted regions. For both SWCNTs, we obtain that the central kink is associated with a pronounced thermal gradient over a length l_k. Unlike the interface effect mentioned above, the thermal resistance at the kink is a real effect. We account for it with a series model, where the overall conductivity writes

$$\frac{1}{\kappa} = \frac{1 - \phi}{\kappa_i} + \frac{\phi}{\kappa_k} \tag{4-4}$$

Here, κ_i and κ_k denote the local thermal conductivities obtained from the slopes identified in the unkinked and kinked regions. $\phi = l_k / l$ is the length fraction of the kinked region. The above model is appropriate since there is no direct interaction between the two SWCNT sections around the kink. There is only one path for the heat flux, through the kink.

Table 4-1 summarizes our simulation results with all considered curvatures. The overall κ values entered in the last column demonstrate that the κ reduction occurs in a gradual manner and that the reduction is small for both nanotubes. By the time the (6,6)

SWCNT develops buckling, we measure a 44 % decrease in κ with respect to the zero-curvature reference case. For the longer and larger-diameter (10,10) SWCNTs, the reduction is of 20 %, which is still significant. (The difference in values reflects the smaller critical curvature for buckling in a larger-diameter SWCNT.) We also see that at the kink location, the local thermal conductivity differs significantly from the rest of the tube. For both nanotubes, κ_k is about 36 % of the unkinked region. For a more transparent characterization of the kink, we estimate the equivalent length of a pristine SWCNT that will give a similar effect. This equivalent length is calculated as $l_k\kappa_0=\kappa_k$, where κ_0 is the pristine thermal conductivity. For the (10,10) CNTs, we find that the equivalent lengths are 11.90 and 20.27 nm, for τ equal to 0.044 and 0.047 nm^{-1}, respectively. Interestingly, these values are larger than the 9-nm value reported for kinks formed under 6 % compressive strain[195].

The thermal resistance at the kink is attributed to the local strain. To gain more insight into the underlying microscopic mechanism, we analyze the local phonon density of states (LPDOS) around the kink and the corresponding region of the unkinked and straight (10,10) SWCNT structures. The LPDOS is obtained by decomposing into Fourier space the MD time-correlation function of the atomic velocities at 300 K. Figure 30 reveals major differences only for the optical G-mode phonons with frequencies around 52 to 54.2 THz (as described with the AIREBO potential[198]). It can be expected that a bending strain affects the G modes since they

correspond to the C-C bond-stretching motion. We see that as s increases, the G peak lowers, broadens, and then splits into two peaks. The shift to lower (higher) frequencies corresponds to a decrease (increase) of the force constants for the C-C bonds elongated (compressed) under the bending deformation. The broadening allows for the optic phonons to provide more scattering channels for the heat-carrying acoustic modes through Umklapp scattering, especially in the acoustic-acoustic-optic scattering, where the sum of two acoustic frequencies must equal the optic frequency. Thus, we conjecture that the MD computed κ lowering with increasing s can originate in the G-band broadening.

Table 4-1. Thermal conductivities of bent (6,6) and (10,10) SWNTs with l much smaller than l_{MPF}. The straight case is shown for a comparison.

SWCNT	l (nm)	s (nm^{-1})	κ_i (W/mK)	κ_k (W/mK)	κ_k/κ_i	ϕ	κ (W/mK)
(6, 6)	24.6	0.000					120.7
		0.106					89.2
		0.133	83.7	29.9	35.7 %	13 %	67.5
(10, 10)	45.5	0.000					155.8

0.034					154.5
0.041					146.4
0.044	143.2	51.5	36.0 %	8.7 %	124.1
0.047	141.4	30.2	21.4 %	8.7 %	107.1

We now examine the consequences of increasing l in order to probe the explanation which attributes the κ robustness to the additional low-frequency acoustic phonons that emerge as $l \sim l_{MFP}$. In Figure 31, we compare the size dependence of κ for a (10,10) SWCNT in the straight and bent (with $s = 0.034$ nm^{-1} and $s = 0.047$ nm^{-1}) states. Relying on the recent detailed investigations[199], we adopt the view that in NEMD simulations with unidirectional heat flux, the whole SWCNT length determines thermal conductivity. Thus, in Figure 31, we plot κ against l, which comprises the heat bath regions. We see that as the sample length increases, the maximum allowable phonon wavelength increases. For the stress-free tubes, we attribute the κ increase with length to the effective contribution of the long-wavelength phonons. We also see that there is no distinction in the conductivity variations of the straight and ideally bent states, suggesting that the transport in ideally bent SWCNTs is ballistic, as in the stress-free

case. Finally, our data demonstrate that the impact of the kink diminishes quickly as l

increases.
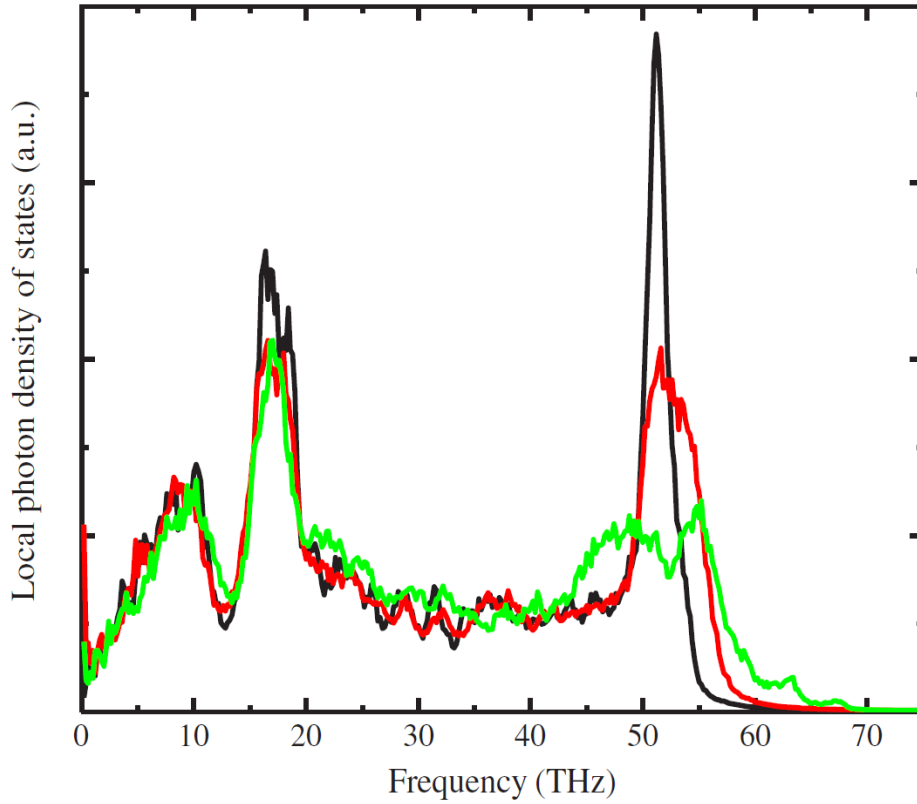
Figure 30. LPDOS in a 45.5-nm-long (10,10) SWCNT as a function of frequency, for a straight structure shown as a black curve, an unkinked bent structure with $s = 0.034$ nm^{-1} shown as a red curve, and a kinked bent structure with $s = 0.047$ nm^{-1} shown as a green curve. LPDOS is calculated over a portion comprising nine unit cells.

While for $l = 24.8$ nm, κ differs by 38 % from the ideal straight state; at $l = 90$

nm, the difference reduces only to 5.7 %. Thus, our simulations confirm the robustness

of the thermal transport observed in experiments. Note that our MD-calculated thermal

conductivities do not include quantum effects. The quantum-corrected κ are estimated[200] as 84 % of those presented in Figure 31. The quantum-corrected temperature is 260 K when the MD temperature is 300 K.
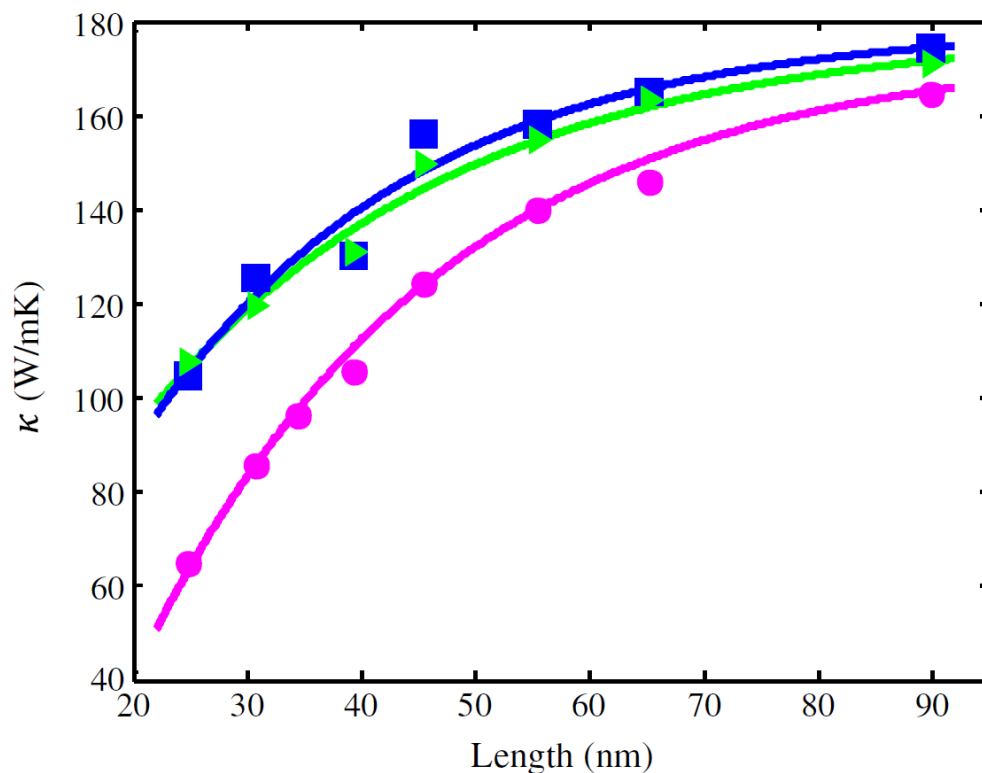
Figure 31. Thermal conductivity in a (10,10) SWCNT as a function of the sample length, for the following structures: straight, blue squares; bent (unkinked) with s = 0.034 nm^{-1}, green triangles; and bent (kinked) with s = 0.044 nm^{-1}, magenta circles. Lines represent exponential fitting of the length dependence.

4.3 Thermal Transport in Flattened Single-walled Carbon Nanotubes

κ of stress-free single-walled CNTs (SWCNTs) increases with tube length (l) until it reaches the phonon mean free path (l_{MFP})[33,180,194,199,201]. In this work, we are concerned with SWCNTs with lengths under 1 μm, which cover both ballistic and diffusive regimes. We applied non-equilibrium molecular dynamics (NEMD)[123] to study thermal conductivities along SWCNTs with different lengths and chirality. A thorough comparison of phonon relaxation time, phonon group velocity, phonon dispersion curves and phonon density of states (PDOS) between cylindrical and flattened SWCNTs are conducted to provide understanding of their differences in κ. In addition, a deep analysis of the three most commonly used potentials in molecular dynamics calculations of carbon-based materials is presented.

Our large-scale atomistic molecular dynamics simulations are performed with LAMMPS[140]. Three different interatomic potentials are used to study the structures: the adaptive intermolecular reactive empirical bond order (AIREBO) potential[198], which includes a Lennard-Jones term (LJ) describing the van der Waals interactions

experienced by the C-C atoms located in the 2-10.2 Å space interval, and is expressed as

$$V_{ij}^{LJ} = 4\varepsilon \left[\left(\frac{\sigma}{r_{ij}} \right)^{12} - \left(\frac{\sigma}{r_{ij}} \right)^{6} \right]$$
(4-5)

where the energy parameter $\varepsilon = 0.00284 eV$ and the distance parameter $\sigma = 3.4$ Å; a combination of the second-generation reactive empirical bond order (REBO-II) potential[202] and the LJ potential; and a combination of optimized Tersoff (Tersoff-2010) potential[203] and the LJ potential, which describes the interlayer interaction of the grey and the red layers shown in the Tersoff model in Figure 32 (a). The connection of the two layers (the purple parts) is described with Tersoff-2010 only to avoid the strong repulsion of LJ potential. To be consistent, the parameters and cut-off distances in the LJ terms in all the above three potentials are the same. We use REBO+LJ and Tersoff+LJ to refer to the latter two potentials. The original Tersoff potential[204] is also widely used to study C-C interactions. However, due to its intrinsic drawback in describing the bending behavior[205] and the lattice dynamics of graphene[203,206], we will not discuss its application in this work. The optimized Tersoff-2010 is developed by adjusting the attraction term in the original Tersoff potential, which displays a significant improvement in both obtaining the κ values of graphene and fitting the dispersion curves of all acoustic phonon branches in graphene[203,206].

To study the behavior of CNTs with large diameters at room temperature, a series of (30, 30) armchair, (50, 0) zigzag and (20, 50) chiral cylindrical and flattened SWCNTs, which respectively have dimeters of 4.1nm, 3.9nm and 4.9nm in their cylindrical form, are investigated. Initially, a Nose-Hoover thermostat is used to equilibrate the cylindrical SWCNTs at 300K. After the system reaches equilibrium, a $0.01 eV/\text{Å}$ force is added in transverse direction for 200 ps to squeeze the structure. The system is then freed in transverse direction and is equilibrated again under microcanonical ensemble for another 200 ps. Periodic boundary conditions are applied in the axial direction during the whole process. The van der Waals attraction of the closest walls (region 1) overcomes the stress at the circular edges (region 2) due to the C-C covalent bonding, resulting in a stabilized flattened SWCNT shown in Figure 32 (a). The width of the flattened SWCNTs in the transverse direction (y direction shown in Figure 32 (c)) with a certain chirality remains the same modeled with the same potential. For example, for zigzag SWCNTs modeled with AIERBO, the width in the transverse direction remains to be 7.17 Å when the diameter of the cylindrical tube is $>\sim$ 2.5 nm. It's worth noting that after a brief transverse compression, although the cross-sectional view of the relaxed flattened CNTs described with different potentials all present dumbbell-like shapes, the areas of region 1 are different. The area of region 1 depends on the bending stiffness of the monolayer graphene sheet. The stiffer the graphene sheet that comprises the SWCNT, the more difficult it is for the vdW attractions to hold walls together. The

bending moduli of monolayer graphene under infinitesimal bending curvature[207] are 0.91eV, 1.41eV and 2.29eV, calculated with AIREBO, REBO-II and Tersoff-2010 potentials, respectively. It can be seen that the bending modulus calculated with REBO-II is the closest to that calculated with *ab-initio*[205], which gives 1.46eV. The reason AIREBO gives the lowest bending modulus is because, compared to REBO-II, AIERBO adds an additional "torsional term" to describe the rotation about a single C-C sp^3 bond[198], which is much softer than the C-C sp^2 in benzene-ring structures like graphene and CNTs. Therefore, the conformation described with REBO+LJ in Figure 32 (a) is the most accurate among all the three proposed shapes. The bending stiffness also affects the atomic vibration in the out-of-plane mode, which determines the out-of-plane optical phonon mode, the ZO mode, in graphene. A "softer" graphene sheet described with AIREBO makes the ZO mode in graphene blue-shifted. On the contrary, a "stiffer" graphene sheet described with Tersoff-2010 overestimates the frequencies of ZO mode in graphene. REBO-II gives the best description of the ZO mode. A detailed comparison can be obtained in Ref[206]. The shift of the ZO mode in the phonon dispersion relation may affect the acoustic-optical phonon scattering mechanism, resulting in a different thermal conductivity. For example, the underestimation of the frequency of the ZO mode in graphene described with AIREBO interferes the propagation of the acoustic phonons, which produces a lower thermal conductivity compared with that calculated with Tersoff-2010. Hence, even though ZO mode is not

the main contributor to thermal transport, it is important in influencing the phonon scattering mechanisms, which, in turn, determines the magnitude of κ.

The proposed NEMD simulation for a (30,30) SWCNT set-up is shown in Figure 32 (b) and (c). One unit cell at each end is fixed to prevent the center of the mass of the system from moving. Four other unit cells next to the fixed cells are set as hot and cold reservoirs. The time step throughout all the simulations is 0.5 fs. The system is initially equilibrated at 300K with a Nose-Hoover thermostat. Then the two reservoirs are rescaled at every time step to maintain $T_h = 310K$ and $T_c = 290K$, respectively. The velocity Verlet algorithm is used for time integration. A steady state is reached after 1000 ps for $l \leq 120nm$ and 3000 ps for $l > 120nm$. The heat fluxes along the SWCNTs are obtained by calculating the differences of the rates of the kinetic energy extraction from the two reservoirs:

$$\dot{Q} = \frac{1}{2} < \dot{Q}_h - \dot{Q}_c > \tag{4-6}$$

where $\dot{Q}_h$ and $\dot{Q}_c$ are the instantaneous heat currents flowing into and away from the hot and cold reservoirs to maintain the temperature gradient. The angular brackets indicate a statistical average taken over the last 500 ps for $l \leq 120nm$ and 1000 ps for $l > 120nm$ after steady state is reached. κ is calculated with the Fourier's Law:

$$\kappa = -\dot{q} \left(\frac{dT}{dz}\right)^{-1} \tag{4-7}$$

(a)

↓↓↓↓↓ Force

Region 2   Region 1
AIREBO model

Region 2   Region 1
REBO+LJ model

Region 2   Region 1
Tersoff+LJ model

↑↑↑↑↑ Force

(b)

(30, 30)   (50, 0)

(c)

y
x
z Hot Reservoir   Heat Flux   Cold Reservoir
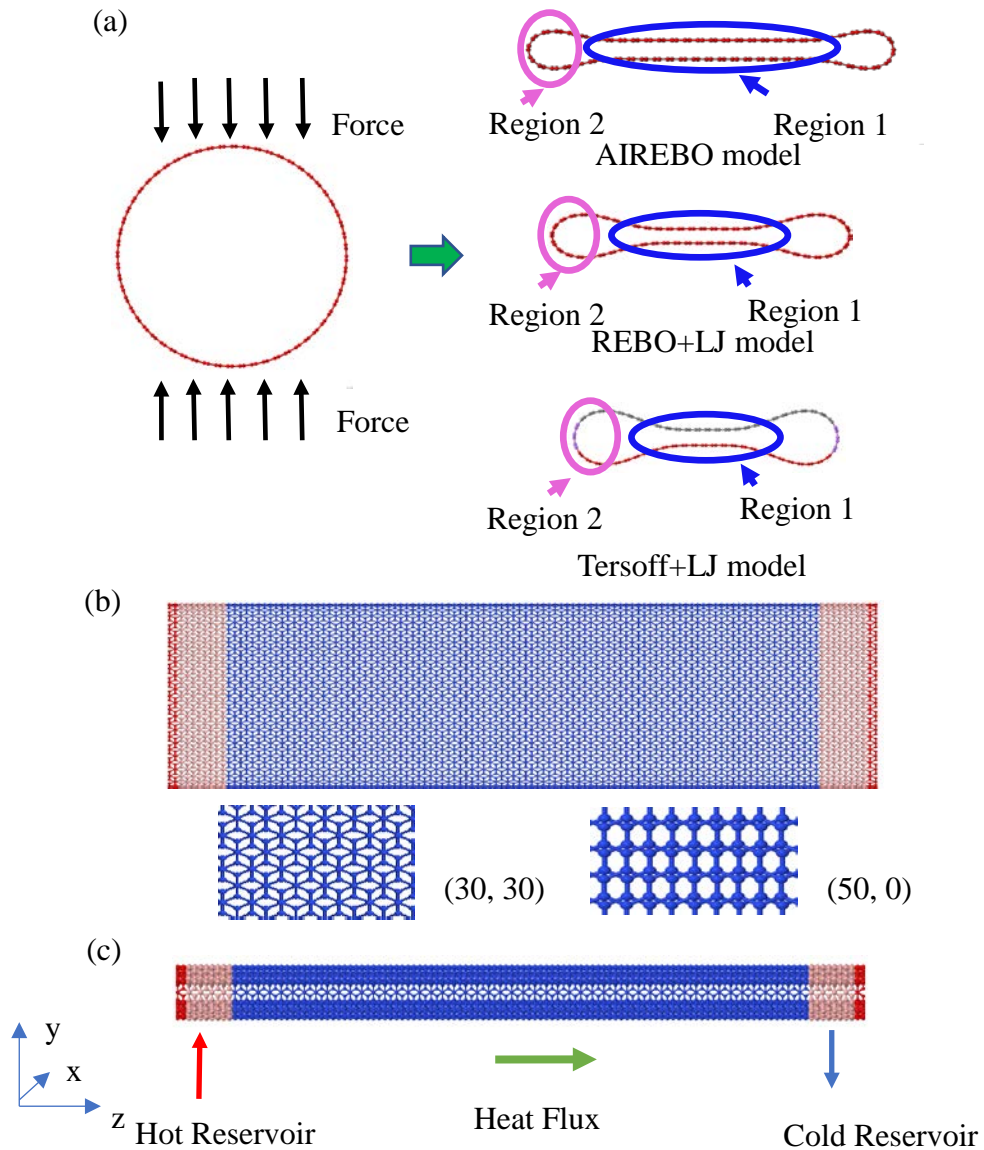
Figure 32. (a) The formation of flattened SWNCTs and the view along axial direction (z direction) in the flattened SWCNTs. (b) and (c) show the transverse view (along y and x directions) of the flattened SWCNTs. The difference in the transverse view of flattened (30, 30) and (50, 0) SWCNTs in y direction is shown in (b).
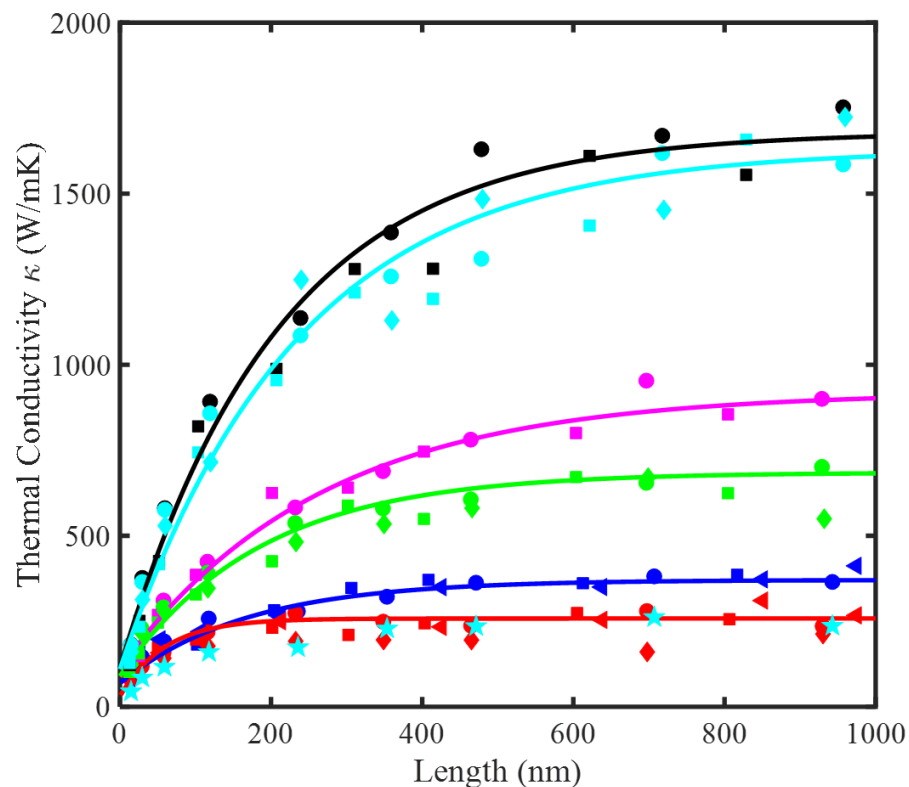
Figure 33. Thermal conductivity of cylindrical (blue, magenta, and black symbols) and flattened (red, green and cyan symbols) CNTs with different tube lengths calculated with AIREBO (blue and red), REBO+LJ (magenta and green), and Tersoff+LJ (black and cyan). The circles, squares, triangles and diamonds represent the thermal conductivity of (30, 30), (50, 0) and (20, 50) CNTs, and zigzag bilayer graphene nanoribbons. The bilayer graphene nanoribbons with rough surface simulated with Tersoff+LJ potential is represented with cyan pentagons. Fitted curves are represented by solid lines.

where $\dot{q}$ is the heat flux per unit cross-sectional area, which is defined by the thickness of one-atom-layer tube wall, 0.34 nm, multiplied by the circumference of one ring of the SWCNT in the cross-section view. z is the axial position. T is the local temperature obtained by statistically averaging the kinetic energy of the atoms located on two subsequent unit cells.

Our main results are summarized in Figure 33, which shows a noticeable κ reduction for long, flattened SWCNTs compared to cylindrical ones, as calculated with AIREBO, REBO+LJ, and Tersoff+LJ, which display $\sim$ 30 %, $\sim$ 26 %, and $\sim$ 3 % κ reductions. The amount of reduction of κ depends on the degree of deformation of the cross-section, i.e. the larger area that region 1 has, and the more strain in region 2, the more significant in the κ can be lowered. We speculate the lowering of κ may be due to the van der Waals interaction in region 1, which allows phonon-phonon scattering in the out-of-plane transverse direction. In addition, the large strain in region 2 may also hinder the movement of atoms in the transverse and shear directions, thus diminishing the ability to transport heat in the axial direction. We can also see that the Tersoff+LJ model gives the highest κ value, which is the closest value to the experimental measurements[32].

To further understand the scattering mechanism, phonon relaxation time (τ_z) for acoustic phonon modes is investigated, which reflects the average time between

successive phonon scattering events in each phonon branch. In pristine SWCNTs, there are four acoustic modes[208]: two degenerate translational acoustic (TA) modes, corresponding to atomic movement perpendicular to the axial direction, which include the out-of-plane mode similar to the flexure mode (ZA mode) in graphene; a twist mode (TW), corresponding the torsional movement of atoms around the axis, which can be analogous to the in-plane mode in graphene; and a longitudinal mode (LA), corresponding to the atomic movement along the axial direction. τ_Z is evaluated with the spectral energy density[209],

$$
\Phi(q_z, \omega) = \frac{1}{4\pi\tau_0 N_T} \sum_\alpha \sum_b^B m \left| \int_0^{\tau_0} \sum_l^{N_T} v_\alpha \begin{pmatrix} l \\ b \end{pmatrix}; t \right.
$$
$$
\left. \cdot \exp\left[ik_z z \begin{pmatrix} l \\ 0 \end{pmatrix} - i\omega t\right] dt \right|^2
\tag{4-8}
$$

where k_z is the z component of the wave vector, ω is the angular frequency, and τ_0 is the integration time constant, here we use $\tau_0 = 250$ ps. Index α represents x, y and z directions. $v_\alpha \begin{pmatrix} l \\ b \end{pmatrix}; t$ is the α component of the instantaneous velocity of atom b with mass m inside unit cell l. B is the number of atoms in a unit cell. N_T is the number of unit cells in the simulation domain, here we have $N_T = 50$. The shape of the frequency spread for each mode can be fitted with the Lorentzian function

$$
\Phi(q_z, \omega) = \frac{I}{1 + [(\omega - \omega_c)/\gamma]^2}
\tag{4-9}
$$

where I is the peak magnitude, ω_c is the frequency at the peak center, and γ is the half-width at half-maximum. τ_Z is defined by $\tau_Z = 1/2\gamma$. The local τ_Z of cylindrical and flattened armchair SWCNTs are investigated to illustrate the difference in κ, see Figure 35. The average τ_Z for each phonon mode calculated with different potentials are summarized in Table 4-2.

Table 4-2. Comparison of average τ_Z for each phonon mode in cylindrical and flattened SWCNTs.

Potential	Chirality	Morphology	Region	TA (ps)	TW (ps)	LA (ps)
AIREBO	(30, 30)	Cylindrical		1.353	0.465	0.452
		Flattened	1	1.230 (-9.1%)	0.556 (+19.6%)	0.418 (-7.5%)
			2	0.507 (-62.5%)	0.374 (-19.9%)	
			Average	0.869 (-35.8%)	0.465 (0.0%)	
	(50, 0)	Cylindrical		1.938	0.504	0.349
		Flattened	1	1.471 (-24.1%)	0.550 (+9.1%)	0.319 (-8.6%)
			2	0.836 (-56.9%)	0.414 (-17.9%)	
			Average	1.154 (-40.5%)	0.482 (-4.4%)	
REBO+ LJ	(30, 30)	Cylindrical		1.521	0.563	0.416
		Flattened	1	1.116 (-26.6%)	0.606 (+7.6%)	0.413 (-0.7%)
			2	0.673 (-55.8%)	0.463 (-17.8%)	
			Average	0.895 (-41.2%)	0.534 (-5.3%)	
	(50, 0)	Cylindrical		2.484	0.574	0.325
		Flattened	1	1.357 (-45.4%)	0.683 (+19.0%)	0.324 (-0.3%)
			2	1.340	0.572	

				(-46.1%)	(-0.4%)	
			Average	1.349 (-45.7%)	0.628 (+9.4%)	
	(30, 30)	Cylindrical		1.251	0.485	0.458
		Flattened	1	1.221 (-2.4%)	0.566 (+16.7%)	0.421 (-8.1%)
			2	0.641 (-48.8%)	0.455 (-6.2%)	
			Average	0.931 (-25.6%)	0.510 (+5.5%)	
Tersoff+ LJ	(50, 0)	Cylindrical		1.911	0.529	0.309
		Flattened	1	1.403 (-26.6%)	0.610 (+15.3%)	0.306 (-1.0%)
			2	1.276 (-33.2%)	0.502 (-5.1%)	
			Average	1.340 (-29.9%)	0.556 (+5.1%)	

Note: the percentage in the parenthesis denotes the change in τ_Z, compared to those of cylindrical structures.

From Table 4-2 we can see that for flattened SWCNTs, τ_Z of the TA modes in region 2 is the most significantly reduced phonon modes in all the structures simulated with all the three potentials. This means that the large strain due to the severe bending in region 2 is the main reason for the reduction in TA phonon transport. It is also obvious that the reduction rates of τ_Z of TA and TW modes in region 2 are more significant in the armchair SWCNT than that in the zigzag SWCNT, within the same potential model. For example, modeled with REBO+LJ potential, the reduction of τ_Z of TA modes in region 2 in the (30, 30) SWCNT is 55.8 %, compared to that in the (50, 0) SWCNT, which is 46.1 %. This is because of the difference in bending energy in graphene under large bending curvature[207]. Even though the tangential bending moduli along the zigzag and armchair directions are the same under infinitesimal bending

curvature, as bending curvature increases, the monolayer graphene becomes anisotropic and presents different bending moduli along zigzag and armchair directions. Under the same bending curvature, the strain energy of monolayer graphene is higher for bending along the zigzag direction, which corresponds to the larger strain in region 2 in the armchair SWCNT. Hence TA and TW phonons in region 2 are scattered more significantly in flattened (30, 30) SWCNTs than those in flattened (50, 0) SWCNTs. The TA modes in region 1 for all flattened structures modeled with all potentials also decrease. Region 1 in a flattened SWCNT can be compared to a bi-layer graphene nanoribbon with a 3.36 Å spacing, see Figure 34 (a). The thermal conductivity of a bi-layer graphene in the in-plane direction is lower than that of a single-layer graphene due to phonon scattering in the inter-plane direction[210–213], especially ZA phonon scattering[214], which is comparable to our TA mode scattering in region 1 in flattened SWCNTs. It is also noticeable that the τ_Z reduction rate of τ_Z of TA mode in region 1 is more significant in the flattened (50, 0) SWCNT than that in the flattened (30, 30) SWCNT. For flattened (30, 30) SWCNTs, region 1 viewed from the y direction resembles the interplane direction of a AB stacking bilayer graphene which has a 50% mismatch, see Figure 32 (b), bottom left. While for flattened (50, 0) SWCNTs, region 1 is neither AA stacking nor AB stacking, which has 100% mismatch, see Figure 32 (b), bottom right. The fewer atoms overlapping, the more phonon mismatch there will

106
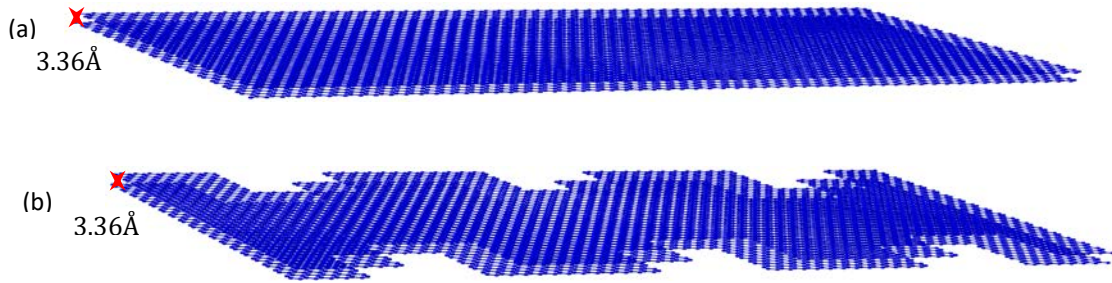
Figure 34. Bi-layer graphene (a) without and (b) with rough edges.

be, which causes phonon scattering in the cross-plane direction, i.e. TA phonon scattering. Thus, more TA phonons in (50, 0) SWCNTs are scattered in region 1. Considering both effects, the average TA phonon scattering rate for the whole structure is the same for (30, 30) and (50, 0) SWCNTs. τ_Z of TW in region 1 in all flattened structures are either close to or higher than those of the cylindrical SWCNTs. This is because unlike in cylindrical SWCNTs, region 1 in flattened SWCNTs is almost flat and has little tension due to bending. The less strain there is, the easier the phonons can be transported[215]. However, the overall effect of flattening does not alter many of the TW modes (the change of τ_Z is within 10%). Similarly, due to the strain effect in region 2 in flattened SWCNTs, τ_Z of the LA modes is also decreased, but also within 10%. Hence, τ_Z is most significantly lowered in the TA branch in flattened SWCNTs. The average TA scattering rate calculated with Tersoff+LJ is less than that calculated with the other two models. This is because the flattened SWCNTs with Tersoff+LJ model is the least severely flattened and the strain in region 2 is the smallest due to the large bending modulus of graphene with this potential.

Another important factor determining κ is the phonon group velocity along the axial direction, $v_{g,z}$. In order to calculate $v_{g,z}$, lattice dynamics calculations[216] are conducted, which can also provide solutions to analyze the phonon dispersion relation. The core equation for lattice dynamical calculations is

$$\widehat{\boldsymbol{D}}(k_z)\boldsymbol{\xi} = m\omega^2\boldsymbol{\xi} \tag{4-10}$$

Where $\widehat{\boldsymbol{D}}(k_z)$ is the dynamical matrix, which can be obtained from

$$\widehat{\boldsymbol{D}}(k_z) = \sum_{R} \boldsymbol{D}(\boldsymbol{R})e^{ik_z\cdot\boldsymbol{R}} \tag{4-11}$$

Where $\boldsymbol{R}$ represents equilibrium lattice sites of a unit cell, $\boldsymbol{D}(\boldsymbol{R})$ is the force constant matrix, $\widehat{\boldsymbol{D}}(k_z)$ is Hermitian for real valued wave numbers k_z, ω is the phonon frequency for each k_z. Solutions of ω for armchair and zigzag cylindrical and flattened SWCNTs with different potential models are shown in Figure 36 and Figure 37. Due to the flattening effect, the TA mode in the flattened SWCNTs at $k_z \rightarrow 0$ has a $\omega \propto k_z^2$ relation, resembling that of the flexure mode in graphene; while TAs mode in the cylindrical SWCNT remains the typical $\omega \propto k_z$ relation at $k_z \rightarrow 0$. The breakdown of symmetry about z-axis and the strain effect also produce fewer degenerate solutions, allowing for more optical-acoustic phonon scattering channels. Different potentials cause the difference in phonon frequencies of the out-of-plane optical mode, i.e. the TO mode, which resembles the ZO mode in graphene. As discussed before, although this

mode is not the main factor of heat transport, it has influence on the acoustic-phonon scattering effects. As can be seen, in the Tersoff-LJ model, the TO mode has a much higher frequency than that in the other two models, thus providing less acoustic-acoustic-optical phonon scattering channels, resulting in a higher thermal conductivity, see Figure 33.

Based on Equation (4-11), we further calculate $v_{g,z}$, which is expressed as

$$v_{g,z} = \frac{d\omega}{dk_z} = -\frac{\text{Im}[a\lambda\boldsymbol{\xi}^H \widehat{\boldsymbol{D}}_R \boldsymbol{\xi}]}{2m\omega|\boldsymbol{\xi}|^2} \tag{4-12}$$

Where $\lambda = e^{i\frac{k_z a}{2}}$, a is the length of the unit cell in z direction, the superscript H denotes a complex-conjugate transpose, $\widehat{\boldsymbol{D}}_R$ is the dynamical matrix of the neighboring unit cells. The calculated results for (30, 30) SWCNTs are shown in Figure 38. The average $v_{g,z}$ for the cylindrical and flattened SWCNTs are 838.86 m/s and 782.39 m/s calculated with AIREBO, 883.06 m/s and 855.42 m/s with REBO+LJ, 882.65 m/s and 868.95 m/s with Tersoff+LJ, respectively. Although a slight decrease in $v_{g,z}$ is observed in the flattened SWCNT, the main values and the distribution of $v_{g,z}$ over all the frequencies remain the same. Hence, the structural difference has little effect on $v_{g,z}$. The scattering effect is the main reason for κ reduction in the flattened SWCNT.

To gain more insight into the microscopic mechanism of how the strain effects in the flattened SWCNT affect the phonon modes at different frequencies, PDOS are

obtained by decomposing into the Fourier space the MD time-correlation function of the atomic velocities at 300 K. For cylindrical SWNCTs, we calculate the PDOS of the whole structure. For flattened SWCNTs, we calculated the local PDOS of region 1 and region 2 separately to observe the different effect on phonons due to different structures. The calculated results are shown in Figure 39. As we can see, major phonon peaks in region 2 in the flattened SWCNTs are slightly lowered compared to region 1 and those in cylindrical SWCNTs. Additionally, more optical phonons emerge in the high frequency range (55~60 THz for AIREBO and REBO+LJ models, and 50~55 THz for Tersoff+LJ models) in the flattened SWCNT, which is an indication of the severe strain in region 2. Overall, the change in PDOS can be neglected.

To understand the mechanism of phonon scattering, we used Non-equilibrium Green's function to calculate thermal conductance[217,218] G of SWNCTs with harmonic approximation,

$$G(T) = \frac{\hbar^2 \omega^2}{2\pi k_B T^2} \int \tau(\omega) \frac{e^{\hbar\omega/k_B T}}{(e^{\hbar\omega/k_B T} - 1)^2} d\omega \tag{4-13}$$

where $\hbar$ is the Planck constant, k_B is the Boltzmann constant and $\tau(\omega)$ is the phonon transmission. The results calculated with QuantumWise package[219] for (30, 30) SWCNTs with REBO+LJ potential is shown in Figure 40. As we can see, there is very
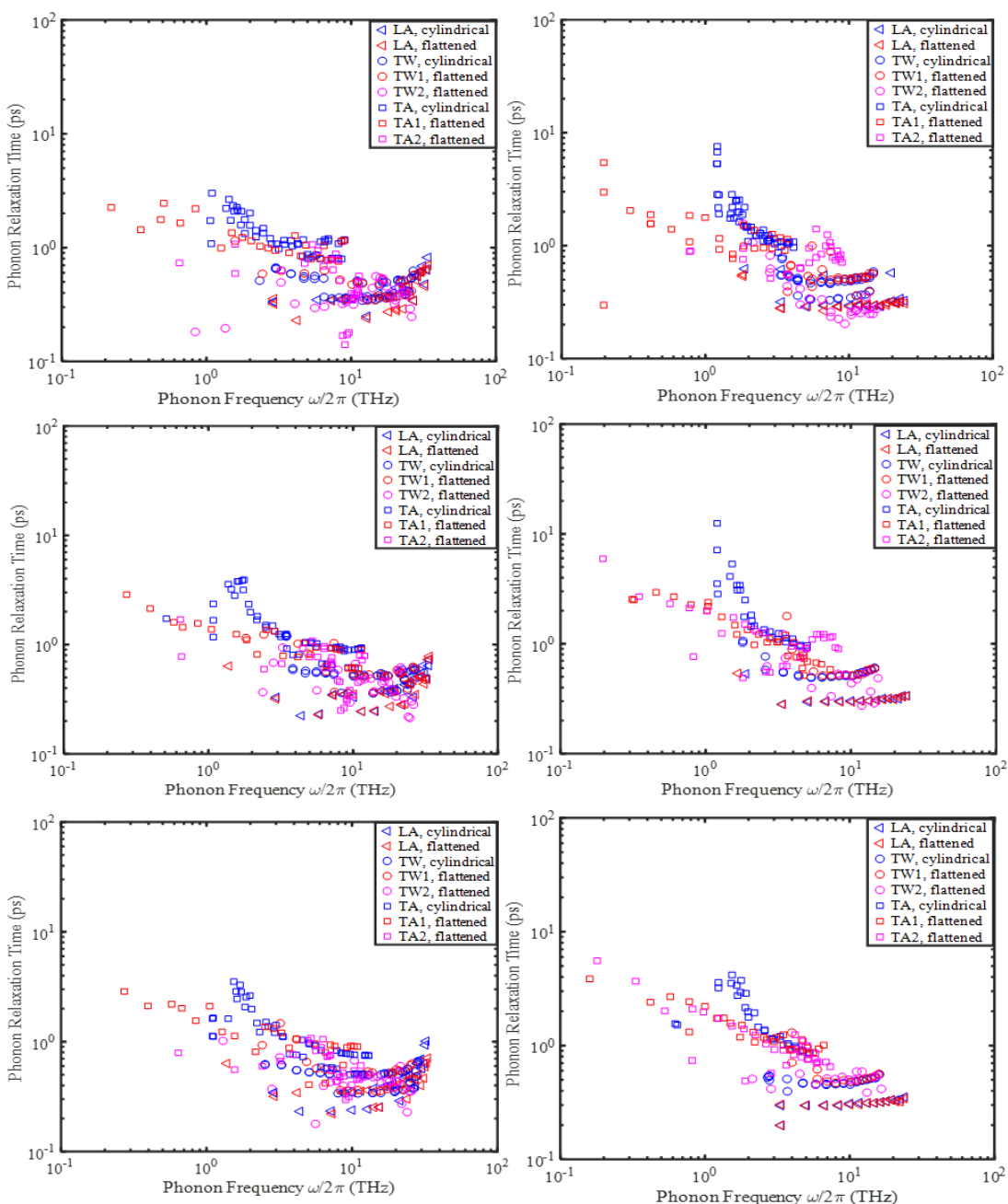
Figure 35. Phonon relaxation time for different phonon modes. The top, middle and bottom figures represent phonon relaxation time calculated with AIREBO, REBO+LJ and Tersoff+LJ, respectively. The left and right figures represent (30, 30) and (50, 0) SWCNTs, respectively. TW1 and TA1 represent the twist modes and transverse acoustic modes in region 1, respectively. Similarly, TW2 and TA2 denote the twist modes and transverse acoustic modes in region 2, respectively.
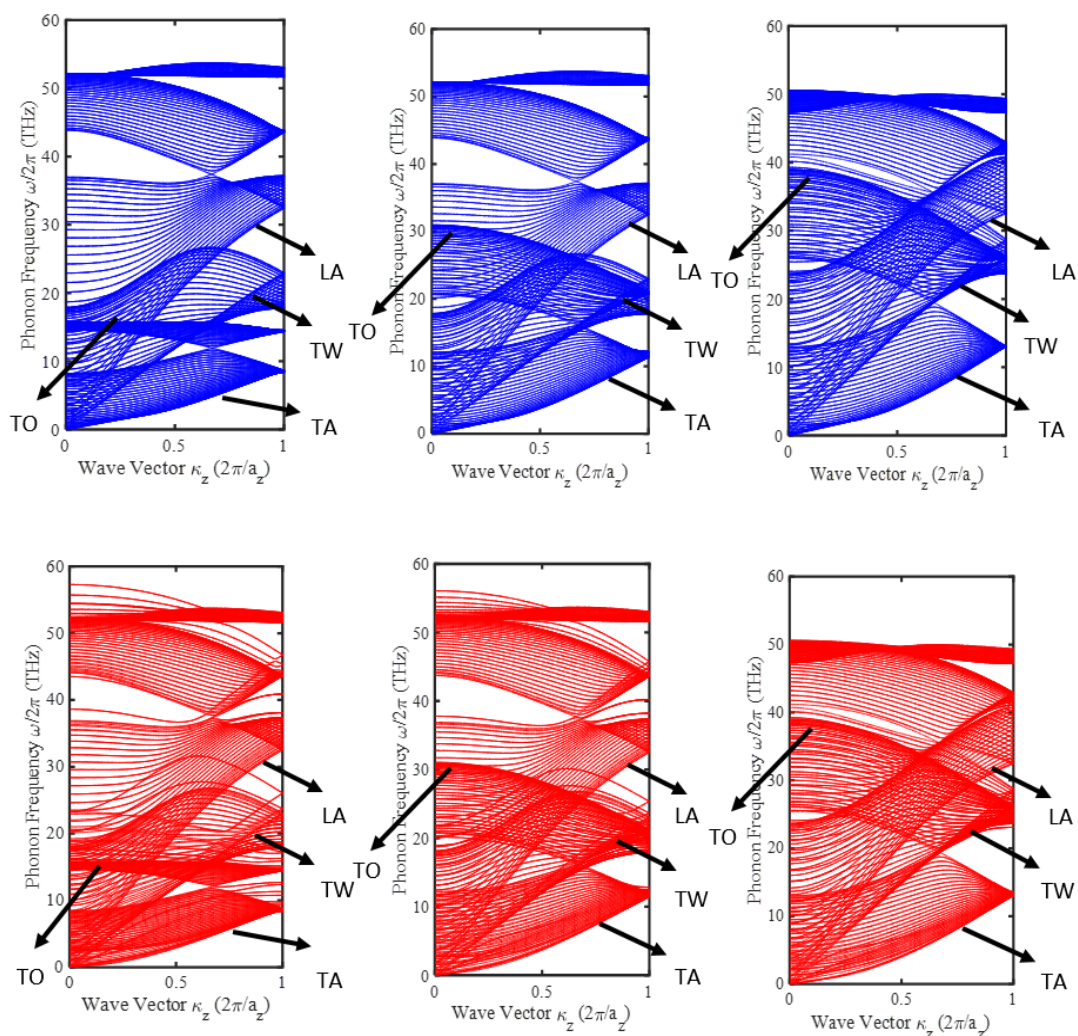
Figure 36. Phonon dispersion relations of cylindrical (upper, blue) and flattened (lower, red) (30, 30) SWCNTs calculated with AIREBO (left), REBO+LJ (middle) and Tersoff+LJ (right). The black arrows denote the acoustic phonon branches (TA, TW and LA) and the out-of-plane optical phonon branch (TO) which are most important in determining the thermal conductivity of the studied SWCNTs.
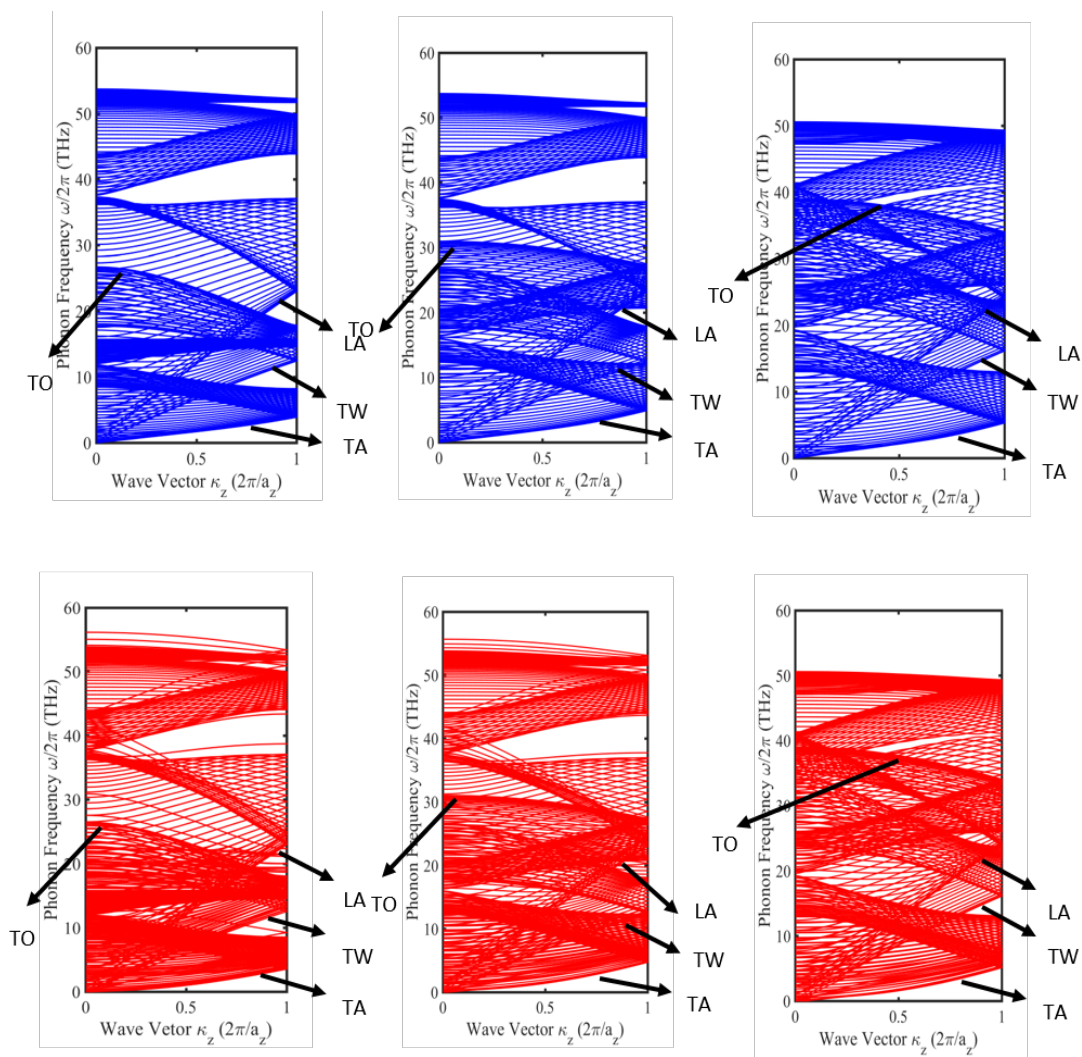
Figure 37. Phonon dispersion relations of cylindrical (upper, blue) and flattened (lower, red) (50, 0) SWCNTs calculated with AIREBO (left), REBO+LJ (middle) and Tersoff+LJ (right). The black arrows denote the acoustic phonon branches (TA, TW and LA) and the out-of-plane optical phonon branch (TO) which are most important in determining the thermal conductivity of the studied SWCNTs.
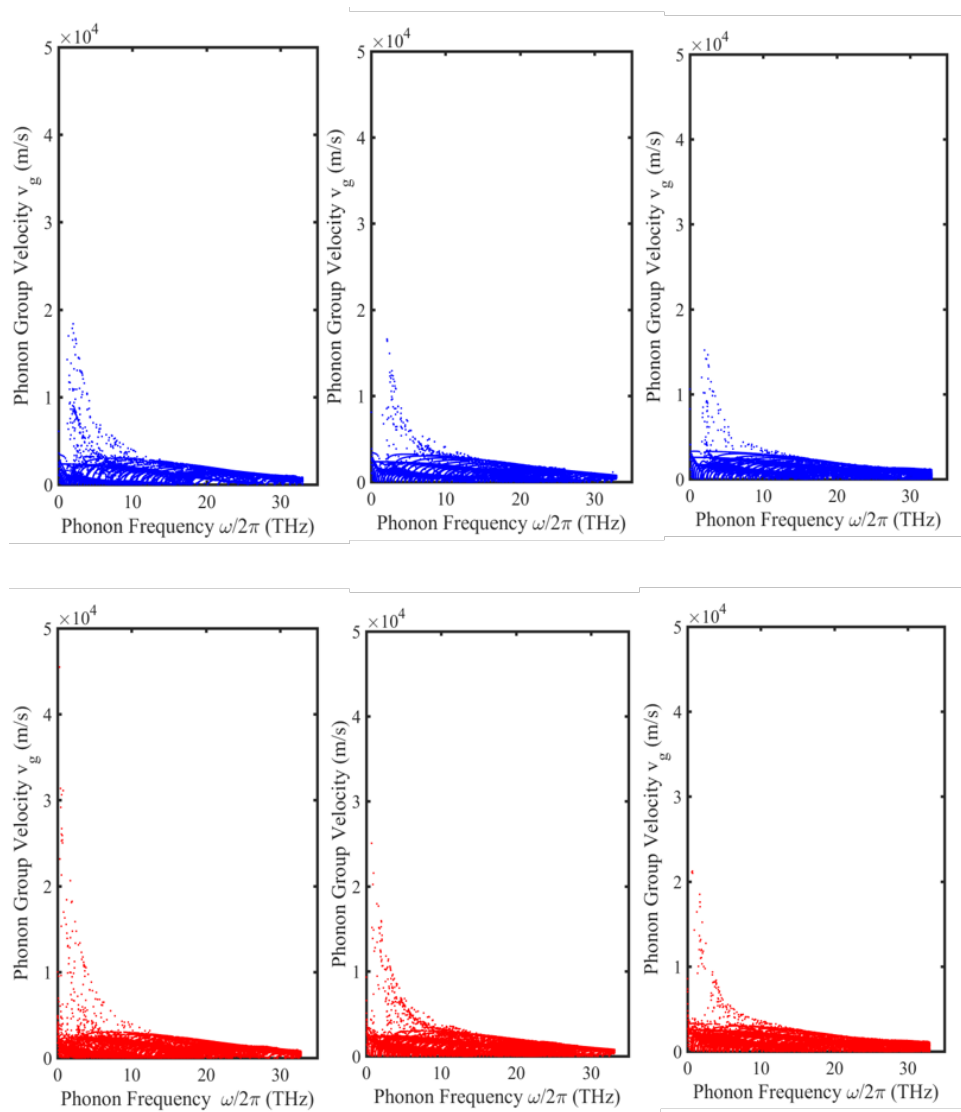
Figure 38. Acoustic phonon group velocities of cylindrical (upper, blue) and flattened (lower, red) (30, 30) SWCNTs calculated with AIREBO (left), REBO+LJ (middle) and Tersoff+LJ (right).
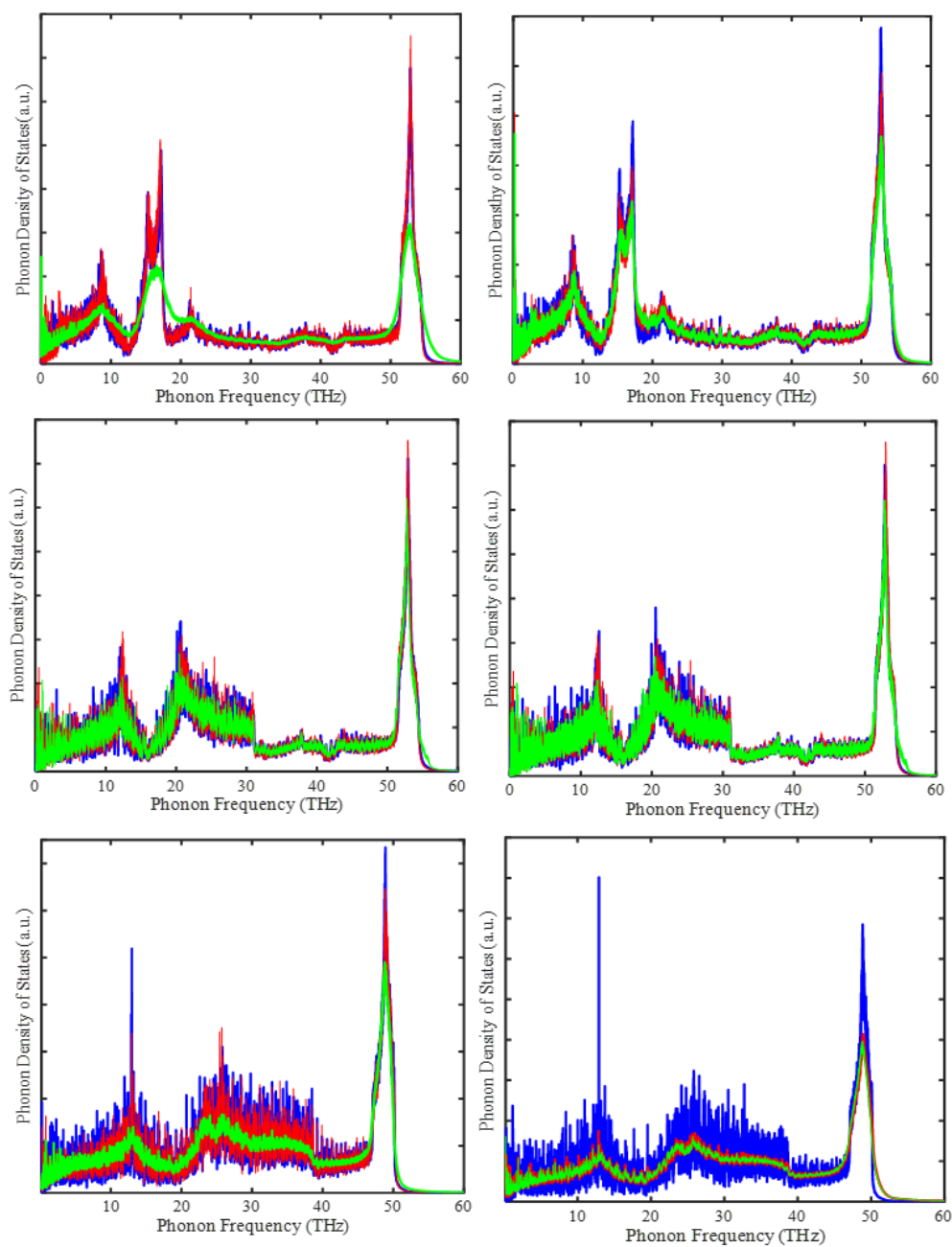
Figure 39. Phonon density of states of (30, 30) (left) and (50, 0) (right) SWCNTs calculated with AIREBO (top), REBO+LJ (middle) and Tersoff+LJ (bottom) potentials. The cylindrical SWCNTs are represented with blue curves. Region 1 and 2 in flattened SWCNTs are represented in red and green curves, respectively.

little difference in G calculated with harmonic approximation in cylindrical and flattened SWCNTs. Therefore, the reduction in thermal conductivity of the flattened SWCNT calculated with REBO+LJ lies in the anharmonic phonon-phonon scattering.
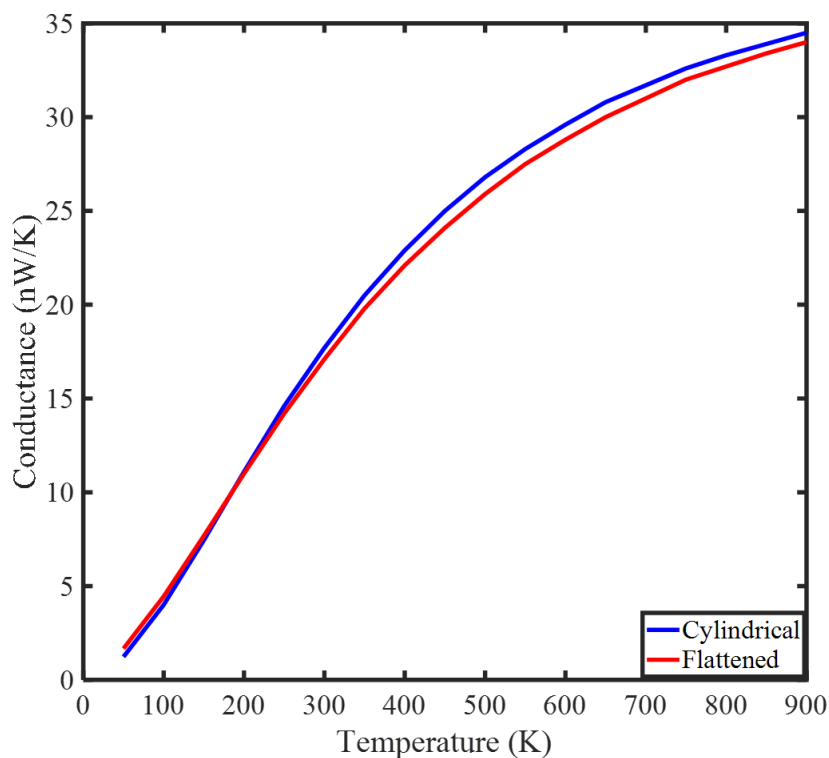
Figure 40. Thermal conductance of (30, 30) SWCNTs with REBO potential. The thermal conductance of cylindrical and flattened SWCNTs are shown in blue and red curves.

As we mentioned before, the shapes of flattened SWCNTs resemble that of a bi-layer graphene nanoribbon. Here we also studied the thermal transport along a bare-edged zigzag graphene nanoribbon with the same number of atoms per unit length as that of the (30, 30) SWCNT, Figure 34 (a). The κ values of different lengths calculated with different potentials are represented with diamonds in Figure 33. It can be seen that

κ of the flattened SWCNTs are very close to that of the bi-layer graphene nanoribbon. The flattened surface of region 1 in the flattened SWCNTs resembles that of a bi-layer graphene nanoribbon surface. In addition, the large strain in region 2 of the flattened SWCNTs has an equivalent effect in scattering phonons as the bared-edges of the bi-layer graphene nanoribbons. To support this hypothesis, we make the edges of the bi-layer graphene rougher by removing and adding atoms on the edges while keeping the total number of atoms the same, Figure 34 (b). The κ values calculated with Tersoff+LJ are shown as cyan pentagons in Figure 33. As some phonons are easily trapped in the rough edges, κ is significantly reduced compared to the model shown in Figure 34 (a). A similar discussion can be found in Ref[115]. This indicates that the flattened SWCNTs, or close-edged bi-layer graphene, can be a good candidate to replace bi-layer graphene nanoribbons for thermal transport applications. Compared to cylindrical SWCNTs, flattened SWCNTs are also susceptive to twists, similar to graphene nanoribbons[220]. We have investigated κ in twisted flattened SWNCTs (Figure 41) with different twist angles (0 ~ 5.5 deg/nm) with Tersoff+LJ and found no significant change in κ, which shows the robustness of the flattened SWCNTs in conducting heat.

Figure 41. A twisted flattened (30, 30) SWCNT.

4.4 Conclusion

I studied the effect of pure bending strain and the flattening effect on the thermal transport of SWCNT with different sizes. NEMD simulations reveal that the kink developed under bending exhibits a much larger resistance-related effective length than previously suggested. In the short-l regime, the overall κ exhibits a sizable decrease by the time buckling occurs. The κ reduction is most significant in small-diameter SWCNTs, which display a higher critical curvature for buckling. The flattening effect has a very minor impact on thermal transport along SWCNTs. The finding is important since significant tunability of the thermal conductivity characteristic for the $l \ll l_{MFP}$ regime is interesting for applications. As $l \sim l_{MFP}$, thermal conductivity becomes robust as the heat-carrying long-wavelength phonons become insensitive to the localized buckling deformation. SWCNTs with large diameters also have important applications in mechanical and thermal applications. Understanding their thermal behavior when they are flattened is crucial in guiding their applications.

Chapter 5

Conclusion

In this work, heat transfer in solids is studied with modern computational methods, which explicitly simulate microscopic heat carriers, or phonons. Atomistic simulations, particularly molecular dynamics techniques, allow us to generate a large amount of data documenting how atoms vibrate around defects or under mechanical deformation. By processing these data with statistical physics methods, I am able to relate the motion of hundreds of thousands of atoms to measurable thermal properties of the structure.

One limitation of MD is the relatively small (on the order of hundreds of thousands) number of atoms that can be simulated. Fortunately, it is not necessary to do calculations on every single atom of the solid, as boundary conditions of the simulated cell have the advantage of significantly simplifying the underlying calculations. Periodic boundary conditions offer a simplified approach to simulating structures with only translational symmetry, such as a bulk crystal or a straight pristine nanowire. In this thesis, I consider structures that have not only translational symmetry,

but also rotational and/or helical symmetry. Examples of such structures are NWs with screw dislocations (Chapter 2), purely bent carbon nanotubes (Chapter 4), and twisted flattened carbon nanotubes (Chapter 4). For these structures, standard molecular dynamics under periodic boundary conditions cannot be used. Instead, I performed these calculations with a novel method named objective molecular dynamics. This method exploits the aforementioned boundary conditions to match the helical/rotational symmetry of the structures at hand in order to make the simulations computationally affordable.

The knowledge gained in this research has important implications for renewable energy and thermal management in electronics. The finding in Chapter 2, which shows that dislocations can lower thermal conductivity significantly, presents enormous importance for the development of new thermoelectric materials with very high heat-electricity conversion efficiency, and has already attracted interest in experimental studies. The thorough study of thermal and mechanical properties of a high-temperature coating composite, namely the amorphous Silicon-Boron-Nitride networks discussed in Chapter 3, provides practical guidance in designing high-performance coatings. The investigation method in this study also promises broad applicability to other composition-structure-properties relationships in more complex composite materials. The study of carbon nanotubes and bi-layer graphene presented in Chapter 4 shows the effect of mechanical deformation in tube-like structures on heat transport through

carbon nanotubes, which has implications for applications of CNTs in thermal interface materials. At the same time, the discoveries in this work also resolve some conflicts between experimental measurements and numerical simulations, as the results shown in this thesis are in agreement with similar experimental discoveries. The studies in this thesis also provide important routes to developing high-performance functional materials. It is likely that these nano-scale heat transfer studies will soon move from computation to experiments, and further industrial applications.

References

1. Kaviany, M. *Heat transfer physics*. (Cambridge University Press, 2014).

2. Peierls, R. Zur kinetischen theorie der wärmeleitung in kristallen. *Ann. Phys.* **395,** 1055–1101 (1929).

3. Carslaw, H. S. & Jaeger, J. C. Conduction of heat in solids. *Oxf. Clarendon Press 1959 2nd Ed* (1959).

4. Klemens, P. Thermal conductivity of solids at low temperatures. *Handb. Phys.* **3,** 198–281 (1956).

5. Vineis, C. J., Shakouri, A., Majumdar, A. & Kanatzidis, M. G. Nanostructured thermoelectrics: big efficiency gains from small features. *Adv. Mater.* **22,** 3970–3980 (2010).

6. Greicius, T. Mars Science Laboratory - Curiosity. *NASA* (2015). Available at: http://www.nasa.gov/mission_pages/msl/index.html. (Accessed: 29th March 2017)

7. Tritt, T. M. Thermoelectric phenomena, materials, and applications. *Annu. Rev. Mater. Res.* **41,** 433–448 (2011).

8. Boukai, A. I. *et al.* Silicon nanowires as efficient thermoelectric materials. *Nature* **451,** 168–171 (2008).

9. He, Y. & Galli, G. Microscopic origin of the reduced thermal conductivity of silicon nanowires. *Phys. Rev. Lett.* **108,** 215901 (2012).

10. Hippalgaonkar, K. *et al.* Fabrication of microdevices with integrated nanowires for investigating low-dimensional phonon transport. *Nano Lett.* **10,** 4341–4348 (2010).

11. Hochbaum, A. I. *et al.* Enhanced thermoelectric performance of rough silicon nanowires. *Nature* **451,** 163–167 (2008).

12. Li, D. *et al.* Thermal conductivity of individual silicon nanowires. *Appl. Phys. Lett.* **83,** 2934–2936 (2003).

13. Park, Y.-H. *et al.* Thermal conductivity of VLS-grown rough Si nanowires with various surface roughnesses and diameters. *Appl. Phys. A* **104,** 7 (2011).

14. Martin, P., Aksamija, Z., Pop, E. & Ravaioli, U. Impact of phonon-surface roughness scattering on thermal conductivity of thin Si nanowires. *Phys. Rev. Lett.* **102,** 125503 (2009).

15. Klemens, P. Thermal conductivity and lattice vibrational modes. *Solid State Phys.* **7,** 1–98 (1958).

16. Meng, F., Morin, S. A., Forticaux, A. & Jin, S. Screw dislocation driven growth of nanomaterials. *Acc. Chem. Res.* **46,** 1616–1626 (2013).

17. Pei, Y. *et al.* Convergence of electronic bands for high performance bulk thermoelectrics. *Nature* **473,** 66–69 (2011).

18. Bhandari, C. & Rowe, D. Silicon–germanium alloys as high-temperature thermoelectric materials. *Contemp. Phys.* **21,** 219–242 (1980).

19. Savino, R., Fumo, M. D. S., Paterna, D. & Serpico, M. Aerothermodynamic study of UHTC-based thermal protection systems. *Aerosp. Sci. Technol.* **9,** 151–160 (2005).

20. Paul, A. *et al.* UHTC composites for hypersonic applications. (2012).

21. Corral, E. L. & Walker, L. S. Improved ablation resistance of C–C composites using zirconium diboride and boron carbide. *J. Eur. Ceram. Soc.* **30,** 2357–2364 (2010).

22. Tului, M. *et al.* Effects of heat treatments on oxidation resistance and mechanical properties of ultra high temperature ceramic coatings. *Surf. Coat. Technol.* **202,** 4394–4398 (2008).

23. Jansen, M., Schön, J. C. & van Wüllen, L. The route to the structure determination of amorphous solids: A case study of the ceramic Si3B3N7. *Angew. Chem. Int. Ed.* **45,** 4244–4263 (2006).

24. Hannemann, A., Schön, J. C. & Jansen, M. Modeling the sol–gel synthesis route of amorphous Si 3 B 3 N 7. *J. Mater. Chem.* **15,** 1167–1178 (2005).

25. Hannemann, A., Schön, J., Jansen, M. & Sibani, P. Nonequilibrium dynamics in amorphous Si3B3N7. *J. Phys. Chem. B* **109,** 11770–11776 (2005).

26. He, J. *et al.* Microstructure characterization of high-temperature, oxidation-resistant Si-BCN films. *Thin Solid Films* **542,** 167–173 (2013).

27. Tang, Y. *et al.* Polymer-Derived SiBN Fiber for High-Temperature Structural/Functional Applications. *Chem. Eur. J.* **16,** 6458–6462 (2010).

28. Schön, J. C., Hannemann, A., Sethi, G., Pentin, V. I. & Jansen, M. Modelling structure and properties of amorphous silicon boron nitride ceramics. *Process. Appl. Ceram.* **5,** 49–61 (2011).

29. Iijima, S. Helical microtubules of graphitic carbon. *nature* **354,** 56 (1991).

30. Berber, S., Kwon, Y.-K. & Tománek, D. Unusually high thermal conductivity of carbon nanotubes. *Phys. Rev. Lett.* **84,** 4613 (2000).

31. Che, J., Cagin, T. & Goddard III, W. A. Thermal conductivity of carbon nanotubes. *Nanotechnology* **11,** 65 (2000).

32. Fujii, M. *et al.* Measuring the thermal conductivity of a single carbon nanotube. *Phys. Rev. Lett.* **95,** 065502 (2005).

33. Mingo, N. & Broido, D. Carbon nanotube ballistic thermal conductance and its limits. *Phys. Rev. Lett.* **95,** 096105 (2005).

34. Pop, E., Mann, D., Wang, Q., Goodson, K. & Dai, H. Thermal conductance of an individual single-wall carbon nanotube above room temperature. *Nano Lett.* **6,** 96–100 (2006).

35. Arias, I. & Arroyo, M. Size-dependent nonlinear elastic scaling of multiwalled carbon nanotubes. *Phys. Rev. Lett.* **100,** 085503 (2008).

36. Iijima, S., Brabec, C., Maiti, A. & Bernholc, J. Structural flexibility of carbon nanotubes. *J. Chem. Phys.* **104,** 2089–2092 (1996).

37. Hernandez, E., Goze, C., Bernier, P. & Rubio, A. Elastic properties of C and B x C y N z composite nanotubes. *Phys. Rev. Lett.* **80,** 4502 (1998).

38. Demczyk, B. *et al.* Direct mechanical measurement of the tensile strength and elastic modulus of multiwalled carbon nanotubes. *Mater. Sci. Eng. A* **334,** 173–178 (2002).

39. Dumitrica, T., Hua, M. & Yakobson, B. I. Symmetry-, time-, and temperature-dependent strength of carbon nanotubes. *Proc. Natl. Acad. Sci.* **103,** 6105–6109 (2006).

40. Zhang, D.-B., James, R. & Dumitrică, T. Electromechanical characterization of carbon nanotubes in torsion via symmetry adapted tight-binding objective molecular dynamics. *Phys. Rev. B* **80,** 115418 (2009).

41. Thostenson, E. T., Ren, Z. & Chou, T.-W. Advances in the science and technology of carbon nanotubes and their composites: a review. *Compos. Sci. Technol.* **61,** 1899–1912 (2001).

42. Baughman, R. H., Zakhidov, A. A. & De Heer, W. A. Carbon nanotubes--the route toward applications. *science* **297,** 787–792 (2002).

43. Xu, J. & Fisher, T. S. Enhancement of thermal interface materials with carbon nanotube arrays. *Int. J. Heat Mass Transf.* **49,** 1658–1666 (2006).

44. Panzer, M. *et al.* Thermal properties of metal-coated vertically aligned single-wall nanotube arrays. *J. Heat Transf.* **130,** 052401 (2008).

45. Fabris, D. *et al.* Application of carbon nanotubes to thermal interface materials. *J. Electron. Packag.* **133,** 020902 (2011).

46. Lee, V., Chen, R. & Chang, C.-W. Probing the limit of one-dimensional heat transfer under extreme bending strain. *Phys. Rev. B* **87,** 035406 (2013).

47. Chang, C., Okawa, D., Garcia, H., Majumdar, A. & Zettl, A. Nanotube phonon waveguide. *Phys. Rev. Lett.* **99,** 045901 (2007).

48. Volkov, A. N., Shiga, T., Nicholson, D., Shiomi, J. & Zhigilei, L. V. Effect of bending buckling of carbon nanotubes on thermal conductivity of carbon nanotube materials. *J. Appl. Phys.* **111,** 053501 (2012).

49. Huang, Z. *et al.* Temperature-dependent thermal conductivity of bent carbon nanotubes by molecular dynamics simulation. *J. Appl. Phys.* **109,** 104316 (2011).

50. Nishimura, F., Shiga, T., Maruyama, S., Watanabe, K. & Shiomi, J. Thermal conductance of buckled carbon nanotubes. *Jpn. J. Appl. Phys.* **51,** 015102 (2012).

51. Zhong, W.-R., Zhang, M.-P., Zheng, D.-Q. & Ai, B.-Q. Thermal conductivity of deformed carbon nanotubes. *J. Appl. Phys.* **109,** 074317 (2011).

52. Chopra, N. G., Benedict, L. X., Crespi, V. H. & Cohen, M. L. Fully collapsed carbon nanotubes. *Nature* **377,** 135 (1995).

53. Yu, M.-F., Kowalewski, T. & Ruoff, R. S. Structural analysis of collapsed, and twisted and collapsed, multiwalled carbon nanotubes by atomic force microscopy. *Phys. Rev. Lett.* **86,** 87 (2001).

54. Zhang, C. *et al.* Closed-edged graphene nanoribbons from large-diameter collapsed nanotubes. *Acs Nano* **6,** 6023–6032 (2012).

55. Choi, D. *et al.* Fabrication and characterization of fully flattened carbon nanotubes: a new graphene nanoribbon analogue. *Sci. Rep.* **3,** 1617 (2013).

56. Hertel, T., Walkup, R. E. & Avouris, P. Deformation of carbon nanotubes by surface van der Waals forces. *Phys. Rev. B* **58,** 13870 (1998).

57. Tersoff, J. & Ruoff, R. Structural properties of a carbon-nanotube crystal. *Phys. Rev. Lett.* **73,** 676 (1994).

58. Liu, S., Yue, J. & Wehmschulte, R. J. Large thick flattened carbon nanotubes. *Nano Lett.* **2,** 1439–1442 (2002).

59. Xiao, J. *et al.* Collapse and stability of single-and multi-wall carbon nanotubes. *Nanotechnology* **18,** 395703 (2007).

60. Liu, H. J. & Cho, K. A molecular dynamics study of round and flattened carbon nanotube structures. *Appl. Phys. Lett.* **85,** 807–809 (2004).

61. Zhang, D.-B. & Dumitrica, T. Effective strain in helical rippled carbon nanotubes: A unifying concept for understanding electromechanical response. *ACS Nano* **4,** 6966–6972 (2010).

62. Hone, J., Whitney, M. & Zettl, A. Thermal conductivity of single-walled carbon nanotubes. *Synth. Met.* **103,** 2498–2499 (1999).

63. Ma, J., Ni, Y., Volz, S. & Dumitrică, T. Thermal Transport in Single-Walled Carbon Nanotubes Under Pure Bending. *Phys. Rev. Appl.* **3,** 024014 (2015).

64. Ma, J., Ni, Y. & Dumitrică, T. Thermal conductivity and phonon scattering in severely bent carbon nanotubes and bi-layer graphene. *Mater. Today Proc.* **2,** 3819–3823 (2015).

65. Cao, G. & Chen, X. Buckling of single-walled carbon nanotubes upon bending: Molecular dynamics simulations and finite element method. *Phys. Rev. B* **73,** 155435 (2006).

66. Cheung, C. L., Kurtz, A., Park, H. & Lieber, C. M. Diameter-controlled synthesis of carbon nanotubes. *J Phys Chem B* **106,** 2429–2433 (2002).

67. Ren, Z. *et al.* Synthesis of large arrays of well-aligned carbon nanotubes on glass. *Science* **282,** 1105–1107 (1998).

68. Javey, A., Shim, M. & Dai, H. Electrical properties and devices of large-diameter single-walled carbon nanotubes. *Appl. Phys. Lett.* **80,** 1064–1066 (2002).

69. Griffin, P. B., Plummer, J. D. & Deal, M. D. Silicon VLSI technology: fundamentals, practice, and modeling. *1a Ed. Prentice Hall Inc* (2000).

70. Frank, F. The influence of dislocations on crystal growth. *Discuss. Faraday Soc.* **5,** 48–54 (1949).

71. Heindl, J., Strunk, H., Heydemann, V. & Pensl, G. Micropipes: hollow tubes in silicon carbide. *Phys. Status Solidi A* **162,** 251–262 (1997).

72. Morin, S. A., Bierman, M. J., Tong, J. & Jin, S. Mechanism and kinetics of spontaneous nanotube growth driven by screw dislocations. *Science* **328,** 476–480 (2010).

73. Morin, S. A. & Jin, S. Screw dislocation-driven epitaxial solution growth of ZnO nanowires seeded by dislocations in GaN substrates. *Nano Lett.* **10,** 3459–3463 (2010).

74. Bierman, M. J., Lau, Y. A., Kvit, A. V., Schmitt, A. L. & Jin, S. Dislocation-driven nanowire growth and Eshelby twist. *Science* **320,** 1060–1063 (2008).

75. Bierman, M. J., Lau, Y. A., Kvit, A. V., Schmitt, A. L. & Jin, S. Dislocation-driven nanowire growth and Eshelby twist. *Science* **320,** 1060–1063 (2008).

76. Frank, F. Capillary equilibria of dislocated crystals. *Acta Crystallogr.* **4,** 497–501 (1951).

77. Qian, W. *et al.* Open-core screw dislocations in GaN epilayers observed by scanning force microscopy and high-resolution transmission electron microscopy. *Appl. Phys. Lett.* **67,** 2284–2286 (1995).

78. Liliental-Weber, Z., Zakharov, D., Jasinski, J., O'keefe, M. & Morkoc, H. Screw dislocations in GaN grown by different methods. *Microsc. Microanal.* **10,** 47–54 (2004).

79. Jin, S., Bierman, M. J. & Morin, S. A. A new twist on nanowire formation: Screw-dislocation-driven growth of nanowires and nanotubes. *J. Phys. Chem. Lett.* **1,** 1472–1480 (2010).

80. Jacobs, B. W., Crimp, M. A., McElroy, K. & Ayres, V. M. Nanopipes in gallium nitride nanowires and rods. *Nano Lett* **8,** 4354–4358 (2008).

81. Tizei, L. *et al.* Enhanced Eshelby twist on thin wurtzite InP nanowires and measurement of local crystal rotation. *Phys. Rev. Lett.* **107,** 195503 (2011).

82. Zhu, J. *et al.* Formation of chiral branched nanowires by the Eshelby Twist. *Nat. Nanotechnol.* **3,** 477–481 (2008).

83. Maestre, D., Haussler, D., Cremades, A., Jager, W. & Piqueras, J. Complex defect structure in the core of Sn-doped In2O3 nanorods and its relationship with a dislocation-driven growth mechanism. *J. Phys. Chem. C* **115,** 18083–18087 (2011).

84. Wu, H., Meng, F., Li, L., Jin, S. & Zheng, G. Dislocation-driven CdS and CdSe nanowire growth. *ACS Nano* **6,** 4461–4468 (2012).

85. Chernatynskiy, A., Clarke, D. R. & Phillpot, S. R. in *Handbook of Nanoscience, Engineering, and Technology, Third Edition* 545–572 (CRC Press, 2012).

86. Kittel, C. *Introduction to solid state*. **162,** (John Wiley & Sons, 1966).

87. Klemens, P. The scattering of low-frequency lattice waves by static imperfections. *Proc. Phys. Soc. Sect. A* **68,** 1113 (1955).

88. Carruthers, P. Theory of thermal conductivity of solids at low temperatures. *Rev. Mod. Phys.* **33,** 92 (1961).

89. Ziman, J. M. *Electrons and phonons: the theory of transport phenomena in solids*. (Oxford university press, 1960).

90. Callaway, J. Model for lattice thermal conductivity at low temperatures. *Phys. Rev.* **113,** 1046 (1959).

91. Ward, A., Broido, D., Stewart, D. A. & Deinzer, G. Ab initio theory of the lattice thermal conductivity in diamond. *Phys. Rev. B* **80,** 125203 (2009).

92. Berman, R. & Klemens, P. G. Thermal conduction in solids. (1978).

93. Kneeze, G. A. & Granato, A. Effect of independent and coupled vibrations of dislocations on low-temperature thermal conductivity in alkali halides. *Phys. Rev. B* **25,** 2851 (1982).

94. Ninomiya, T. Dislocation vibration and phonon scattering. *J. Phys. Soc. Jpn.* **25,** 830–840 (1968).

95. Sproull, R., Moss, M. & Weinstock, H. Effect of dislocations on the thermal conductivity of lithium fluoride. *J. Appl. Phys.* **30,** 334–337 (1959).

96. Bross, H., Seeger, A. & Haberkorn, R. Der Gitterwärmewiderstand von Stufenversetzungen. *Phys. Status Solidi B* **3,** 1126–1140 (1963).

97. Mion, C., Muth, J., Preble, E. & Hanser, D. Accurate dependence of gallium nitride thermal conductivity on dislocation density. *Appl. Phys. Lett.* **89,** 092123 (2006).

98. Ansari, M., Kumar, A. & Srivastava, B. Thermal conductivity of germanium containing dislocations at low temperatures. *Phys. Status Solidi B* **116,** 163–167 (1983).

99. Kogure, Y. & Hiki, Y. Effect of Dislocations on Low-Temperature Thermal Conductivity and Specific Heat of Copper-Aluminum Alloy Crystals. *J. Phys. Soc. Jpn.* **39,** 698–707 (1975).

100. Taylor, A., Albers, H. & Pohl, R. Effect of plastic deformation on the thermal conductivity of various ionic crystals. *J. Appl. Phys.* **36,** 2270–2278 (1965).

101. Wasserbäch, W., Abens, S., Sahling, S., Pohl, R. & Thompson, E. Low-Temperature Acoustic and Thermal Properties of Plastically Deformed, High-Purity Polycrystalline Aluminum. *Phys. Status Solidi B* **228,** 799–823 (2001).

102. Zhang, D.-B., Hua, M. & Dumitrică, T. Stability of polycrystalline and wurtzite Si nanowires via symmetry-adapted tight-binding objective molecular dynamics. *J. Chem. Phys.* **128,** 084104 (2008).

103. Akatyeva, E., Huang, J. & Dumitrică, T. Edge-mediated dislocation processes in multishell carbon nano-onions? *Phys. Rev. Lett.* **105,** 106102 (2010).

104. Schapotschnikow, P., van Huis, M. A., Zandbergen, H. W., Vanmaekelbergh, D. & Vlugt, T. J. Morphological transformations and fusion of PbSe nanocrystals studied using atomistic simulations. *Nano Lett.* **10,** 3966–3971 (2010).

105. Stillinger, F. H. & Weber, T. A. Computer simulation of local order in condensed phases of silicon. *Phys. Rev. B* **31,** 5262 (1985).

106. Dumitrică, T. & James, R. D. Objective molecular dynamics. *J. Mech. Phys. Solids* **55,** 2206–2236 (2007).

107. Tretiakov, K. V. & Scandolo, S. Thermal conductivity of solid argon from molecular dynamics simulations. *J. Chem. Phys.* **120,** 3765–3769 (2004).

108. Volz, S. G. & Chen, G. Molecular-dynamics simulation of thermal conductivity of silicon crystals. *Phys. Rev. B* **61,** 2651 (2000).

109. James, R. D. Objective structures. *J. Mech. Phys. Solids* **54,** 2354–2390 (2006).

110. Schneider, T. & Stoll, E. Molecular-dynamics study of a three-dimensional one-component model for distortive phase transitions. *Phys. Rev. B* **17,** 1302 (1978).

111. Nosé, S. A molecular dynamics method for simulations in the canonical ensemble. *Mol. Phys.* **52,** 255–268 (1984).

112. Hoover, W. G. Canonical dynamics: equilibrium phase-space distributions. *Phys. Rev. A* **31,** 1695 (1985).

113. Stevens, R. J., Zhigilei, L. V. & Norris, P. M. Effects of temperature and disorder on thermal boundary conductance at solid–solid interfaces: Nonequilibrium molecular dynamics simulations. *Int. J. Heat Mass Transf.* **50,** 3977–3989 (2007).

114. Xiong, S., Ma, J., Volz, S. & Dumitrică, T. Thermally-Active Screw Dislocations in Si Nanowires and Nanotubes. *Small* **10,** 1756–1760 (2014).

115. Al-Ghalith, J., Ni, Y. & Dumitrică, T. Nanowires with dislocations for ultralow lattice thermal conductivity. *Phys. Chem. Chem. Phys.* **18,** 9888–9892 (2016).

116. Bell, L. E. Cooling, heating, generating power, and recovering waste heat with thermoelectric systems. *Science* **321,** 1457–1461 (2008).

117. Hsu, K. F. *et al.* Cubic AgPbmSbTe2+ m: bulk thermoelectric materials with high figure of merit. *Science* **303,** 818–821 (2004).

118. Poudel, B. *et al.* High-thermoelectric performance of nanostructured bismuth antimony telluride bulk alloys. *Science* **320,** 634–638 (2008).

119. Lau, Y. A., Chernak, D. J., Bierman, M. J. & Jin, S. Formation of PbS nanowire pine trees driven by screw dislocations. *J. Am. Chem. Soc.* **131,** 16461–16471 (2009).

120. Lau, Y. A., Chernak, D. J., Bierman, M. J. & Jin, S. Epitaxial growth of hierarchical PbS nanowires. *J. Mater. Chem.* **19,** 934–940 (2009).

121. Skye, A. & Schelling, P. K. Thermal resistivity of Si–Ge alloys by molecular-dynamics simulation. *J. Appl. Phys.* **103,** 113524 (2008).

122. Kim, S. I. *et al.* Dense dislocation arrays embedded in grain boundaries for high-performance bulk thermoelectrics. *Science* **348,** 109–114 (2015).

123. Schelling, P. K., Phillpot, S. R. & Keblinski, P. Comparison of atomic-level simulation methods for computing thermal conductivity. *Phys. Rev. B* **65,** 144306 (2002).

124. Zhang, W., Fisher, T. & Mingo, N. Simulation of interfacial phonon transport in Si–Ge heterostructures using an atomistic Green's function method. *J. Heat Transf.* **129,** 483–491 (2007).

125. Mingo, N. & Yang, L. Phonon transport in nanowires coated with an amorphous material: An atomistic Green's function approach. *Phys. Rev. B* **68,** 245406 (2003).

126. Zhang, W., Mingo, N. & Fisher, T. Simulation of phonon transport across a non-polar nanowire junction using an atomistic Green's function method. *Phys. Rev. B* **76,** 195429 (2007).

127. Eshelby, J. Screw dislocations in thin rods. *J. Appl. Phys.* **24,** 176–179 (1953).

128. Tersoff, J. Modeling solid-state chemistry: Interatomic potentials for multicomponent systems. *Phys. Rev. B* **39,** 5566 (1989).

129.   Nikiforov, I., Zhang, D.-B. & Dumitrica, T. Screw Dislocations in⟨ 100⟩ Silicon Nanowires: An Objective Molecular Dynamics Study. *J. Phys. Chem. Lett.* **2,** 2544–2548 (2011).

130.   Akatyeva, E., Kou, L., Nikiforov, I., Frauenheim, T. & Dumitrica, T. Electrically active screw dislocations in helical ZnO and Si nanowires and nanotubes. *ACS Nano* **6,** 10042–10049 (2012).

131.   Hu, M. & Poulikakos, D. Si/Ge superlattice nanowires with ultralow thermal conductivity. *Nano Lett.* **12,** 5487–5494 (2012).

132.   Ishai, M. B. & Patolsky, F. Shape-and dimension-controlled single-crystalline silicon and SiGe nanotubes: toward nanofluidic FET devices. *J. Am. Chem. Soc.* **131,** 3679–3689 (2009).

133.   Li, X., Maute, K., Dunn, M. L. & Yang, R. Strain effects on the thermal conductivity of nanostructures. *Phys. Rev. B* **81,** 245318 (2010).

134.   Chalopin, Y., Mingo, N., Diao, J., Srivastava, D. & Volz, S. Large effects of pressure induced inelastic channels on interface thermal conductance. *Appl. Phys. Lett.* **101,** 221903 (2012).

135.   Tian, Z. *et al.* Phonon conduction in PbSe, PbTe, and PbTe 1− x Se x from first-principles calculations. *Phys. Rev. B* **85,** 184303 (2012).

136.   Garg, J., Bonini, N., Kozinsky, B. & Marzari, N. Role of disorder and anharmonicity in the thermal conductivity of silicon-germanium alloys: A first-principles study. *Phys. Rev. Lett.* **106,** 045901 (2011).

137. Abeles, B. Lattice thermal conductivity of disordered semiconductor alloys at high temperatures. *Phys. Rev.* **131,** 1906 (1963).

138. Wen, Y.-H., Zhang, Y., Zheng, J.-C., Zhu, Z.-Z. & Sun, S.-G. Orientation-dependent structural transition and melting of Au nanowires. *J. Phys. Chem. C* **113,** 20611–20617 (2009).

139. Liang, W., Zhou, M. & Ke, F. Shape memory effect in Cu nanowires. *Nano Lett.* **5,** 2039–2043 (2005).

140. Plimpton, S. Fast parallel algorithms for short-range molecular dynamics. *J. Comput. Phys.* **117,** 1–19 (1995).

141. Miller, A. Landolt-bornstein: Numerical data and functional relationships in science and technology. *J. Mod. Opt.* **32,** 507–508 (1985).

142. Dalven, R. A review of the semiconductor properties of PbTe, PbSe, PbS and PbO. *Infrared Phys.* **9,** 141–184 (1969).

143. Wei, S.-H. & Zunger, A. Electronic and structural anomalies in lead chalcogenides. *Phys. Rev. B* **55,** 13605 (1997).

144. Zhang, Y., Ke, X., Chen, C., Yang, J. & Kent, P. Thermodynamic properties of PbTe, PbSe, and PbS: First-principles study. *Phys. Rev. B* **80,** 024304 (2009).

145. Jian, Z., Kaiming, Z. & Xide, X. Modification of stillinger-weber potentials for si and ge. *Phys. Rev. B* **41,** 12915 (1990).

146. Lee, E. K. *et al.* Large thermoelectric figure-of-merits from SiGe nanowires by simultaneously measuring electrical and thermal transport properties. *Nano Lett.* **12,** 2918–2923 (2012).

147. Cheaito, R. *et al.* Experimental investigation of size effects on the thermal conductivity of silicon-germanium alloy thin films. *Phys. Rev. Lett.* **109,** 195901 (2012).

148. Akatyeva, E. & Dumitrică, T. Eshelby twist and magic helical zinc oxide nanowires and nanotubes. *Phys. Rev. Lett.* **109,** 035501 (2012).

149. Ni, Y., Xiong, S., Volz, S. & Dumitrică, T. Thermal transport along the dislocation line in silicon carbide. *Phys. Rev. Lett.* **113,** 124301 (2014).

150. Chen, R. *et al.* Thermal conductance of thin silicon nanowires. *Phys. Rev. Lett.* **101,** 105501 (2008).

151. Donadio, D. & Galli, G. Atomistic simulations of heat transport in silicon nanowires. *Phys. Rev. Lett.* **102,** 195901 (2009).

152. Merabia, S. & Termentzidis, K. Thermal boundary conductance across rough interfaces probed by molecular dynamics. *Phys. Rev. B* **89,** 054309 (2014).

153. Lee, Y., Lee, S. & Hwang, G. S. Effects of vacancy defects on thermal conductivity in crystalline silicon: A nonequilibrium molecular dynamics study. *Phys. Rev. B* **83,** 125202 (2011).

154. Al-Ghalith, J., Dasmahapatra, A., Kroll, P., Meletis, E. & Dumitrica, T. Compositional and Structural Atomistic Study of Amorphous Si–B–N Networks of Interest for High-Performance Coatings. *J. Phys. Chem. C* **120,** 24346–24353 (2016).

155. Lawson, J. W., Daw, M. S. & Bauschlicher Jr, C. W. Lattice thermal conductivity of ultra high temperature ceramics ZrB2 and HfB2 from atomistic simulations. *J. Appl. Phys.* **110,** 083507 (2011).

156. Kindlund, H. *et al.* Toughness enhancement in hard ceramic thin films by alloy design. *APL Mater.* **1,** 042104 (2013).

157. Tang, B., An, Q. & Goddard III, W. A. Improved Ductility of Boron Carbide by Microalloying with Boron Suboxide. *J. Phys. Chem. C* **119,** 24649–24656 (2015).

158. Zhang, K. *et al.* Epitaxial NbCxN 1− x (001) layers: Growth, mechanical properties, and electrical resistivity. *Surf. Coat. Technol.* **277,** 136–143 (2015).

159. Ni, Y., Jiang, J., Meletis, E. & Dumitrică, T. Thermal transport across few-layer boron nitride encased by silica. *Appl. Phys. Lett.* **107,** 031603 (2015).

160. Griebel, M. & Hamaekers, J. Molecular dynamics simulations of boron-nitride nanotubes embedded in amorphous Si-BN. *Comput. Mater. Sci.* **39,** 502–517 (2007).

161. Ge, K., Ye, L., Han, W., Han, Y. & Zhao, T. Pyrolysis of polyborosilazane and its conversion into SiBN ceramic. *Adv. Appl. Ceram.* **113,** 367–371 (2014).

162. Matsunaga, K. & Iwamoto, Y. Molecular dynamics study of atomic structure and diffusion behavior in amorphous silicon nitride containing boron. *J Am Ceram Soc* **84,** 2213–2219 (2001).

163. Kroll, P. & Hoffmann, R. Silicon boron nitrides: Hypothetical polymorphs of Si3B3N7. *Angew. Chem. Int. Ed.* **37,** 2527–2530 (1998).

164. Dumitrică, T. & Yakobson, B. I. Rate theory of yield in boron nitride nanotubes. *Phys. Rev. B* **72,** 035418 (2005).

165. Kroll, P. Modelling polymer-derived ceramics. *J. Eur. Ceram. Soc.* **25,** 163–174 (2005).

166. Jalowiecki, A., Bill, J., Aldinger, F. & Mayer, J. Interface characterization of nanosized B-doped Si3N4/SiC ceramics. *Compos. Part Appl. Sci. Manuf.* **27,** 717–721 (1996).

167. Esfarjani, K., Chen, G. & Stokes, H. T. Heat transport in silicon from first-principles calculations. *Phys. Rev. B* **84,** 085204 (2011).

168. Chaplot, S. L., Mittal, R. & Choudhury, N. *Thermodynamic Properties of Solids: Experiments and Modeling*. (John Wiley & Sons, 2010).

169. Capilla, J. *et al.* Characterization of amorphous tantalum oxide for insulating acoustic mirrors. in 1–6 (IEEE, 2011).

170. Testardi, L. & Hauser, J. Sound velocity in amorphous Ge and Si. *Solid State Commun.* **21,** 1039–1041 (1977).

171. Clarke, D. R. Materials selection guidelines for low thermal conductivity thermal barrier coatings. *Surf. Coat. Technol.* **163,** 67–74 (2003).

172. Cahill, D. G., Watson, S. K. & Pohl, R. O. Lower limit to the thermal conductivity of disordered crystals. *Phys. Rev. B* **46,** 6131 (1992).

173. Simpson, A. & Stuckes, A. The thermal conductivity of highly oriented pyrolytic boron nitride. *J. Phys. C Solid State Phys.* **4,** 1710 (1971).

174. Jäschke, T. & Jansen, M. Synthesis and characterization of new amorphous Si/B/N/C ceramics with increased carbon content through single-source precursors. *Comptes Rendus Chim.* **7,** 471–482 (2004).

175. Zhang, M. *et al.* A study of the microstructure evolution of hard Zr–B–C–N films by high-resolution transmission electron microscopy. *Acta Mater.* **77,** 212–222 (2014).

176. Zhang, M. *et al.* Effect of the Si content on the microstructure of hard, multifunctional Hf–B–Si–C films prepared by pulsed magnetron sputtering. *Appl. Surf. Sci.* **357,** 1343–1354 (2015).

177. Kalweit, M. & Drikakis, D. Multiscale methods for micro/nano flows and materials. *J. Comput. Theor. Nanosci.* **5,** 1923–1938 (2008).

178. Asproulis, N., Kalweit, M. & Drikakis, D. A hybrid molecular continuum method using point wise coupling. *Adv. Eng. Softw.* **46,** 85–92 (2012).

179. Wang, C. *et al.* Buckling behavior of carbon nanotubes under bending: From ripple to kink. *Carbon* **102,** 224–235 (2016).

180. Mingo, N. & Broido, D. Length dependence of carbon nanotube thermal conductivity and the 'problem of long waves'. *Nano Lett.* **5,** 1221–1225 (2005).

181. Shiomi, J. & Maruyama, S. Molecular dynamics of diffusive-ballistic heat conduction in single-walled carbon nanotubes. *Jpn. J. Appl. Phys.* **47,** 2005 (2008).

182. Falvo, M. R. *et al.* Bending and buckling of carbon nanotubes under large strain. *Nature* **389,** 582–584 (1997).

183. Hernandez, E., Goze, C., Bernier, P. & Rubio, A. Elastic properties of C and B x C y N z composite nanotubes. *Phys. Rev. Lett.* **80,** 4502 (1998).

184. Zhang, D.-B. & Dumitrică, T. Elasticity of ideal single-walled carbon nanotubes via symmetry-adapted tight-binding objective modeling. *Appl. Phys. Lett.* **93,** 031919 (2008).

185. Zhang, D.-B., James, R. & Dumitrică, T. Electromechanical characterization of carbon nanotubes in torsion via symmetry adapted tight-binding objective molecular dynamics. *Phys. Rev. B* **80,** 115418 (2009).

186. Wang, Q., Liew, K. M. & Duan, W. Modeling of the mechanical instability of carbon nanotubes. *Carbon* **46,** 285–290 (2008).

187. Harris, J. M. *et al.* Electronic durability of flexible transparent films from type-specific single-wall carbon nanotubes. *ACS Nano* **6,** 881–887 (2011).

188. Abadi, P. P. S. S. *et al.* Reversible tailoring of mechanical properties of carbon nanotube forests by immersing in solvents. *Carbon* **69,** 178–187 (2014).

189. Cola, B. A., Xu, X. & Fisher, T. S. Increased real contact in thermal interfaces: A carbon nanotube/foil material. *Appl. Phys. Lett.* **90,** 093513 (2007).

190. Nikiforov, I., Zhang, D.-B., James, R. D. & Dumitrică, T. Wavelike rippling in multiwalled carbon nanotubes under pure bending. *Appl. Phys. Lett.* **96,** 123107 (2010).

191.   Tsai, P.-C., Jeng, Y.-R., Huang, Y.-X. & Wu, K.-T. Buckling characterizations of an individual multi-walled carbon nanotube: Insights from quantitative in situ transmission electron microscope nanoindentation and molecular dynamics. *Appl. Phys. Lett.* **103,** 053119 (2013).

192.   Wong, E. W., Sheehan, P. E. & Lieber, C. M. Nanobeam mechanics: elasticity, strength, and toughness of nanorods and nanotubes. *Science* **277,** 1971–1975 (1997).

193.   Jackman, H., Krakhmalev, P. & Svensson, K. Measurements of the critical strain for rippling in carbon nanotubes. *Appl. Phys. Lett.* **98,** 183104 (2011).

194.   Cao, A. & Qu, J. Size dependent thermal conductivity of single-walled carbon nanotubes. *J. Appl. Phys.* **112,** 013503 (2012).

195.   Xu, Z. & Buehler, M. J. Strain controlled thermomutability of single-walled carbon nanotubes. *Nanotechnology* **20,** 185701 (2009).

196.   Lee, V., Chen, R. & Chang, C.-W. Probing the limit of one-dimensional heat transfer under extreme bending strain. *Phys. Rev. B* **87,** 035406 (2013).

197.   Rurali, R. & Hernandez, E. Trocadero: a multiple-algorithm multiple-model atomistic simulation program. *Comput. Mater. Sci.* **28,** 85–106 (2003).

198.   Stuart, S. J., Tutein, A. B. & Harrison, J. A. A reactive potential for hydrocarbons with intermolecular interactions. *J. Chem. Phys.* **112,** 6472–6486 (2000).

199.   Salaway, R. N. & Zhigilei, L. V. Molecular dynamics simulations of thermal conductivity of carbon nanotubes: Resolving the effects of computational parameters. *Int. J. Heat Mass Transf.* **70,** 954–964 (2014).

200. Lukes, J. R. & Zhong, H. Thermal conductivity of individual single-wall carbon nanotubes. *J. Heat Transf.* **129,** 705–716 (2007).

201. Lindsay, L., Broido, D. & Mingo, N. Lattice thermal conductivity of single-walled carbon nanotubes: Beyond the relaxation time approximation and phonon-phonon scattering selection rules. *Phys. Rev. B* **80,** 125407 (2009).

202. Brenner, D. W. *et al.* A second-generation reactive empirical bond order (REBO) potential energy expression for hydrocarbons. *J. Phys. Condens. Matter* **14,** 783 (2002).

203. Lindsay, L. & Broido, D. Optimized Tersoff and Brenner empirical potential parameters for lattice dynamics and phonon thermal transport in carbon nanotubes and graphene. *Phys. Rev. B* **81,** 205441 (2010).

204. Tersoff, J. Empirical interatomic potential for carbon, with applications to amorphous carbon. *Phys. Rev. Lett.* **61,** 2879 (1988).

205. Nikiforov, I., Dontsova, E., James, R. & Dumitrică, T. Tight-binding theory of graphene bending. *Phys. Rev. B* **89,** 155437 (2014).

206. Zou, J.-H. *et al.* Phonon thermal properties of graphene from molecular dynamics using different potentials. *J. Chem. Phys.* **145,** 134705 (2016).

207. Lu, Q., Arroyo, M. & Huang, R. Elastic bending modulus of monolayer graphene. *J. Phys. Appl. Phys.* **42,** 102002 (2009).

208. Hone, J. in *Carbon Nanotubes* 273–286 (Springer, 2001).

209. Thomas, J. A., Turney, J. E., Iutzi, R. M., Amon, C. H. & McGaughey, A. J. Predicting phonon dispersion relations and lifetimes from the spectral energy density. *Phys. Rev. B* **81,** 081411 (2010).

210. Liu, Y., Yang, H., Liao, N. & Yang, P. Investigation on thermal conductivity of bilayer graphene nanoribbons. *RSC Adv.* **4,** 54474–54479 (2014).

211. Si, C., Wang, X.-D., Fan, Z., Feng, Z.-H. & Cao, B.-Y. Impacts of potential models on calculating the thermal conductivity of graphene using non-equilibrium molecular dynamics simulations. *Int. J. Heat Mass Transf.* **107,** 450–460 (2017).

212. Ghosh, S. *et al.* Dimensional crossover of thermal transport in few-layer graphene. *Nat. Mater.* **9,** 555–558 (2010).

213. Kong, B. D., Paul, S., Nardelli, M. B. & Kim, K. W. First-principles analysis of lattice thermal conductivity in monolayer and bilayer graphene. *Phys. Rev. B* **80,** 033406 (2009).

214. Singh, D., Murthy, J. Y. & Fisher, T. S. Mechanism of thermal conductivity reduction in few-layer graphene. *J. Appl. Phys.* **110,** 044317 (2011).

215. Zhang, J. *et al.* Effect of tensile strain on thermal conductivity in monolayer graphene nanoribbons: A molecular dynamics study. *Sensors* **13,** 9388–9395 (2013).

216. Zhao, H. & Freund, J. Lattice-dynamical calculation of phonon scattering at ideal Si–Ge interfaces. *J. Appl. Phys.* **97,** 024903 (2005).

217. Wang, J.-S., Zeng, N., Wang, J. & Gan, C. K. Nonequilibrium Green's function method for thermal transport in junctions. *Phys. Rev. E* **75,** 061128 (2007).

218. Markussen, T., Jauho, A.-P. & Brandbyge, M. Electron and phonon transport in silicon nanowires: Atomistic approach to thermoelectric properties. *Phys. Rev. B* **79,** 035415 (2009).

219. *Atomistix ToolKit version 2016.3, QuantumWise A/S (www.quantumwise.com).*

220. Bets, K. V. & Yakobson, B. I. Spontaneous twist and intrinsic instabilities of pristine graphene nanoribbons. *Nano Res.* **2,** 161–166 (2009).